# PONTIFICIA UNIVERSIDAD CATÓLICA DEL PERÚ

## Escuela de Posgrado

# Synthesis, Tribology, Electro-Tribology and Mechanical Performance of $Ti_2AlC$ and $Ti_3AlC_2$ MAX Phases Thin Films

Tesis para obtener el grado académico de Doctor en Física que presenta:

***Roger Quispe Dominguez***

Asesor:

***Prof. Dr. Rolf Grieseler***

Lima, 2022

**Declaración jurada de autenticidad**

Yo, Dr. Rolf Grieseler, docente de la Escuela de Posgrado de la Pontificia Universidad Católica del Perú, asesor de la tesis titulada

*Synthesis, Tribology, Electro-Tribology and Mechanical Performance of Ti2AlC and Ti3AlC2 MAX Phases Thin Films* del autor Roger Quispe Dominguez, dejo constancia de lo siguiente:

- Ha obtenido en la plataforma Turnitin un índice de similitud de 28%, pero se tiene que omitir las referencias 1, 2 y 7 del informe ya que partes de la tesis ya están publicadas en revistas internacionales, por lo tanto, se produce esta similitud con la tesis del alumno. El índice de similitud, omitiendo las referencias señaladas, es de 18%, lo que está dentro del límite establecido. Así lo consigna el reporte de similitud emitido por el software *Turnitin* el / /2022.
- He revisado con detalle dicho reporte y confirmo que cada una de las coincidencias detectadas no constituyen plagio alguno.
- Las citas a otros autores y sus respectivas referencias cumplen con las pautas académicas.

Lugar y fecha:

Lima, 04 de diciembre de 2022

| Apellidos y nombres de asesor : Grieseler, Rolf | |
|---|---|
| CE: 001660902 | Firma: |
| ORCID: 0000-0001-5307-7755 | |

# Abstract

This thesis investigates the synthesis, mechanical properties, tribological and electro-tribological behavior of $Ti_2AlC$ and $Ti_3AlC_2$ MAX phases in the form of thin films. The thin films were obtained by deposition of a multilayer system of Titanium (Ti) - Aluminum (Al) - Carbon (C) and subsequent thermal annealing in a vacuum and controlled atmosphere. The Ti-Al-C multilayer system was deposited by magnetron sputtering on silicon substrates with a $SiO_2$ and $Si_xN_y$ double-layer diffusion barrier. The stoichiometric of the film was controlled through the thickness of the individual monolayers. To obtain a 500 nm thick film, the Ti-Al-C sequence was repeated 22 times with individual thicknesses of 14, 6 and 3.5 nm, respectively. The experimental results show that the $Ti_2AlC$ phase is formed at a temperature of 700°C, while the $Ti_3AlC_2$ phase is formed at 950°C. The structural properties of the thin films were characterized by X-ray diffraction, Raman microscopy and glow discharge optical emission spectroscopy (GD-OES). The hardness of the thin films was analyzed by nanoindentation tests, obtaining hardness values of 11.6 and 5.3 GPa for $Ti_2AlC$ and $Ti_3AlC_2$, respectively. The tribological behavior of the thin films was analyzed under dry sliding conditions using a ball-on-flat reciprocating tribometer. The counter body consisted of AISI 52100 steel balls of 3 mm diameter. The friction coefficients obtained were in the range of 0.21 - 0.2 and 0.6 - 0.91 for the $Ti_2AlC$ and $Ti_3AlC_2$ thin films, respectively. The $Ti_2AlC$ phase has a better tribological performance, which can be attributed to its smaller grain size, lower surface roughness and higher hardness compared to the $Ti_3AlC_2$ phase. The electrical resistivity of the thin films was 0.73 and 0.45 $\mu\Omega \cdot m$ for $Ti_2AlC$ and $Ti_3AlC_2$, respectively. The electro-tribological test was carried out using a ball-on-flat reciprocating tribometer under electrical currents of 10, 50 and 100 mA. The coefficient of friction and the electrical contact resistance were measured simultaneously in the same test. The results show that the coefficient of friction and electrical contact resistance could be related to thin-film properties such as hardness, roughness, grain size, and resistivity. These results of the electro-tribological behavior of the films provide valuable information for possible applications such as sliding electrical contacts.

# Resumen

La presente tesis investiga la síntesis, propiedades mecánicas, comportamiento tribológico y electro-tribológico de $Ti_2AlC$ y $Ti_3AlC_2$ fases MAX en forma de películas delgadas. Las películas delgadas se obtuvieron mediante deposición de un sistema de multicapas de Titanio (Ti) - Aluminio (Al) – Carbono (C) y un posterior tratamiento térmico en vacío y atmosfera controlada. El sistema de multicapa de Ti-Al-C fue depositado mediante pulverización catódica sobre sustratos de silicio con una barrera de difusión de doble capa de $SiO_2$ y $Si_xN_y$. La estequiométrica de la película se controló a través del espesor de las monocapas individuales. Para obtener una película de 500 nm de espesor, se repitió 22 veces la secuencia de Ti-Al-C con espesores individuales de 14, 6 y 3.5 nm, respectivamente. Los resultados experimentales muestran que la fase $Ti_2AlC$ se forma a una temperatura de 700°C, mientras que la fase $Ti_3AlC_2$ se forma a 950°C. Las propiedades estructurales de las películas delgadas fueron caracterizadas mediante difracción de rayos X, microscopia Raman y espectroscopia de emisión óptica de descarga luminiscente (GD-OES). La dureza de las películas delgadas fue analizada mediante ensayos de nanoindentacion, obteniéndose valores de dureza de 11.6 y 5.3 GPa para $Ti_2AlC$ y $Ti_3AlC_2$, respectivamente. El comportamiento tribológico de las películas fue analizado bajo condiciones de deslizamiento en seco mediante el tribómetro reciprocante ball-on-flat. El contra material utilizado consiste en bolas de acero AISI 52100 de 3 mm de diámetro. Los coeficientes de fricción obtenidos están en el rango de 0.21 - 0.2 y 0.6 - 0.91 para las películas delgadas de $Ti_2AlC$ y $Ti_3AlC_2$, respectivamente. La fase $Ti_2AlC$ tiene un mejor comportamiento tribológico y esto se puede atribuir a su menor tamaño de grano, menor rugosidad superficial y mayor dureza en comparación con la fase $Ti_3AlC_2$. La resistividad eléctrica de las películas delgadas fue de 0.73 y 0.45 μΩ·m para $Ti_2AlC$ y $Ti_3AlC_2$, respectivamente. El ensayo electro-tribológico se llevó a cabo utilizando un tribómetro reciprocante ball-on-flat bajo corrientes eléctricas de 10, 50 y 100 mA. El coeficiente de fricción y la resistencia de contacto eléctrico se midieron simultáneamente en una misma prueba. Los resultados muestran que el coeficiente de fricción y la resistencia de contacto eléctrico podrían estar relacionados con las propiedades de película delgada como dureza, rugosidad, tamaño de grano y resistividad. Estos resultados del comportamiento electro-tribológico de las películas proporcionan información valiosa para posibles aplicaciones como contactos eléctricos deslizantes.

# Dedicatory

This thesis is dedicated to my lovely family: Roger Sebastián, Victoria, Lucio Antonio, Mario, Susana, Lucio Antonio Jr., Marleny, Edwin, Joel and Walter.

# Acknowledgements

I want to express my greatest gratitude to my advisor, Prof. Dr. Rolf Grieseler, for having trusted and agreed to be my advisor without having many references about me. I greatly appreciate the time and dedication that you always showed throughout these four years of continuous research work. You knew how to guide, support, and motivate me even in challenging situations. The long hours of planning and discussing the results remain in my memory. Very grateful for the time dedicated to the observations and corrections to the scientific articles and the redaction of this thesis.

This research was financed thanks to a doctoral scholarship from the National Fund for Scientific and Technological Development of Peru (FONDECYT) with contract number 233-2015. Similarly, I would like to thank the German Academic Exchange Service (DAAD) and the PUCP – KAAD Scholarship (Katholischer Akademischer Ausländer-Dienst) for the additional support in carrying out research internships in Germany. I thank Prof. Dr. Francisco Rumiche for allowing me to use the facilities of the Materials Characterization Center of the Pontifical Catholic University of Peru (CAM-PUCP). I want to express my gratitude to Univ.-Prof. Dr. rer. nat. habil. Dr. h. c. Peter Schaaf of the Technische Universitat Ilmenau (TU Ilmenau, Germany), for his constant support and for allowing me to use the laboratory of the Centre for Micro and Nanotechnologies (ZNM) during the research internships carried out at his institution. I would like to thank Dr. Henry Romanus, Dr. Manuel Oliva, Dipl.-Ing. Marcus Hopfeld, M.Sc. Hauke-Lars Honig, M.Sc. Yesenia Sauñi, M.Sc. Teresa Scheler and Mr. Joachim Döll from ZMN for supporting me during the synthesis and characterization of the thin films. Furthermore, I would like to express my gratitude to Prof. Hartmut Witte, M.Sc. José Zárate, Dipl.-Ing. Thomas Helbig, Dipl.-Ing. Sebastian Köhring and Dipl.-Betriebswirt Wolfgang Kempf from the Biomechatronics Group at TU Ilmenau for their support with the tribological tests.

I thank my friends and colleagues from the Materials Science and Renewable Energies Research Group (MatER-PUCP). Dr. Andrés Guerra, Dr. Amaru Palomino, Carlos Torres, Zully Calderón, Mary Mejía, Luis Conde, Miguel Piñeiro, Paul Llontop, Erick Serquen, Francisco Sanchez, Miguel Sevillano, Alvaro Tejada, Jorge Dulanto, Kevin Lizarraga, etc. Very grateful to all of you for the experiences and moments lived in the laboratory. Last but not least, I would like to thank my family and close friends for their continued support during my doctoral studies.

# Table of contents

**Abstract** ..... **i**
**Resumen** ..... **ii**
**Dedicatory** ..... **iii**
**Acknowledgements** ..... **iv**
**Table of contents** ..... **v**
**List of figures** ..... **viii**
**List of tables** ..... **xii**
**List of symbols and abbreviations** ..... **xiii**
**Chapter 1. Introduction and Motivation** ..... **1**
**Chapter 2. Fundamental Theory and State of the Art** ..... **3**
2.1 $M_{n+1}AX_n$ phase materials ..... 3
*2.1.1 The structural properties of MAX phases – Crystal structure* ..... *3*
*2.1.2 The MAX phases processing techniques* ..... *4*
2.2 Fundamentals concepts of tribology ..... 5
*2.2.1 Roughness and characteristics of solid surfaces* ..... *5*
*2.2.2 Friction under dry sliding conditions* ..... *6*
*2.2.3 Wear mechanisms* ..... *9*
*2.2.4 Lubrication regimens* ..... *12*
*2.2.5 Types of tribometers* ..... *13*
2.3 Tribology of coatings and thin films ..... 13
2.4 Tribology of MAX phases ..... 15
2.5 Fundamentals concepts of electrical contacts ..... 20
*2.5.1 Introduction to electrical contacts* ..... *20*
*2.5.2 Electrical contact resistance* ..... *20*
*2.5.3 Influence of the load in electrical contacts* ..... *23*
*2.5.4 The voltage-temperature relation in electrical contact interfaces* ..... *25*
**Chapter 3. Synthesis of $Ti_2AlC$ and $Ti_3AlC_2$ MAX phases thin films** ..... **26**
3.1 Experimental details ..... 26
*3.1.1 The deposition process of $Ti_2AlC$ and $Ti_3AlC_2$ MAX phases thin films* ..... *26*
*3.1.2 Annealing treatment* ..... *28*
**Chapter 4. Characterization of the structural properties, composition and morphology of $Ti_2AlC$ and $Ti_3AlC_2$ thin films** ..... **29**

4.1 Thin film characterization techniques are used to obtain structural properties and chemical composition as well as the surface roughness and morphology ..... 29
4.2 The chemical composition profiles of $Ti_2AlC$ and $Ti_3AlC_2$ ..... 30
4.3 XRD and Raman measurements ..... 32
*4.3.1 Lattice parameters and density of $Ti_2AlC$ and $Ti_3AlC_2$ ..... 33*
*4.3.2 Texture analysis of $Ti_2AlC$ and $Ti_3AlC_2$ ..... 39*
4.4 Atomic force microscopy of $Ti_2AlC$ and $Ti_3AlC_2$ ..... 42
4.5 Conclusions ..... 42
**Chapter 5. Mechanical and tribological performance of $Ti_2AlC$ and $Ti_3AlC_2$ thin films ... 43**
5.1 Introduction ..... 43
5.2 Experimental details ..... 43
*5.2.1 Hardness measurements of $Ti_2AlC$ and $Ti_3AlC_2$ ..... 43*
*5.2.2 Tribological measurements of $Ti_2AlC$ and $Ti_3AlC_2$ ..... 43*
*5.2.3 Chemical composition and wear profile of worn tracks ..... 44*
5.3 Results and discussion ..... 45
*5.3.1 Mechanical performance of $Ti_2AlC$ and $Ti_3AlC_2$ ..... 45*
*5.3.2 Tribological behavior of $Ti_2AlC$ and $Ti_3AlC_2$ ..... 46*
*5.3.3 Wear track analysis ..... 47*
5.4 Conclusions ..... 52
**Chapter 6. Electro-tribological performance under electric current of $Ti_2AlC$ and $Ti_3AlC_2$ thin films ..... 53**
6.1 Introduction ..... 53
6.2 Experimental details ..... 53
*6.2.1 Electrical resistivity measurements of $Ti_2AlC$ and $Ti_3AlC_2$ thin films ..... 53*
*6.2.2 Setup of tribology under electrical currents of $Ti_2AlC$ and $Ti_3AlC_2$ ..... 53*
6.3 Results and discussion ..... 54
*6.3.1 Electrical properties of $Ti_2AlC$ and $Ti_3AlC_2$ ..... 54*
*6.3.2 Tribological performance under electrical current of $Ti_2AlC$ and $Ti_3AlC_2$ ..... 55*
*6.3.2.1 Tribology and electrical contact resistance of $Ti_2AlC$ thin film ..... 55*
*6.3.2.2 Tribology and electrical contact resistance of $Ti_3AlC2$ thin film ..... 58*
*6.3.2.3 Analysis of the balls used in the electro-tribological test. ..... 62*
6.4 Conclusions ..... 66
**General conclusion and future works ..... 68**
General conclusion ..... 68

Future works ..... 69
**Bibliography ..... 71**
**List of publications and conference presentations ..... 92**
List of publications ..... 92
Conference presentations ..... 92

# List of figures

**Figure 2.1** The periodic table with highlighted elements that make up the MAX phases, adapted from [81]. ..... 3

**Figure 2.2** MAX phase crystal structure, adapted from [78]. ..... 4

**Figure 2.3** Amplified surface roughness and different surface layers on the base material, adapted from [103]. ..... 6

**Figure 2.4** Schematic representation of a) sliding and b) rolling contact, adapted from [103]. ..... 7

**Figure 2.5** Friction coefficient as a function of the normal load. a) Steel sliding on an aluminum surface, b) a copper sliding on another copper and c) an AISI 440C stainless steel sliding on a $Ni_3Al$ alloy [103]. In all cases, the test was carried out under dry sliding conditions. ..... 8

**Figure 2.6** Schematic representation of the two break possibilities (1 and 2) during interface sliding, generating adhesive wear [103]. ..... 9

**Figure 2.7** Schematic representation of a) a rough hard surface or surface mounted abrasive particles sliding over a softer surface, and (b) free abrasive particles trapped between two surfaces with at least one of the surfaces softer than the abrasive particles [103]. ..... 10

**Figure 2.8** Schematic representation of abrasive particles impacting a surface at high speed [103]. ... 11

**Figure 2.9** Friction coefficient as a function of the ηU/W ratio for a lubricated sliding bearing: Stribeck curve. Where η is the lubricant viscosity, U is the peripheral speed of the components in contact, and W is the applied load [107]. ..... 12

**Figure 2.10** Schematic representation of tribometers used in tribological tests a) pin-on-disc, b) block-on-ring, c) pin-on-plate, d) twin disc, e) ring-on-ring, adapted from [107]..... 13

**Figure 2.11** Schematic representation of the fracture of a hard coating on a soft substrate [108,109]. 14

**Figure 2.12** Wear mechanisms caused by hard spherical counter-material sliding on coated surfaces. Four cases are considered: film hardness, thickness (a, b and f), surface roughness (a, c, e and g) and debris (a, d, e and h) [108,109]. ..... 15

**Figure 2.13** A bulk electrical contact is depicted in this diagram, adapted from [157]. ..... 21

**Figure 2.14** Schematic representation of the different contact areas, adapted from [160]. ..... 22

**Figure 2.15** (a) Near the electrical constriction, equipotential surfaces and current flow lines appear. The vertical axis of the vertical ellipsoidal surface is the parameter μ. The curves corresponding to the current

flow show the limits that enclose the current fraction. (b) Show a conducting cylinder of radius R with a circular constriction of radius a [160]. ..... 22

**Figure 2.16** Contact resistance as a function of the load applied to the gold electrical contacts [162]. 24

**Figure 2.17** Voltage as a function of temperature for copper-copper, aluminum-aluminum and brass-brass electrical contacts for $T_1$ temperatures of 20°C and 100°C [160]. ..... 25

**Figure 3.1** Schematic representation of the CS400ES Von Ardenne sputter cluster chamber equipped with three individual magnetrons and substrate holder of the Center for Micro and Nanotechnologies at TU Ilmenau, adapted from [164]. ..... 27

**Figure 3.2** Schematic representation of $Ti_2AlC$ and $Ti_3AlC_2$ thin film deposition. a) diffusion barrier and substrate and b) Ti-Al-C multilayer systems. ..... 27

**Figure 3.3** a) 1x1 cm square thin film samples after annealing for mechanical and tribological tests b) Thin films annealing temperature vs time. ..... 28

**Figure 4.1** a) Schematic representation of GD-OES measurement of thin films. Composition profiles as a function of the thickness of (b) Ti-Al-C multilayer systems, c) $Ti_2AlC$, and d) $Ti_3AlC_2$. ..... 31

**Figure 4.2** a) GI-XRD patterns and b) Raman spectra of $Ti_2AlC$ (blue color) and $Ti_3AlC_2$ (red color) MAX phase thin films obtained at 700°C and 950°C, respectively. ..... 32

**Figure 4.3** Crystal structure and lattice parameters of the MAX phases. a) $Ti_2AlC$ and b) $Ti_3AlC_2$. ..... 34

**Figure 4.4** a) Miller index obtained from data base PDF 29-0095 and b) crystallographic planes of $Ti_2AlC$. ..... 35

**Figure 4.5** a) Miller index obtained from data base PDF 52-0875 and b) crystallographic planes of $Ti_3AlC_2$. ..... 35

**Figure 4.6** BB-XRD diffraction patterns of a) $Ti_2AlC$ and b) $Ti_3AlC_2$, respectively. ..... 40

**Figure 4.7** Two-dimensional (2D) XRD 2θ-θ frames of a) $Ti_2AlC$ and b) $Ti_3AlC_2$, respectively. ..... 40

**Figure 4.8** The intensity changes in the gamma direction suggest that both films have preferential orientations. The relative texture coefficients for a) $Ti_2AlC$ and b) $Ti_3AlC_2$, respectively. ..... 41

**Figure 4.9** AFM images of the surfaces of a) $Ti_2AlC$ and b) $Ti_3AlC_2$ thin films, respectively. ..... 42

**Figure 5.1** Ball on flat reciprocating Micro-Tribometer Tetra–Basalt. a) a general view of the used tribometer and b) details of the test configuration. ..... 44

**Figure 5.2** a) Curves corresponding to the load-displacement and b) hardness as a function of the penetration depth of $Ti_2AlC$, $Ti_3AlC_2$ and pure silicon tested at 10 mN. ..... 45

**Figure 5.3** a) a) Schematic representation of the wear track resulting from the tribological tests. b) The CoF of $Ti_2AlC$ and $Ti_3AlC_2$ against 100Cr6 for different normal loads (connection lines are visual guides only)..... 46

**Figure 5.4** SEM-EDX analysis of $Ti_2AlC$ at 10 kV. SEM-micrographs of the wear track at a) 50, c) 250, and e) 500 mN. Track composition at b) 50, d) 250, and f) 500 mN. ..... 48

**Figure 5.5** SEM-EDX analysis of $Ti_3AlC_2$ at 10 kV. SEM-micrographs of the wear track at a) 50, c) 250, and e) 500 mN. Track composition at b) 50, d) 250, and f) 500 mN. ..... 50

**Figure 5.6** Wear track profiles measured by AFM after tribological tests using a normal of 500 mN for a) $Ti_2AlC$ and b) $Ti_3AlC_2$ (part of the track), respectively. ..... 51

**Figure 5.7** SEM micrographs of the kinking formation were observed in the wear track after tribological testing of $Ti_2AlC$ at 500 mN. ..... 52

**Figure 6.1** Schematic representation of the tribological test under electric current. ..... 54

**Figure 6.2** *Coefficient of friction and electrical contact resistance of $Ti_2AlC$ at 50 mN: a) 0, b) 10, c) 50, and d) 100 mA.* ..... 56

**Figure 6.3** *Coefficient of friction and electrical contact resistance of $Ti_2AlC$ at 500 mN: a) 0, b) 10, c) 50, and d) 100 mA.* ..... 57

**Figure 6.4** *SEM micrographs of the $Ti_2AlC$ tracks. a) 50 mN and 10 mA, and b) 500 mN and 100 mA.*58

**Figure 6.5** *Coefficient of friction and electrical contact resistance of $Ti_3AlC_2$ at 50 mN: a) 0, b) 10, c) 50, and d) 100 mA.* ..... 59

**Figure 6.6** *Coefficient of friction and electrical contact resistance of $Ti_3AlC_2$ at 500 mN: a) 0, b) 10, c) 50, and d) 100 mA.* ..... 61

**Figure 6.7** *SEM micrographs of the $Ti_3AlC_2$ tracks. a) 50 mN and 10 mA, and b) 500 mN and 100 mA.* ..... 62

**Figure 6.8** SEM micrographs and composition of the AISI 52100 ball after the electro-tribological test against $Ti_2AlC$ film at 500 mN and 100 mA. a) ball, b) contact region, c) enlarged of b), d) crack propagation, e) porous, and e) chemical composition of the contact region. ..... 63

**Figure 6.9** SEM micrographs and composition of the AISI 52100 ball after the electro-tribological test against $Ti_3AlC_2$ film at 500 mN and 100 mA. a) ball, b) contact region, c) enlarged of b), d) eroded area, e) porous and e) chemical composition of the contact region. ..... 65

**Figure 6.10** *General summary of CoF for a) $Ti_2AlC$ and b) $Ti_3AlC_2$, and the ECR for a) $Ti_2AlC$ and b) $Ti_3AlC_2$.* ..... 66

# List of tables

**Table 2.1** Coefficient of friction of bulk and thin films MAX phases against different counter materials. 16

**Table 4.1** Raman-active vibrational modes for $Ti_2AlC$ and $Ti_3AlC_2$ based on [172]..... 33

**Table 4.2** Values used for calculating the lattice parameters and the density of the $Ti_2ALC$ phase..... 36

**Table 4.3** Process for obtaining the lattice parameters and the density of $Ti_2AlC$ thin film. ..... 37

**Table 4.4** Values used for calculating the lattice parameters and the density of the $Ti_3ALC_2$ phase..... 37

**Table 4.5** Process for obtaining the lattice parameters and the density of $Ti_3AlC_2$ thin film. ..... 38

**Table 4.6** Lattice parameters and density of bulk MAX phases from literature and thin films of this work. ..... 39

**Table 6.1.** Electrical resistivity and hardness of $Ti_2AlC$ and $Ti_3AlC_2$ MAX phases. ..... 55

# List of symbols and abbreviations

| | |
|---|---|
| a | Radius |
| $A_c$ | Mechanical contact area |
| AFM | Atomic force microscopy |
| Al | Aluminum |
| $A_w$ | Atomic weight |
| C | Carbon |
| CoF | Coefficient of friction |
| CVD | Chemical vapor deposition |
| $d_{hkl}$ | Interplanar distance |
| F | Force |
| GD-OES | Glow discharge optical emission spectroscopy |
| H | Hardness |
| hkl | Miller index |
| N | Nitrogen |
| $N_A$ | Avogadro's number |
| MAX | $M_nAX_{n+1}$ phases |
| PDF | Powder diffraction file |
| PVD | Physical vapor deposition |
| $R_c$ | Constriction resistance |
| $R_s$ | Spreading resistance |
| RTC | Relative texture coefficient |
| RTP | Rapid thermal processing |
| $R^2$ | Coefficient of determination |
| Si | Silicon |
| Ti | Titanium |
| $T_m$ | Maximum temperature |
| $T_1$ | Initial temperature |
| U | Peripheral speed |
| W | Applied normal load |
| W | Weight |
| XRD | X-ray diffraction |
| V | Volume |

| | |
|---|---|
| θ | Angle |
| η | Lubricant viscosity |
| ρ | Resistivity of electrical conductor |
| μ | Coeficcient of friction |
| ρ | Density |
| ω | Angular velocity |
| ω | Wavenumbers |

# Chapter 1. Introduction and Motivation

The phases $M_{n+1}AX_n$ (abbreviated as MAX) have received worldwide attention due to their outstanding properties. MAX phases are well known for their interesting combination of metallic and ceramic materials properties [1,2]. MAX phases have high thermal and mechanical resistance and good electrical and thermal conductivity [3]. MAX phases were initially synthesized and studied by Nowotny et al. in the early 60s and 70s of the last century [4,5]. Since then, more than 150 types of MAX phases have been discovered [6]. Since the previous decade, MAX phases have also been used as precursors for 2D MXenes [7]. Due to this property combination and versatility, MAX phases have attracted considerable interest in applications such as protective coatings, electrical contacts [8] and structural materials in corrosive media [9]. Due to their ceramic-like thermal stability and corrosion resistance in a harsh environment, they are also interesting for high-temperature applications [10]. Considering the fascinating combination of properties and the growing scientific interest in these materials. This thesis aims to evaluate the tribological, mechanical and electro-tribological properties of $Ti_2AlC$ and $Ti_3AlC_2$ films for possible applications such as protective coatings and electrical contacts.

For various industrial uses, coatings and thin films have become one of the most valuable protective materials against friction and wear. Since 23% of the world's total energy is required to mitigate friction and wear, the field of tribology, which includes friction, wear, and lubrication, has a substantial impact on society [11]. Finding materials and material combinations with low friction (coefficient of friction - CoF), a low wear rate, and a long lifetime is one of the main goals of tribological research. Various procedures concerning surface modifications and coating systems have been investigated to enhance the tribological performance of machine components. This procedure includes diamond-like carbon coatings systems [12–16], transition metal dichalcogenides ($MoS_2$ and $WS_2$) [17–20], different multilayers coating systems [21–28], MAX phases as potential coating materials [29–37], 2D materials as solid lubricants [38–40], and surface modification and textured patterns [41–47].

MAX phases have good electrical conductivity and tribological performance [48–61]. Thus, the MAX phases could be used as sliding electrical contacts [8,62–64]. The performance of sliding electrical contacts is strongly influenced by properties such as electrical conductivity and tribological behavior [60,65]. Moreover, adequate wear control is critical to sliding contact reliability [61,66–68]. Electrical contacts are generally subjected to various levels of mechanical load, excessive friction and wear, micro-welding, corrosion, and electrical arc erosion, resulting in poor electrical contact performance and a short life cycle [61,69–71]. Commonly, electrical contacts are coated with noble and soft metals such as gold, palladium, silver, and other noble metals and their alloys [67,70–72]. Thus, a larger contact area is formed

due to the ductile nature of noble metals. This offers low electrical contact resistance or good electrical conductivity and provides protection against corrosion. However, in sliding contacts (non-stationary), the larger contact area generates high friction and excessive adhesive and abrasive wear of the electrical contact [60,73]. Several studies on sliding contacts have been reported emphasizing wear mechanisms such as adhesive wear, abrasive wear, arc ablation, oxidative wear, and arc contact erosion [74–77]. However, it is still necessary to go through the subject and find additional ways to coat sliding electrical contacts. The low coefficient of friction and low wear rate should prevail, and good electrical behavior should be comparable to standard metallic coatings. In this regard, the MAX phases could be an excellent alternative to be used as sliding electrical contacts.

Considering the topics discussed in the previous paragraphs and taking into account the importance of the MAX phase in applications such as protective coatings and sliding electrical contacts. This thesis, in the first part, investigates the synthesis and characterization of the $Ti_2AlC$ and $Ti_3AlC_2$ phases thin films. These films were obtained from the same precursor formed by Ti-Al-C multilayers and subsequent annealing treatment. The formation of the thin films was verified by various experimental techniques such as XRD, GD-OES and Raman spectroscopy. Afterwards, the mechanical and tribological properties of these MAX phases were investigated. The tribological behavior of these MAX phases was correlated with the mechanical properties, texture, grain size and surface roughness. It can be observed that the $Ti_2AlC$ phase is harder and has better tribological performance than the $Ti_3AlC_2$ phase. Finally, the electrical conductivity of the $Ti_3AlC_2$ phase is higher than that of the $Ti_2AlC$ phase. However, the $Ti_2AlC$ film remains complete after the electro-tribological test at currents of 50 mA. In contrast, the $Ti_3AlC_2$ phase suffers a considerable film deterioration at a current flow of 50 mA. The different performance of both phases is related to their respective mechanical properties and tribological behavior.

# Chapter 2. Fundamental Theory and State of the Art

## 2.1 $M_{n+1}AX_n$ phase materials

This chapter introduces an overview of MAX phases' crystal structure, synthesis process, and mechanical and tribological performance. The crystal structure is closely connected to its tribological and mechanical properties. On the other hand, different synthesis routes have been developed depending on their physical form, such as hot isostatic pressing and physical vapor deposition for bulk and thin films, respectively. More information on this topic can also be found at Barsoum [78], Eklund et al. [1], Sokol et al. [79], Berger [80] and others.

### 2.1.1 The structural properties of MAX phases – Crystal structure

MAX phases are ternary carbides and nitrides with the general formula $M_{n+1}AX_n$ (thus in short MAX) where n could take different values such as (n=1, 2 or 3); M is an early transition metal. A is an element of group A and X is C and/or N (see the periodic table shown in Figure 2.1). These phases represent a new class of solids with a hexagonal nanolayered crystal structure (see Figure 2.2). Up to now, more than 150 MAX phases [6] have been synthesized, and all of them share a similar crystal structure and chemical composition [78].

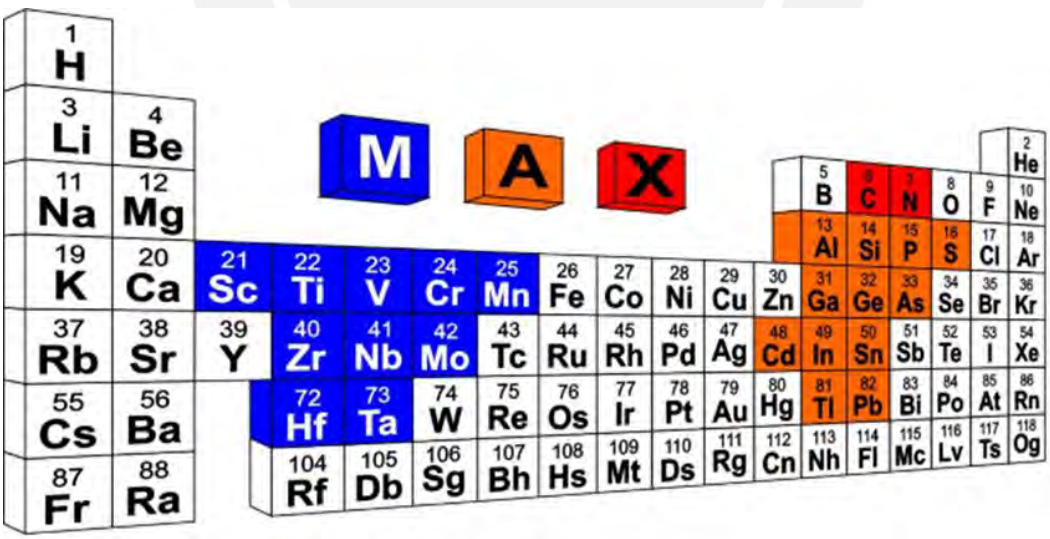


***Figure 2.1*** *The periodic table with highlighted elements that make up the MAX phases, adapted from* [81].

The MAX phases generally have unique properties that make them attractive in multiple applications. These phases behave as metallic and ceramic materials at the same time [78,82,83]. They have good electrical and thermal conductivity, are machinable and resistant to thermal shocks [48,50]. In addition, they are resistant to corrosion and aggressive environments and retain their mechanical properties at high temperatures [64,84].

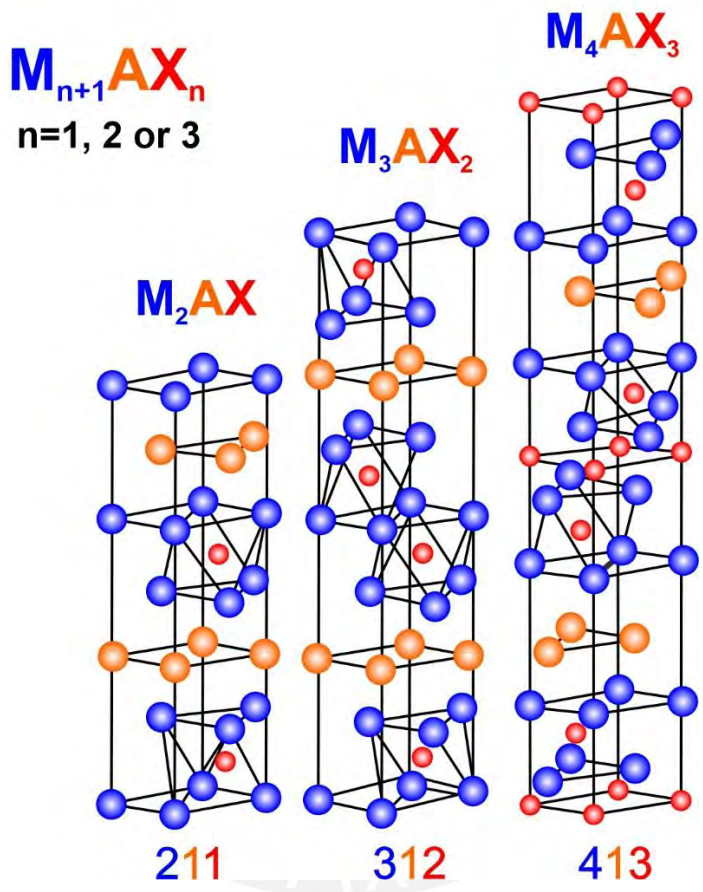


***Figure 2.2*** *MAX phase crystal structure, adapted from* [78].

### 2.1.2 The MAX phases processing techniques

MAX phases can be found in the form of bulk material and thin films. Bulk materials are generally obtained from powders or some other precursors. The starting materials are often subjected to pressure and high temperatures to densify them. Among the techniques used to obtain bulk material are hot pressing [57], hot isostatic pressing [49,85], plasma spark sintering [86–88], sol-gel processes [89], and sintering without pressure [90]. Furthermore, the MAX phase thin films can be obtained through different techniques such as chemical vapor deposition (CVD) [91], pulsed laser deposition [92], physical vapor

deposition (PVD) such as magnetron sputtering with alternating and direct current [30,93,94] or radiofrequency [95] and high-power impulse magnetron sputtering [96].

Hot pressing is the most widely known bulk MAX phase synthesis method, and materials with high density and purity can be obtained. The starting materials need to be particulate or pulverized, and this is poured into graphite molds and pressed at high temperatures. The synthesis pressure can reach up to 50 MPa, and the maximum temperatures range between 1200 and 1500°C [6]. Below is a review of some bulk MAX phases that were synthesized by hot pressing. These are $Ti_2AlC$ [57], $Ti_3AlC_2$ [97] and $Ti_3SiC_2$ [98].

In this thesis, the synthesis process of magnetron sputtering is used. This technique allows exact control of the thickness of the deposited film, films with low contamination and high-quality films can be obtained [1,99]. Furthermore, MAX phase thin films offer a series of benefits, such as reduced production costs due to the minor amounts of material used, design flexibility, and excellent surface finish, among others [100–102].

## 2.2 Fundamentals concepts of tribology

### 2.2.1 Roughness and characteristics of solid surfaces

The roughness and surface properties of solids are an essential part of the study of tribology. The surface interaction of solid surfaces can affect friction, wear, real contact area, lubrication, thermal and electrical conductivity, optical properties, and appearance. Regardless of the manufacturing method, all surfaces exhibit irregularities or geometric deviations. These irregularities range from interatomic distances to macroscopic variations in shape [103]. It is worth mentioning that no machining or manufacturing process produces completely flat surfaces.

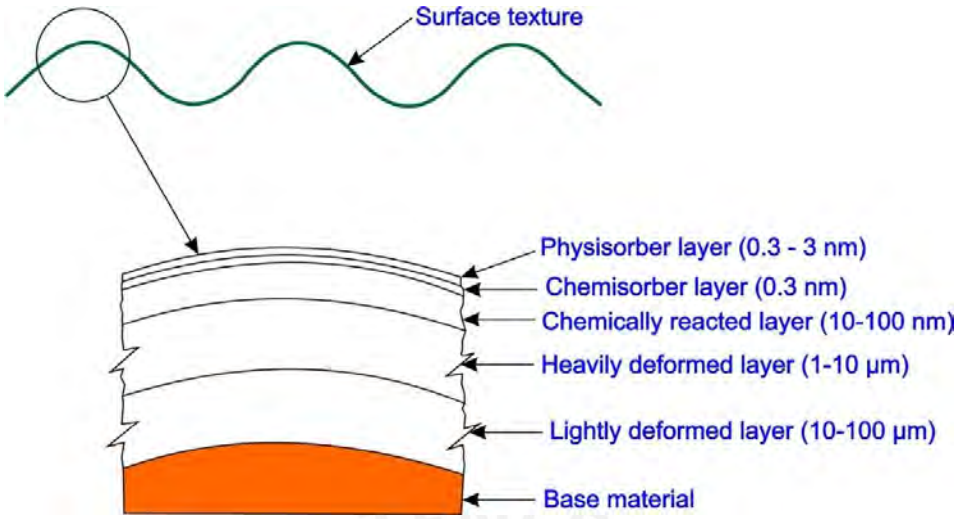


**Figure 2.3** *Amplified surface roughness and different surface layers on the base material, adapted from* [103].

Figure 2.3 shows a solid surface with various layers. These layers usually have characteristic physicochemical properties of the base material. The first two layers over the base material are formed due to the manufacturing or machining process used during its formation. These layers are usually deformed or work-hardened. These layers have different properties than the base material.

Moreover, surfaces are generally reactive when they interact with the environment. That is, layers of certain oxides can form on surfaces. Layers can also be generated by chemisorption or physisorption of oxygen and water vapor from the surrounding medium [104]. The surface tension should be considered apart from the films formed on the surface.

### 2.2.2 Friction under dry sliding conditions

Friction is a force that opposes the relative motion during the sliding or rolling of two surfaces in contact (see Figure 2.4). Friction is not an intrinsic property of materials but rather a response to a tribological system. The tribological system usually contains materials in contact, applied normal force, sliding speed, surface roughness, mechanical properties and environmental conditions. The typical classification of friction comprises dry friction and liquid friction. This section will address only dry friction or "Coulomb" friction. Dry friction occurs when two dry surfaces come into contact under relative motion. Generally, when two smooth and clean surfaces are in contact, the value of the friction force is usually high. On well-lubricated surfaces, the adhesion and friction force are generally weak, although a small amount of liquid on smooth surfaces could cause an increase in friction force.

Depending on the application, friction can be beneficial or detrimental. Some examples of positive friction are vehicle brakes, machining and polishing components, conveyor belts or power transmission by friction, and walking on ice. In the previously mentioned examples, the aim is to increase the value of the

friction force. However, in some applications, friction is undesirable, such as in bearings, gears, cams, and mechanical components in sliding or rotating contact motion. In the previously discussed applications, the value of friction coefficient should be controlled and minimized.

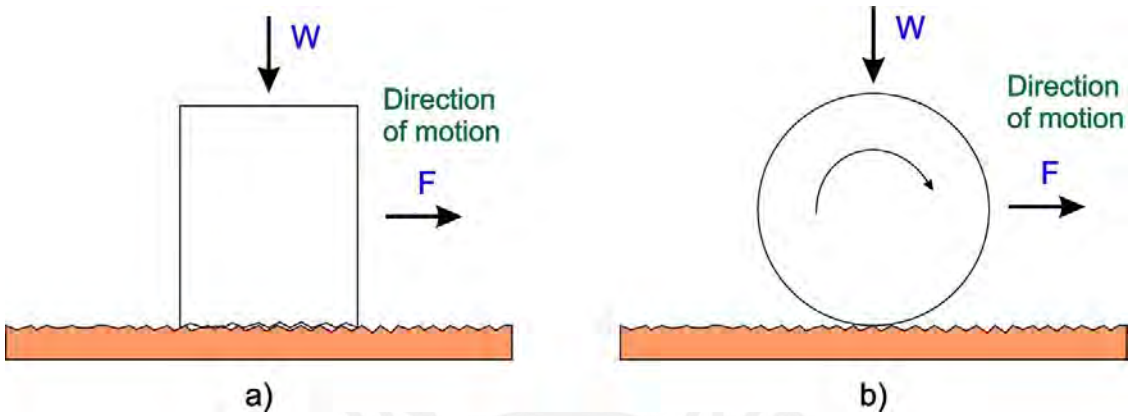


**Figure 2.4** *Schematic representation of a) sliding and b) rolling contact, adapted from* [103].

Friction is usually measured by the coefficient of friction (μ or CoF). CoF is a quantitative and empirical parameter which should be measured by experimental tests. It is impossible to find the CoF only by mathematical or numerical calculations. The coefficient of friction can be static ($\mu_s$) or kinetic ($\mu_k$) and is independent of the normal load. The coefficient of friction is a scalar value given by Equation 2.1.

$$\mu = \frac{F}{W} \tag{2.1}$$

Where F is the friction force, and W is the normal force.

Coulomb (1785) states that when two objects are in relative motion, the force of kinetic friction is independent of the sliding speed. It is worth mentioning that the rules correlated with friction are entirely empirical. That is to say, in the cases in which they are not fulfilled, it does not imply a violation of the fundamental laws of nature [103].

Figure 2.5 shows the variation of the coefficient of friction as a function of the normal force. In general, three different behaviors can be seen. Figure 2.5a) shows the variation of the coefficient of friction as a function of the normal load of the steel against the aluminium. Under these conditions, the coefficient of friction remains constant at around 1.3. However, in the case of copper against copper, it is observed that the coefficient of friction depends on the normal load (see Figure 2.5b)). At low loads, a coefficient of friction of 0.4 can be seen. This value increases with the increasing normal load. The coefficient of friction undergoes a transition to stabilize at an approximate value of 1.8 for loads greater than 1 N. Some factors responsible for this behavior may be that the oxide film on the copper surface at low loads

decreases the metal-to-metal contact, reducing the contact area. The oxide film breaks down at high normal forces, causing metal-to-metal contact. Considering that copper is a soft material, a larger contact area causes the coefficient of friction and surface damage to increase. In some cases, at high normal forces, the coefficient of friction decreases (see Figure 2.5c)), and the formation of tribo-films could cause a reduction in the coefficient of friction.

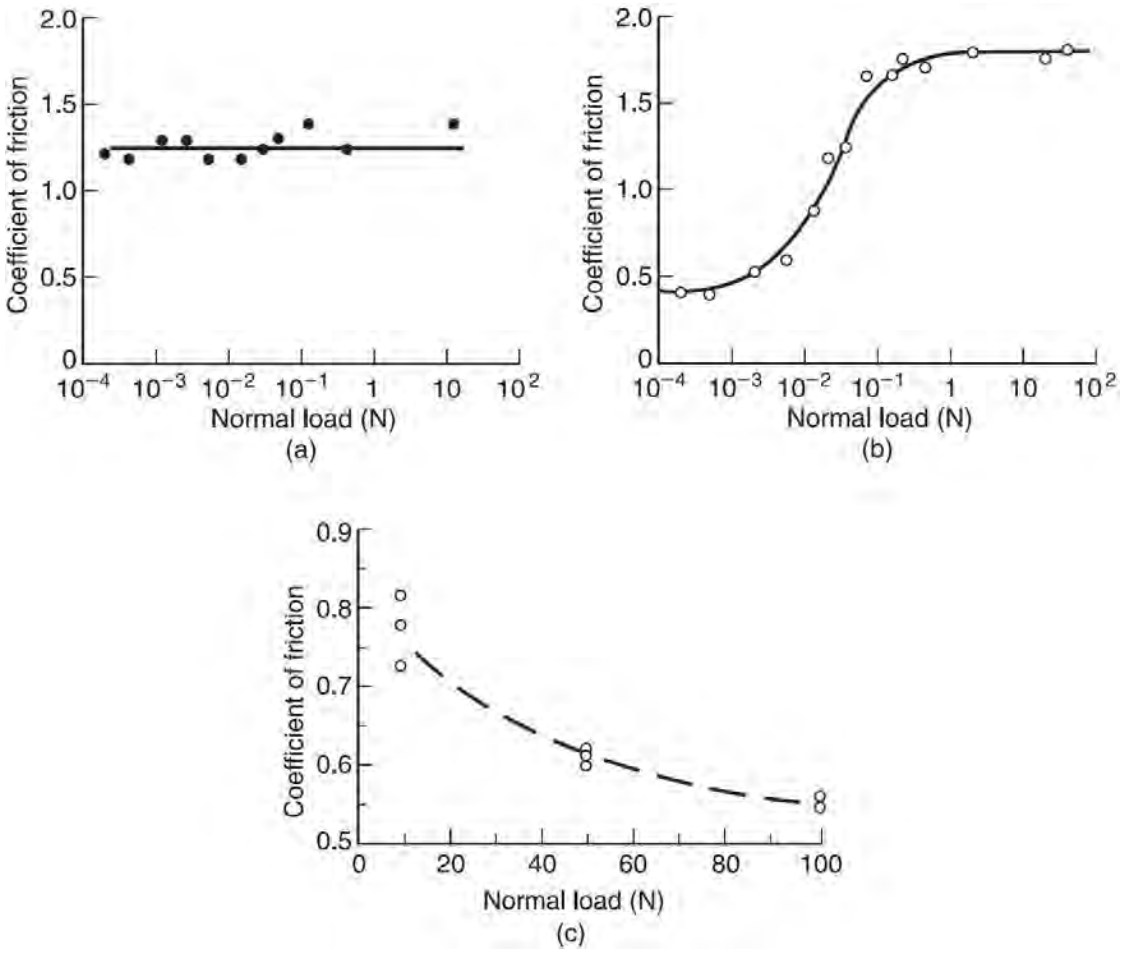


**Figure 2.5** *Friction coefficient as a function of the normal load. a) Steel sliding on an aluminum surface, b) a copper sliding on another copper and c) an AISI 440C stainless steel sliding on a $Ni_3Al$ alloy* [103]*. In all cases, the test was carried out under dry sliding conditions.*

As mentioned before, the coefficient of friction is not an intrinsic property of the material but depends on many factors, such as sliding, materials and environmental conditions. Friction also involves energy dissipation during sliding. When two surfaces are in contact, only the tips of the asperities come into contact, and the applied load causes deformation of the asperities, forming discrete contact points. In the vicinity of the contact points, adhesive forces are formed caused by physicochemical interactions of the

contact interface and the environment. Then friction occurs due to adhesion and deformation. Adhesive forces are present at all contacts and depend on the conditions of the contact interface. A traditional method used to reduce friction is to use protective coatings with low interface shear strength.

### 2.2.3 Wear mechanisms

Wear appears when two surfaces are in contact and relative movement. It is characterized as a continuous process of interface deterioration. Mechanical components fail mainly due to wear, fatigue and corrosion. Wear is one of the most important factors because wear can cause between 60 to 80% of the total volume of failures [105]. Given its importance in saving resources and energy, it is imperative to know the wear mechanisms and the actions that must be taken to reduce wear.

#### Adhesive wear

Adhesive wear occurs when contact surfaces move against each other, causing particles to be removed from the contact surface. The adhesive bond is formed when asperities are cut, resulting in particles or fragments of one of the surfaces. These particles adhere to the other surface in contact (see Figure 2.6). This operation is repeated multiple times, and the transfer or migration of material due to adhesive wear can change between the surfaces in contact. Sometimes, the transferred material comes off, and the presence of loose particles can be seen on the track.

Adhesive wear is calculated using the model proposed by Archard (1953) [106]. In Equation 2.2, the contact area is assumed to be circular points, and each has a radius a. From this idealization, it is established that the contact area is πa2. Each contact point supports a normal load of:

$$W = \pi a^2 H \tag{2.2}$$

H is the hardness of the softer material in the tribological contact interface.

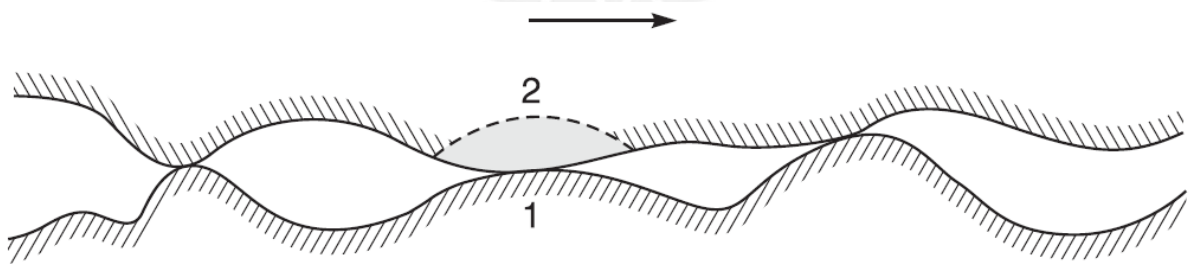


**Figure 2.6** *Schematic representation of the two break possibilities (1 and 2) during interface sliding, generating adhesive wear* [103].

**Abrasive wear**

Abrasive wear occurs when a rough, hard surface or trapped hard particles slide over a soft surface, this interaction damages the contact interface by plastic deformation or fracture. Material loss in ductile materials occurs by plastic deformation, while in brittle materials, it occurs by brittle fracture. Both cases shown in Figure 2.7 have practical applications. In the first case, the hard surface slides over a softer one. This can be seen in metal removal machinings such as turning, milling, and drilling. The second case is when hard and abrasive particles are trapped in the contact interface (also known as three-body abrasion). This case can be observed in the operations of lapping or polishing materials.

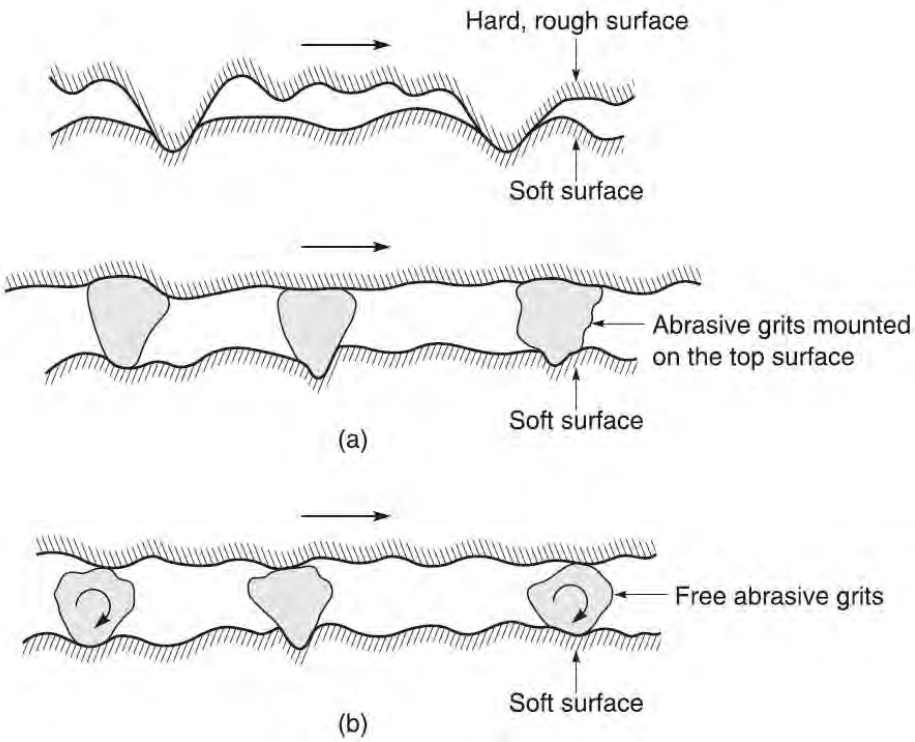


**Figure 2.7** *Schematic representation of a) a rough hard surface or surface mounted abrasive particles sliding over a softer surface, and (b) free abrasive particles trapped between two surfaces with at least one of the surfaces softer than the abrasive particles* [103].

**Fatigue wear**

In tribological systems, fatigue wear is produced by the formation and growth of surface or subsurface cracks due to the action of a large number of load and unload cycles. The superficial rupture causes the detachment of large fragments, causing large biting in the contact interface. Crack formation usually takes a short time. However, crack propagation can be quite slow [105]. Load and unload cycles before a fatigue failure is typically in the order of thousands or millions of cycles, so wear is negligible before

fatigue failure. This characteristic distinguishes fatigue wear from adhesive or abrasive wear, where material loss is gradual and progressive during tribological contact performance. The above shows that the wear rate is not an adequate parameter to measure fatigue wear. It is more convenient to predict the lifetime of the tribological system in terms of the number of cycles before failure occurs.

**Erosion wear**

Erosion wear occurs when hard particles impact a solid surface (see Figure 2.8). Wear can be caused by plastic deformation (ductile materials) or fracture (brittle materials). Erosive wear differs from abrasive wear because erosion considers the kinetic energy of hard particles impacting the study surface. For ductile materials, maximum erosion occurs at an impact angle of 20°, while for brittle materials, the degree and severity of wear are influenced by the shape of the abrasive particles [104]. Erosion-generated debris forms due to repeated impacts.

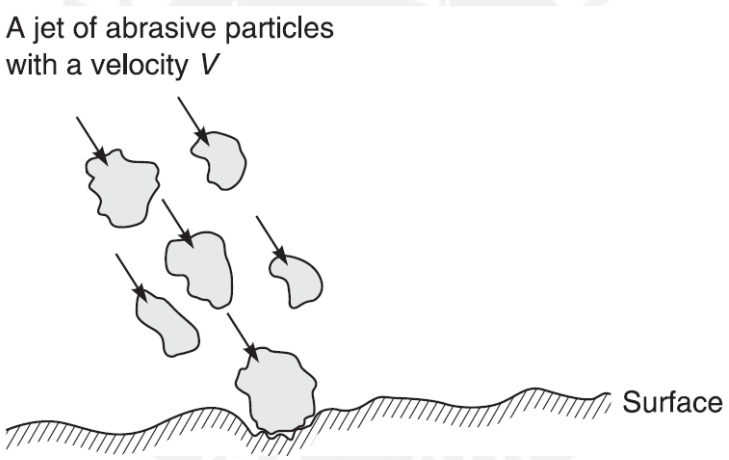


**Figure 2.8** *Schematic representation of abrasive particles impacting a surface at high speed* [103].

**Corrosive/Oxidative Wear**

Corrosive/oxidative wear occurs when the tribological system is in a corrosive environment. Oxygen is the most dominant corrosive component of air. In static contacts, oxide films typically form on a surface less than a micron thick. However, the progressive wear of the tribological system generates new areas for the corrosive attack to continue. In many cases, forming oxides on the surface can be beneficial. Because the film isolates the metal-to-metal contact, reducing the adhesion forces and consequently lowering the friction coefficient and the wear rate.

### 2.2.4 Lubrication regimens

Mechanical contact between two solid sliding surfaces can produce a high coefficient of friction and a high wear rate. However, the addition of lubricant can significantly reduce friction and wear. The proper choice of lubricant based on operating conditions requires knowledge of the Stribeck curve. Figure 2.9 shows the lubrication regimes in which the mechanical components could work.

Hydrodynamic lubrication is when two sliding surfaces become separated by a lubricant film. The thickness of the lubricant film usually ranges from 5 to 500 μm. This film is thicker than the surface roughness, and there is no physical contact between the asperities. The coefficient of friction in this regime is usually low. However, it can increase slightly with increasing the sliding speed. Elastohydrodynamic lubrication is a subset of the hydrodynamic regime. The thickness of the film can vary between 0.5 and 5 μm; in certain areas, the asperities can touch. Mixed lubrication is a combination of hydrodynamic and boundary lubrication. In this regime, there may be frequent asperity contacts. In boundary lubrication, as the speed decreases or the applied load increases, as shown by the Stribeck curve (see Figure 2.9), the coefficient of friction increases significantly. In this regime, the film cannot separate both surfaces in contact.

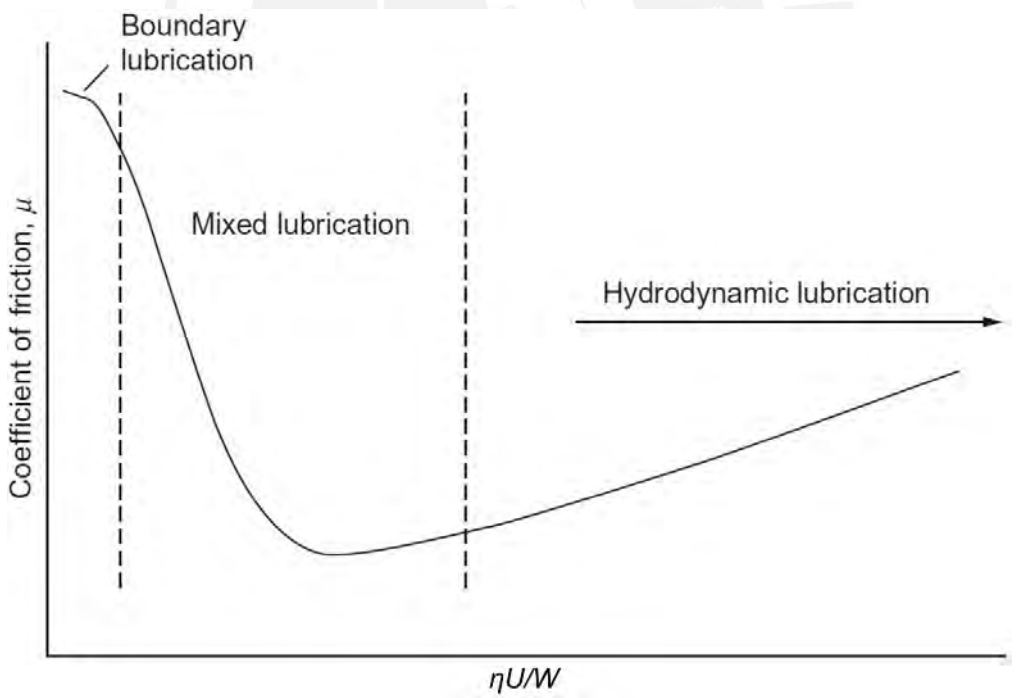


**Figure 2.9** *Friction coefficient as a function of the ηU/W ratio for a lubricated sliding bearing: Stribeck curve. Where η is the lubricant viscosity, U is the peripheral speed of the components in contact, and W is the applied load* [107].

### 2.2.5 Types of tribometers

The coefficient of friction and the wear rate must be determined experimentally. For this purpose, many types of tribometers have been developed. Figure 2.10 shows schematic representations of the most commonly used tribometers. These tests allow the simulation of tribological systems, estimate the coefficient of friction, examine the wear mechanisms and quantify the wear rate. The parameters analyzed, such as the coefficient of friction and the wear rate, are a response of the tribological system and not just the material itself.

The most commonly used tribometers are the pin-on-disc (Figure 2.10a), block-on-ring (Figure 2.10b), and pin-on-reciprocating plate (Figure 2.10c). The three cases mentioned above are asymmetrical in load application, so repeatability is challenging. In the cases of twin discs and ring-on-ring, the angular velocities must be different (Figure 2.10d and e). These last two cases are symmetric cases making $\omega_1 = -\omega_2$. The ring-on-ring configuration allows all points on the surfaces to remain in contact throughout the entire test [107].

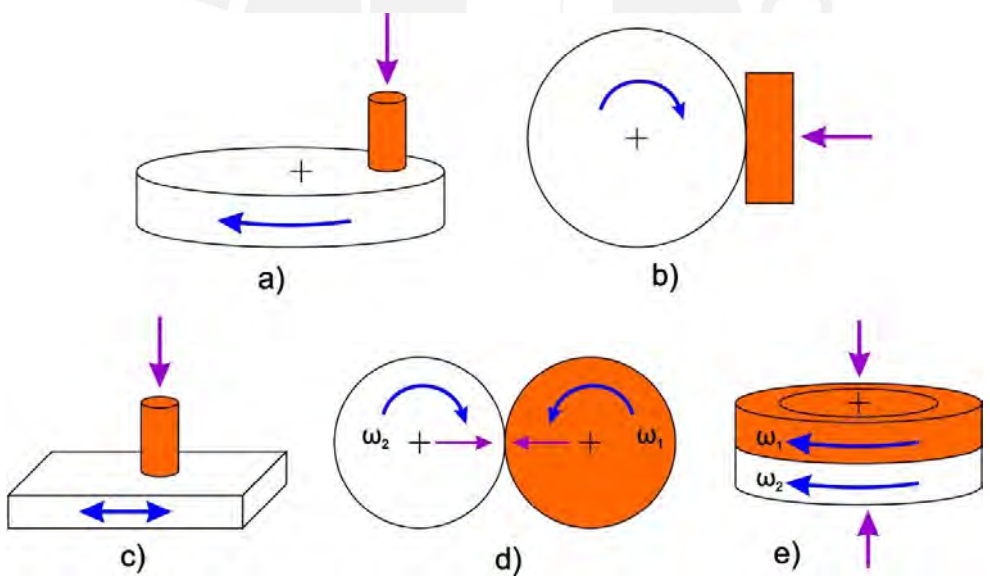


**Figure 2.10** *Schematic representation of tribometers used in tribological tests a) pin-on-disc, b) block-on-ring, c) pin-on-plate, d) twin disc, e) ring-on-ring, adapted from* [107].

## 2.3 Tribology of coatings and thin films

The tribology of coatings and thin films is influenced or governed by four essential parameters: coating hardness, coating thickness, surface roughness, and the size and hardness of external debris or debris

generated in the tribological contact. The combination of these parameters defines the tribological behavior of the coatings. Depending on the tribo-pair conditions, different wear mechanisms can be observed. Figure 2.12 shows schematic representations of 12 typical tribological contacts of a hard sphere against a coating [108,109].

The relationship between the hardness of the coating and the substrate is an important parameter in the tribological study of thin films or coatings. Two cases can be discussed for better analysis: hard and soft coatings (see Figure 2.12). Bowden and Tabor [110] suggest that a soft coating reduces the friction coefficient, but wear could be excessive. A hard coating on a softer substrate can decrease the coefficient of friction and excessive wear by preventing ploughing [111]. That is why hard coatings are used in abrasive environments. The diamond-like carbon (DLC) coatings are perhaps the most widely used and studied coatings [112]. Multilayer coatings offer great possibilities for manipulating mechanical and tribological properties according to the required application conditions [23].

Coatings typically separate the substrate from the counter material, reducing friction and wear. However, if the substrate is soft, it cannot support the applied load [113]. Thus, the film would no longer fulfill its designed function (see Figure 2.11). The appropriate solution to this problem is to find the correct thickness according to the working conditions to which it will be subjected.

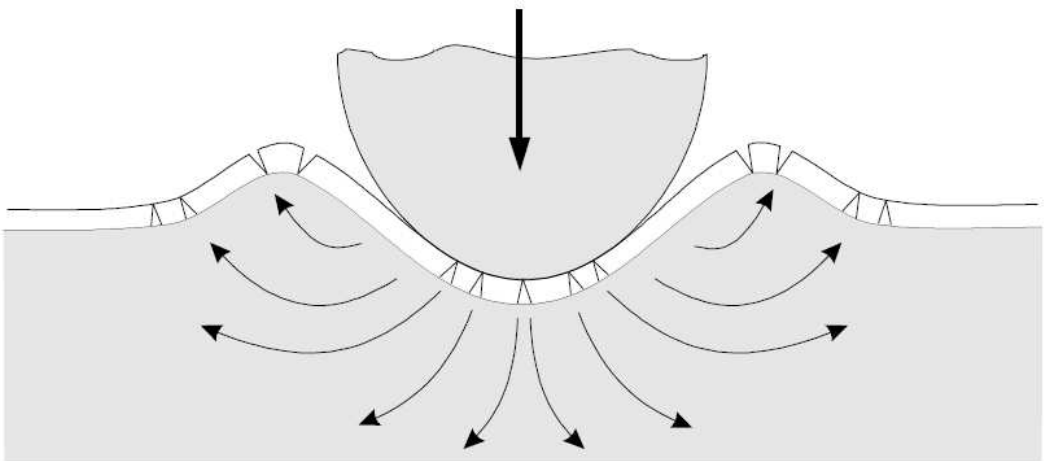

**Figure 2.11** *Schematic representation of the fracture of a hard coating on a soft substrate* [108,109].

Roughness at different scales is always present on all surfaces, depending on the type of deposition or method used to obtain the thin film. The substrate roughness can be reflected in the surface roughness of the coating. Moreover, hard asperities can scratch the contact interface during sliding, causing an increased friction coefficient and abrasive wear. However, rough surfaces can also reduce the real contact area and thus reduce friction (see Figure 2.12a), b), and f)). Debris can be generated during

sliding contact. The origin of this debris may be the wear of the tribo-pairs themselves, or it may result from the surrounding environment. The effect of debris on tribo-pairs can be mild or severe (see Figure 2.12a), d), e), and h)). These effects depend on factors such as the size and hardness of the debris, the hardness relationship between the coating and the substrate, surface roughness and thickness of the films or coatings.

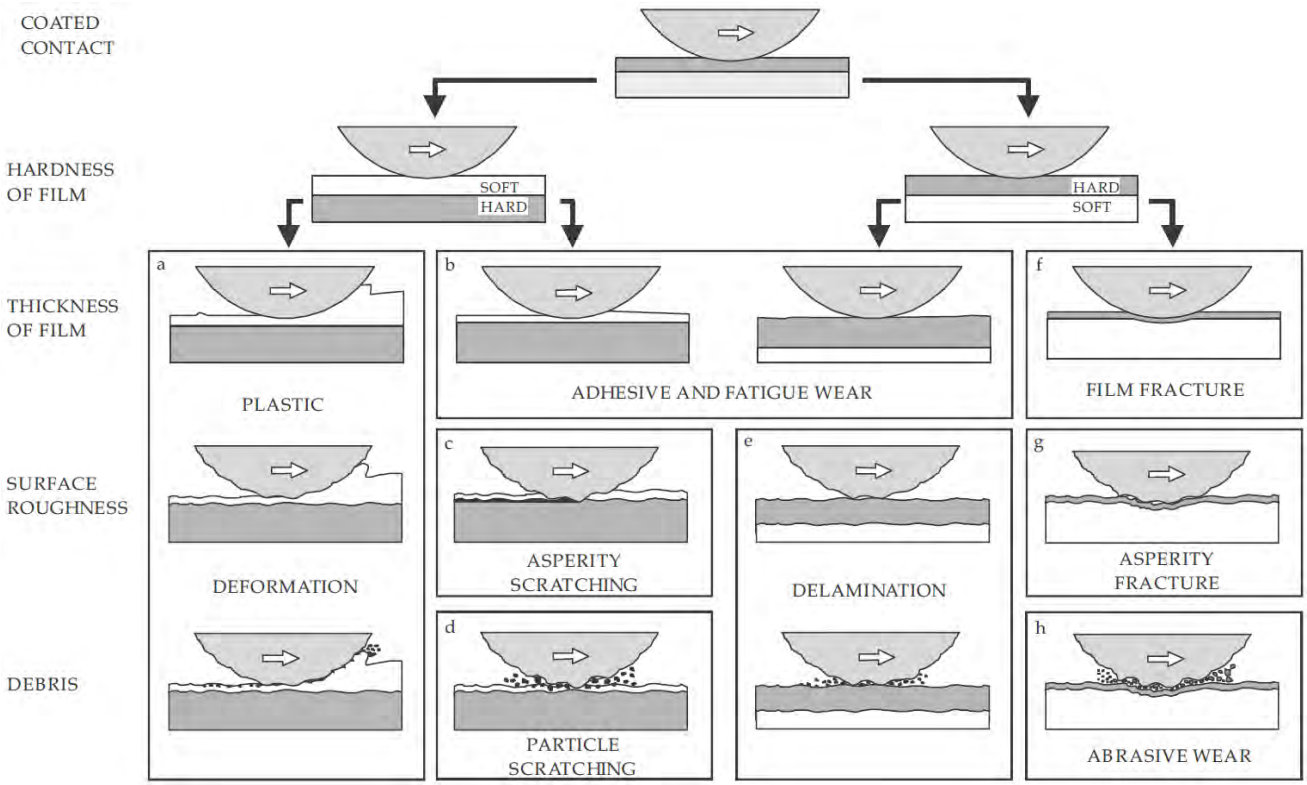


**Figure 2.12** *Wear mechanisms caused by hard spherical counter-material sliding on coated surfaces. Four cases are considered: film hardness, thickness (a, b and f), surface roughness (a, c, e and g) and debris (a, d, e and h)* [108,109].

## 2.4 Tribology of MAX phases

**Table 2.1** summarizes the publications related to the tribology of MAX phases and compounds based on MAX phases. It can be seen that MAX phases were intensively investigated using a wide variety of counter materials such as bearing steel, alumina, SiC, AISI 316L, and low carbon steels, including the same material or other types of MAX phases as counter material. The applied normal forces were found to vary from 0.05 to 106 N. In addition, a wide variation of the sliding speeds can be seen, ranging from $5*10^{-5}$ to 60 m/s. The range of reported coefficient of friction values varies from 0.10 to 1.22. The MAX

phases were not only analyzed under dry sliding conditions but also under lubrication conditions such as deionized water, seawater, argon, etc. The main wear mechanisms reported are abrasive wear, third-body abrasion, adhesive wear, oxidation wear, and others. Another essential aspect of MAX phase tribology is that MAX phases are used as components to form composite materials. This is done to improve the tribological performance of these materials.

**Table 2.1** *Coefficient of friction of bulk and thin films MAX phases against different counter materials.*

| $M_{n+1}AX_n$ phases | Counterpart | Applied force (N) | Sliding speed (m/s) | Friction coefficient (μ) | Wear mechanisms | Ref. |
|---|---|---|---|---|---|---|
| $Ti_3SiC_2$, $Ti_2AlN$ y $Cr_2AlC$ | Bearing steel 100Cr6, ball (Ø 2.8mm) | 0.05 N and 0.125 N | 0.00005 and 0.00008 m/s | 0.15-0.25, 0.15-0.5 and 0.3-0.7 | Adhesive wear | [114] |
| $Ti_3SiC_2$ | Alumina balls (6mm) | 0.0001 N to 0.24 N | 0.05 m/s | 0.1 to 0.8 | Third body abrasion | [115] |
| $Ti_3AlC_2$ | Ball SiC, (Ø6.35mm) | 20, 40, 60 and 80 N | - | **In deionized water:** 1Hz(0.3), 5Hz(0.15) y 10Hz(0.08) **In sea water:** 1Hz(0.18), 5Hz(0.14) and 10Hz(0.1-0.05) 20N | Tribo-chemical wear | [116] |
| $Ti_3AlC_2$ | Balls AISI 316L (Ø 6 mm), $Al_2O_3$, $Si_3N_4$ and SiC all with (Ø 6.35 mm) | 20 N | 0.05 m/s | **In deionized and seawater:** ($Al_2O_3$, $Si_3N_4$: 0.52-0.60, 316L:0.53-0.56 and SiC:0.15) | Two and three-body abrasive wear | [117] |
| $Ti_3AlC_2$ | Ball SiC, (Ø6.43mm) | 4.9 N | 0.2 m/s | **In air:** 25°C(0.51), 400°C(0.77) and 1000°C(0.52) **In Argon:** 25°C(0.76), 600°C(1.02) and 1000°C(0.60) | Tribo-films was formed | [118] |
| $Ti_3SiC_2$/SiC | Hemispherical pin of $Ti_3SiC_2$/SiC (Ø4mm) | 0.49 N | 0.04 m/s | Dry (≈0.9), Water (≈0.8) and $C_2H_5OH$ (≈0.2) | Oxidation wear, abrasive wear and tribo-oxidation | [119] |
| $Ti_3SiC_2$ | Ball $Si_3N_4$ (Ø10mm) | 20, 50, 70, 100, 150N | 15Hz, 1mm, 30min | 0.1-0.4 | Decoherence and tribo-chemistry | [120] |
| $Ti_3SiC_2$ | $Ti_3SiC_2$, $Al_2O_3$, $Si_3N_4$, SiC, and bearing steel, 100Cr6, (Ø10mm) | 34 N | - | Against ($Ti_3SiC_2$: 1.08; Si3N4: 1.17; $Al_2O_3$: 1.30; Steel: 0.63; SiC: 0.43) | Mechanical wear and oxidative wear | [121] |
| $Ti_3SiC_2$ | AFM tip | $\Delta F_N = k_N \Delta_z$ | - | $2x10^{-3}$-0.25 | - | [122] |
| $Ti_3AlC_2$ | Ball of alumina $Al_2O_3$ (Ø9.525mm) | 20 N | - | - | Mechanical wear and tribo – oxidation | [123] |

| | | | | | | |
|---|---|---|---|---|---|---|
| $Ti_2AlC$ y $Ti_2AlSn_{0.2}C$ | Low carbon steel (Ø300x10mm) | 20-80 N | 10-30 m/s | 0.3-0.45 and 0.25-0.35 | - | [124] |
| $Ti_3Al_{0.8}Si_{0.2}Sn_{0.2}C_2$ | S45C steel (AISI 1045) (Ø300x10mm) | 20-80 N | 5-30m/s | 0.17-0.53 | - | [125] |
| $Ti_3Si\ C_2$ | Bearing steel (Ø 16 mm) | 7.7 to 14.7 N | 7 m/s | 7.7N(0.4) and 14.7N(0.5) | Fracture and delamination | [126] |
| $Ti_3SiC_2$ | $Ti_3SiC_2$ and diamond (Ø 5.5 mm) | 0.98 to 9.8 N | 0.013 m/s | 1.16-1.43 and 0.05 to 0.1 | Adhesive wear | [127] |
| $Ti_3SiC_2$ | Steel (AISI 52100) and $Si_3N_4$, ball (Ø4.5 to 12mm) | 0.5 to 6 N | 0.00135 m/s | Type I: (Steel: 0.15; Si3N4: 0.11) Type II: (Steel: 0.25-0.4; Si3N4: 0.35-0.45) | Third body abrasion, adhesion mechanism | [128] |
| $Ti_3SiC_2$ | Bearing steel (Ø 8.02mm) | 1-10 N | - | 1N (0.55), 2N(0.56), 4N(0.59), 6N(0.62), 8N(0.5), 10N(0.5) | Fretting wear | [129] |
| $Ti_3SiC_2$ | Bearing steel (Ø 8mm) | 1-10 N | - | 1N(0.55), 6N(0.62) and 8N(0.50) | Abrasion, tribochemical layer formation and plastic deformation | [130] |
| $Ti_3SiC_2$ | Low carbon steel (Ø300x10mm) | 0.1-0.8 MPa | 5-60 m/s | 0.53-0.09 | - | [131] |
| $Ti_3SiC_2$ | Low carbon steel (Ø300x10mm) | 0.1-0.8 MPa | 5-60 m/s | 0.26-3.75 | - | [132] |
| $Ti_3AlC_2$ | AISI 52100 steel, SiC, $Al_2O_3$ and $Si_3N_4$ (Ø 6.35 mm) | 10 N | 0.06 m/s | $Ti_3ALC_2$: SiC(0.4), AISI 52100 steel (0.1-0,63), $Si_3N_4$ and $Al_2O_3$:(1.22) | - | [133] |
| $Ti_3SiC_2$ | Pin of $Ti_3SiC_2$ (Ø3 mm) | 1, 5 and 10 N | 0.005 – 0.3 m/s | $Ti_3SiC_2$/ $Ti_3SiC_2$ dry conditions:0.7-0.9 In alcohol: 0.09-0.17 | - | [134] |
| $Ti_3AlC_2$ | AISI 304 (Ø3mm) | 1, 5 and 9 N | 0.001 m/s | TTS(1,5,9N:0.184, 0.219, 0.228), TSS-1 (1,5,9N: 0.245, 0.250, 0.237), TSS-2 (1,5,9N: 0.257, 0.289, 0.282) | Third body abrasion | [135] |
| $Ti_3SiC_2$ | AISI 440C steel (Ø9.525mm), diamond belt | 5 N, 11 N | 0.1 m/s, 10 m/s | FG and CG at 5, 1N (≈0.15, 0.35-0.4, ≈0.82, 0.81), SS diamond FG (0.83) and CG (0.82) | Two body abrasion wear, sliding wear | [136] |
| $Ti_3SiC_2$ | Bearing steel (Ø5mm) | 5 to 20 N | 0.2, 0.35, 0.5 and 0.6 m/s | 0.45 -0.7 | - | [137] |
| $Ti_3SiC_2$ | Low carbon steel (Ø300x10mm) | 0.2 – 0.8 MPa | 20 m/s | 0.2 MPa (0.35), 0.5 MPa (0.28) and 0.8 MPa (0.26) | - | [138] |

| | | | | | | |
|---|---|---|---|---|---|---|
| $Ti_3AlC_2$ | Ball of SiC, (Ø4mm) | 10 N | 0.06 m/s | At RT: 0.34; 200-400°C: 1.21; 600-1000°C: 0.56-0.75 | Abrasive and delamination wear, oxidation wear | [139] |
| $Ti_3SiC_2$ | Pin of $Ti_3SiC_2$ (Ø6 mm) | 5 N | 0.01 m/s | $Ti_3SiC_2$/ $Ti_3SiC_2$: RT to *300°C: 0.95*, 400 to *600°C*: 0.87-*0.66*, 700 to 800*°C*: *0.53* | Mechanical wear at RT-300°C, mechanical and oxidation wear at 400-600°C and oxidation wear above 700°C. | [140] |
| $Ta_2AlC$, $Ti_2AlC$, $Cr_2AlC$ and $Ti_3SiC_2$ | Alumina ($Al_2O_3$) (Ø55x 9.5mm) | 3 N | 1 m/s | $Ta_2AlC$ (0.92±0.01), $Ti_2AlC$ (0.62±0.01), $Cr_2AlC$ (0.44±0.09) and $Ti_3SiC_2$ (0.36±0.01) | Adhesive wear | [34] |
| $Ti_2AlC$, $Cr_2AlC$, $Ta_2AlC$, $Ti_3SiC_2$, $Ti_2AlN$, $Ti_4AlN_3$, $Cr_2GeC$, $Cr_2GaC$, $Nb_2SnC$ and $Ti_2SnC$ | Ni-based superalloys (Inconel-718 and Inconel-600) | 3 N | 1 m/s | At 25°C and Inc718 $Ti_2AlC$ (0.5 ± 0.1) $Ti_2AlN$ (0.8 ± 0.15) $Ti_4AlN_3$ (0.8 ± 0.15) $Ti_3SiC_2$ (0.6 ± 0.15) $Cr_2AlC$ (0.6 ± 0.1) $Ta_2AlC$ (0.5 ± 0.1) At 25°C and Inc600 $Cr_2GeC$ (0.5 ± 0.1) $Cr_2GaC$ (0.4 ± 0.1) $Ti_2SnC$ (0.63 ± 0.1) $Nb_2SnC$ (0.63 ± 0.1) | Third body abrasion | [36] |
| $Ti_3SiC_2$ | Ni-Cr and Ni-Cr-Ti alloys (Ø4mm) | 5N | 0.7 m/s | Ni-Cr: up to 500°C (0.74-0.85), 600°C (0.53), Ni-Cr-Ti (25, 500, 600°C: 0.74, 0.53, 0.53) | Adhesive wear | [141] |
| $Ti_3SiC_2$ and $Ti_3SiC_2$/Cu /Al /SiC | $Si_3N_4$ ball Ø6.43mm | 5 N | 0.188 m/s | $Ti_3SiC_2$:0.60-0.91; $Ti_3SiC_2$/Cu/Al/SiC: 0.46-0.80 | Abrasive wear dominates the wear mechanisms | [142] |
| $Ti_3SiC_2$/Cu composites | Ball SiC, (Ø6.43mm) | 5 N | 0.2 m/s | $Ti_3SiC_2$:0.79; $Ti_3SiC_2$/Cu: 0.54 | Adhesive wear and tribo-oxidation wear | [143] |
| $Ti_3SiC_2$/TiAl composites | Bearing steel, AISI 52100 (Ø6mm) | 2 – 8 N | 0.2 - 0.8 m/s | At 10 N (0.2m/s:0.55, 0.4m/s:0.45, 0.8m/s:0.35) | Abrasive wear and delamination | [144] |
| $Ti_3AlC_2$/Cu and $Ti_3Al(Sn)C_2$ solid solutions | Low carbon steel (Ø300x10mm) | 20-80 N | 30 m/s | 0.13-0.33 | - | [145] |
| $Ti_3AlC_2$ and $Ti_3AlC_2/Al_2$ | Steel ball AISI 52100 (Ø4.76mm) | 5, 15 and 25N | 0.056 m/s | $Ti_3AlC_2$:0.35-0.82; $Ti_3AlC_2$/ $Al_2O_3$:0.35-0.43 | Mechanical wear | [146] |

| | | | | | | |
|---|---|---|---|---|---|---|
| $O_3$ composites | | | | | | |
| $Ti_3SiC_2$ and $Al_2O_3$/ $Ti_3SiC_2$ | AISI 52100 bearing steel (Ø4mm) | 2.5, 5 and 10 N | - | TSC and TSC/20A (0.4-0.5), TSC/10A (0.3-9.4) | - | [147] |
| ($TiB_2$+TiC)/ $Ti_3SiC_2$ | Bearing steel, AISI 52100 (Ø4mm) | 10 to 30 N | 0.03 m/s | TiC/0B(10N:0.4, 20-30N:0.64) TiC/5-10B(0.64-0.68), TiC/15B(0.45), TiC/20B(10N:0.49, 20N:0.44, 30N:0.60) | Adhesive wear and abrasive wear | [148] |
| Boronized $Ti_2AlC$ | Alumina (Ø6mm) | 1 to 10 N | 0.17 m/s | u-$Ti_2AlC$(1N:>0.9), B-$Ti_2AlC$(1N:0.43), B-$Ti_2AlC$(4N:0.48), B-$Ti_2AlC$(10N:0.55) | - | [33] |
| NiAl-10wt%$Ti_3SiC_2$ | $Si_3N_4$ (Ø6mm) | 1 to 10 N | 0.3 m/s | 0.41 – 1.14 | - | [149] |
| $Ti_2AlN$/TiAl | Bearing steel (Ø4mm) | 1 to 9 N | 0.5 – 1.7 m/s | At 0.5 m/s (1N:1.0, 9N:0.6) | Micro-cutting, abrasive wear and oxidation wear | [150] |
| $Ti_3SiC_2$/Pb | Ni-based alloys Inconel 718, disk (Ø32x8mm) | 5 N | 0.1 m/s | At 25°C (0.61-0.72), At 800°C (0.22) | Abrasive wear and tribo-oxidation wear | [151] |
| $Ti_2AlC$, coatings | Stainless steel ball (Ø5mm) | 5, 10 and 15N | 0.005, 0.01 and 0.03 m/s | At RT: 0.32 to 0.38 and 800°C: 0.29 ± 0.02. | - | [152] |
| $Ti_2AlC$, coatings | Alumina $Al_2O_3$, ball (Ø3mm) | 5 N | 100rpm, 30min | At RT: 0.766; and 600°C: 0.603 | Abrasive wear and ductile wear | [35] |
| $Ti_3AlC_2$ coatings | Alloy-steel (42CrMo4) | 43, 86 and 106 N | 2Hz, 40000 cycles, 1.5° angle | **T1 (34kW):** 43N(0.24), 86N(0.64) and 106N(0.63) **T2 (33kW):** 43N(0.54), 86N(0.52) and 106N(0.51) | Fretting wear | [153] |
| TiSiC coatings | Ball SiC, (Ø6mm) | 5 N | - | In the atmosphere (0.43), deionized water (0.25) and seawater (0.27) | - | [154] |
| $Ti_3SiC_2$ | Bearing steel disc 100Cr6 (Ø160x10mm) | 0.1-0.6 MPa | 5-50 m/s | 0.15-0.71 | Mechanical friction, arc erosion and the coupling effect | [155] |
| $Ti_3AlC_2$ | Low carbon steel (Ø300x10mm) | 0.4-0.8 MPa | 20-60 m/s | 20 m/s and 0.4 to 0.8 Mpa: 0 A/cm$^2$ (0.18-0.14), 50 A/cm$^2$ (0.29-0.23), 100 A/cm$^2$ (0.35-0.29) | - | [156] |

## 2.5 Fundamentals concepts of electrical contacts

### 2.5.1 Introduction to electrical contacts

A separable joint between two conductors capable of carrying an electric current is called an electrical contact [157]. The essential purpose of electrical contact is to ensure that electrical current can flow freely through the contact interface. This is only possible if good metal-to-metal contact is formed (breaking down any insulating oxide layers at the interface). The nature of this contact conduction process is complex. However, they are driven by the same fundamental phenomena, the most important of which is contact interface degradation and resulting changes in contact resistance, load, temperature, and other characteristics of the real contact area.

### 2.5.2 Electrical contact resistance

All solid surfaces are rough at different scales (nano, micro or macro-scale). Roughness dimensions can range from atomic sizes to many micrometers. Surface roughness is composed of peaks and valleys whose shape, height fluctuations, lateral dimensions, average separation, and other geometric properties are determined by the manufacturing process details and surface finish [158]. Figure 2.13 shows how contact occurs between two engineering bodies at discrete locations created by the mechanical interaction of asperities on the two surfaces. For a wide range of contact forces, the real contact area is a small fraction of the nominal contact area for all solid materials [157,159]. The contact surfaces of electrical interfaces are often coated with oxide or other electrical insolating layers. The applied force, hardness and modulus of elasticity should consider for breaking these layers. The deformation mechanism of the contacting asperities may be elastic or a combination of plastic and elastic. The contact interface becomes electrically conductive when metal-to-metal contact points are formed. This happens when the layers of electrically insulating material break or move on the roughness of the contact surfaces. The electrical contact area in a typical bulk electrical contact is much less than the real mechanical contact area.

Figure 2.13 shows how the electrical current lines are distorted as they approach the electrical contact interface, and the lines of the current flow bundle together to pass through the individual contact points (or "a-spots"). The volume of material required for electrical conductivity is reduced when the electrical current is restricted by a-spots, which increases the electrical resistance. Constriction resistance is the name given to this increase in resistance. The interface contact resistance is determined by the total interface resistance produced by the constriction and the contaminant film resistances [160].

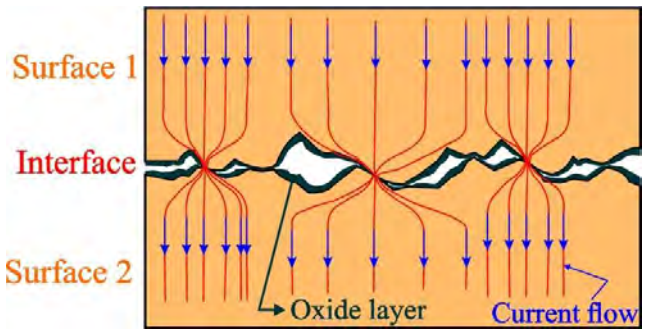


**Figure 2.13** *A bulk electrical contact is depicted in this diagram, adapted from* [157].

A-spot contacts have a wide range of variations and have been extensively investigated. The circular shapes of a-spots are the most studied of all the forms of a-spots (see Figure 2.14). The equipotential surfaces and current flow lines near an electrical constriction are seen in Figure 2.15. The equipotential surfaces at the contacts are known to consist of ellipsoids governed by the following equation 2.3:

$$\frac{r^2}{a^2+\mu^2}+\frac{z^2}{\mu^2}=1 \tag{2.3}$$

Where r and z are cylindrical coordinates and the length of the ellipsoid vertical semi-axis is u. Between the equipotential surface with semi-axis and the constriction, the resistance is given as [157]:

$$R_\mu=\frac{\rho}{2\pi}\int_0^\mu \frac{d\mu}{(a^2+\mu^2)}=\frac{\rho}{2\pi a}\tan^{-1}\left(\frac{\mu}{a}\right) \tag{2.4}$$

Where ρ is the resistivity of the electrical conductor, the μ increases considerably when it is far enough from the constriction region. The spreading resistance or constriction resistance between the equipotential surface and the contact area (constriction) can be given by the following equation 2.5:

$$R_s=\frac{\rho}{4a} \tag{2.5}$$

As a result, the total constriction resistance for both contact interfaces is equal to two times the spreading resistance:

$$R_c=\frac{\rho}{2a} \tag{2.6}$$

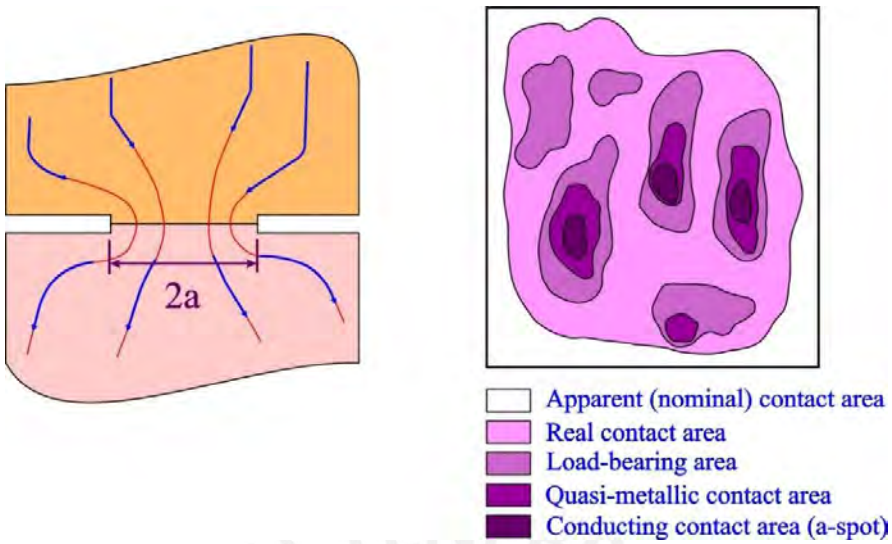


**Figure 2.14** *Schematic representation of the different contact areas, adapted from* [160].

If the electrical contact is formed by materials with different resistivities, that is, $\rho_1$ and $\rho_2$. Then, the propagation resistance associated with each half is $\rho_i/4$, where i=1,2. Thus, the contact resistance becomes:

$$R_c = \frac{(\rho_1 + \rho_2)}{2a} \tag{2.7}$$

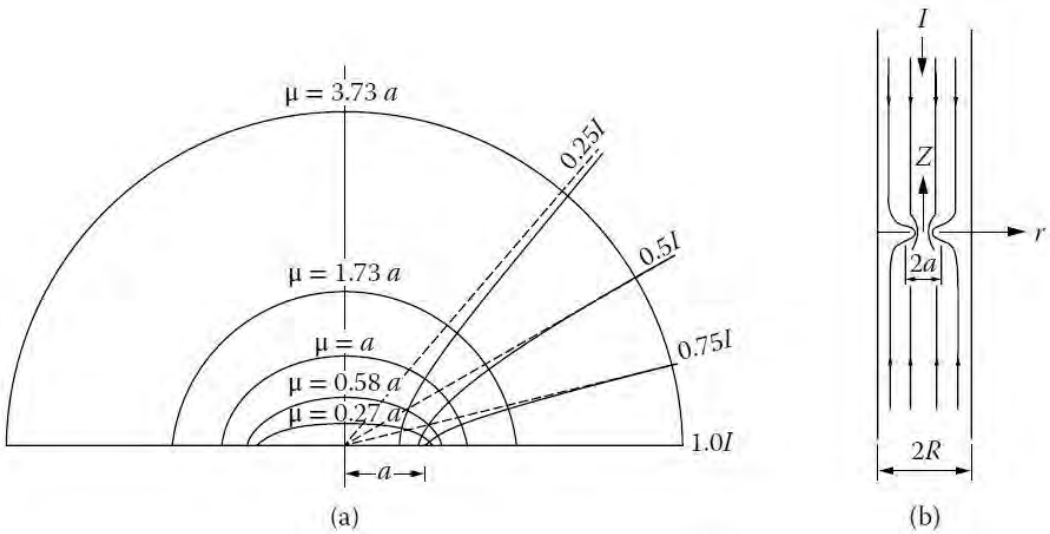


**Figure 2.15** *(a) Near the electrical constriction, equipotential surfaces and current flow lines appear. The vertical axis of the vertical ellipsoidal surface is the parameter μ. The curves corresponding to the current flow show the limits that enclose the current fraction. (b) Show a conducting cylinder of radius R with a circular constriction of radius a* [160].

### 2.5.3 Influence of the load in electrical contacts

The number of asperity contacts available for forming a-spots should increase with increasing normal load. Contact between two flat surfaces occurs in clusters of a-spots. The large-scale waviness of the contact surfaces determines the locations of the contact clusters, while the small-scale surface roughness determines the a-spots (real contact area). The number and dimensions of the a-spots and the group and size of the clusters define the contact resistance. Electrically conductive a-spots are created only when the insulating layers crack or disperse in the contact interface. The electrical contact could be mechanically connected at multiple points, but that does not guarantee that there is electrical contact. In addition, the fracture of the oxide films can be affected by the plastic or elastic deformation mode of the asperities in contact. The number of metal-to-metal a-spots is challenging to predict and may be significantly less than the number of mechanically connected asperities.

The a-spots of the contact are treated as if the spots were circular to facilitate the calculation of the contact resistance. Greenwood [161] showed for the simplest case of n a-spots within a single cluster, and the contact resistance is given by the following equation 2.8:

$$R_c = \rho\left(\frac{1}{2na} + \frac{1}{2\alpha}\right) \tag{2.8}$$

Where $a$ is the average radius of the a-spots, determined as follows $\sum a_i/n_i$ (Where $a_i$ is the radius of the i$^{th}$ spot). The cluster radius is $\alpha$, also known as Holm´s radius.

The real electrical contact area is much smaller than the apparent contact area. Therefore, the a-spots support local pressures in the range of the mechanical resistance of the materials in contact. The plastic deformation of the projecting asperities determines the real contact area. Greenwood and Williamson [159] suggest that the contact area is controlled by the mechanical properties of both materials in contact, the roughness and the surface density of the asperities. Generally, plastic deformation of the asperities occurs in most practical applications. The asperities of the softer material support the applied normal force. Equation 2.9 relates the normal force ($F$) to the mechanical contact area ($A_c$) and the hardness ($H$) of the softer contact material.

$$F = A_c H \tag{2.9}$$

Considering that there are no insulating oxides at the electrical contact interface and assuming that there are a large number of dispersed a-spots within a Holm radius $\alpha$, the contact resistance could be approximated using the following equation 2.10.

$$R_c = \frac{\rho}{2\alpha} \tag{2.10}$$

The contact area is determined using the following equation 2.11.

$$A_c = \eta\pi\alpha^2 \tag{2.11}$$

Where η is an empirical coefficient that depends on the surface conditions of the contact interface, it takes the value of 1 for clean surfaces. The contact resistance can be determined by combining Equations 2.9 and 2.11 and expressed as follow:

$$R_c = \left(\frac{\rho^2\eta\pi H}{4F}\right) \tag{2.12}$$

Figure 2.16 shows that the electrical contact resistance decreases with increasing applied mechanical force. This behavior is due to the increase in the real contact area. By increasing the contact force, the asperities are elastically and plastically deformed. In addition, due to the load, the oxide layers on the surface are broken, considerably increasing the real area of electrical contact, thus reducing the contact resistance.

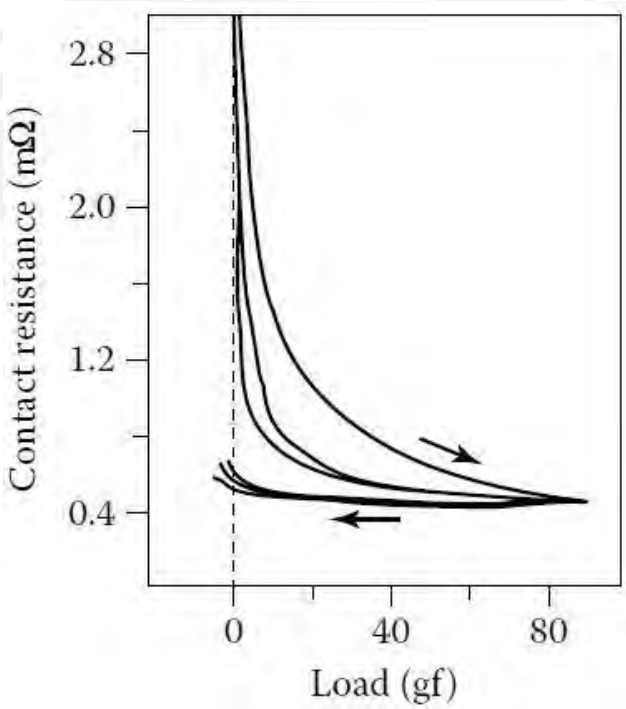


**Figure 2.16** *Contact resistance as a function of the load applied to the gold electrical contacts* [162].

### 2.5.4 The voltage-temperature relation in electrical contact interfaces

Figure 2.17 shows the temperature rise of aluminum-aluminum, copper-copper, and brass-brass electrical contacts as a function of the voltage drop across the electrical contact interface. The initial temperature $T_1$ (20°C and 100°C) has a marked effect at low voltages. Voltage drops larger than 0.1 V can cause an increase in the temperature, causing softening of the electrical contact material [160]. Equation 2.13 correlates the maximum temperature with the material parameters and the voltage drop at the contact interface.

$$T_m - T_1 = \frac{V^2}{8\lambda\rho} \tag{2.13}$$

Where $T_m$ is the maximum temperature at the interface, $T_1$ is the initial temperature at the ends of the electrical contacts of the bulk materials, V voltage drop across the electrical contact, λ is the thermal conductivity and ρ the electrical resistivity of the conductors.

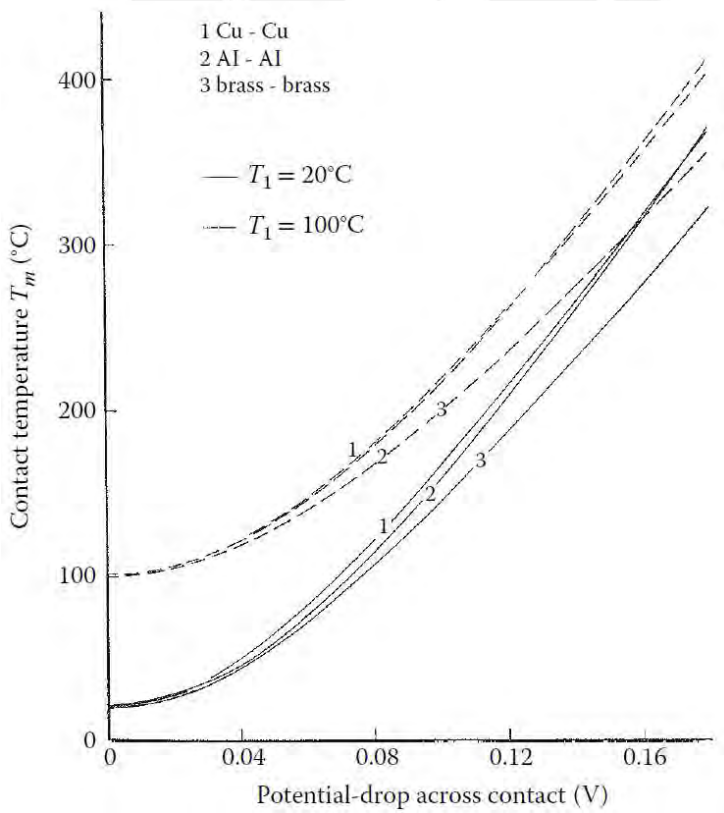


**Figure 2.17** *Voltage as a function of temperature for copper-copper, aluminum-aluminum and brass-brass electrical contacts for $T_1$ temperatures of 20°C and 100°C* [160].

# Chapter 3. Synthesis of $Ti_2AlC$ and $Ti_3AlC_2$ MAX phases thin films

## 3.1 Experimental details

The synthesis process was divided into two stages. It started with the deposition of the Ti-Al-C multilayers by magnetron sputtering and finished with rapid thermal annealing. These synthesis steps are described below in much more detail. Torres et al. [163] investigated the synthesis process and characterization of $Ti_2AlC$ and $Ti_3AlC_2$ films.

### 3.1.1 The deposition process of $Ti_2AlC$ and $Ti_3AlC_2$ MAX phases thin films

The deposition of the thin films was carried out using a CS400ES Von Ardenne sputter cluster chamber equipment. This equipment has three independent magnetrons and a sample holder located in the lower part (see Figure 3.1). The synthesis of $Ti_2AlC$ and $Ti_3AlC_2$ thin films was carried out in two stages. The first stage consists of depositing multilayers of titanium (Ti), aluminum (Al) and carbon (C) on a 4-inch Si (100) wafer. An amorphous layer of 20 nm of $SiO_2$ was thermally grown on the silicon wafer, and 80 nm of $Si_xN_y$ was obtained by plasma-enhanced chemical vapor deposition (PE-CVD) (see Figure 3.2a). These two layers between the film and the silicon wafer act as a diffusion barrier during the annealing. The stoichiometry of the thin films was controlled by the individual thicknesses of the monolayers, for which 14 nm, 6 nm and 3.5 nm of Ti, Al and C were deposited, respectively.

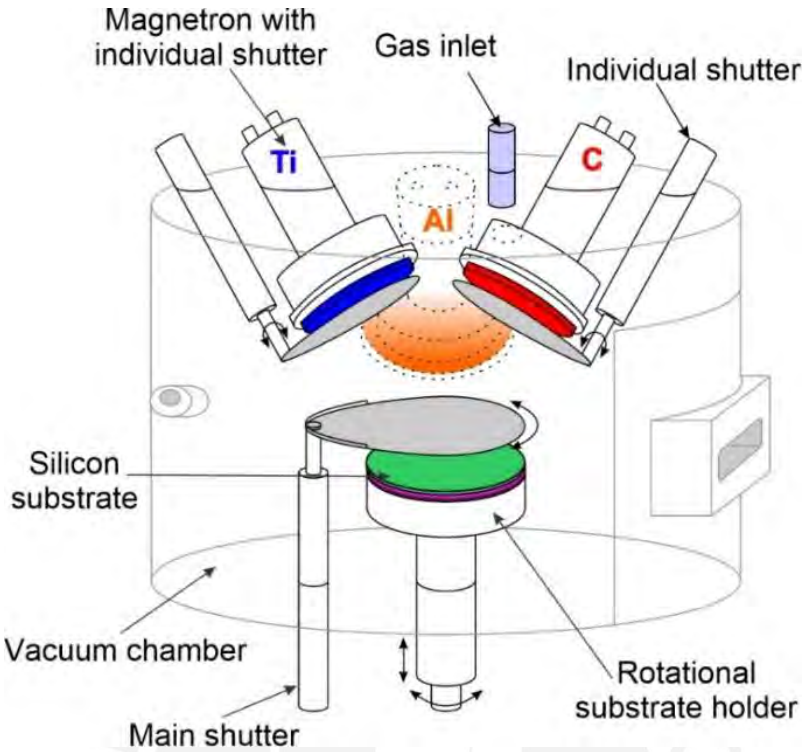


**Figure 3.1** *Schematic representation of the CS400ES Von Ardenne sputter cluster chamber equipped with three individual magnetrons and substrate holder of the Center for Micro and Nanotechnologies at TU Ilmenau, adapted from* [164].

In order to obtain an approximate thickness of 500 nm, the Ti-Al-C sequence was deposited 22 times (see Figure 3.2b). The targets were sputtered using a magnetron power of 200 W for Ti and Al and 500 W for C, respectively. The deposition of the films was carried out under a high-purity argon atmosphere with a flow rate of 30 sccm and a working pressure of $5*10^{-3}$ mbar.

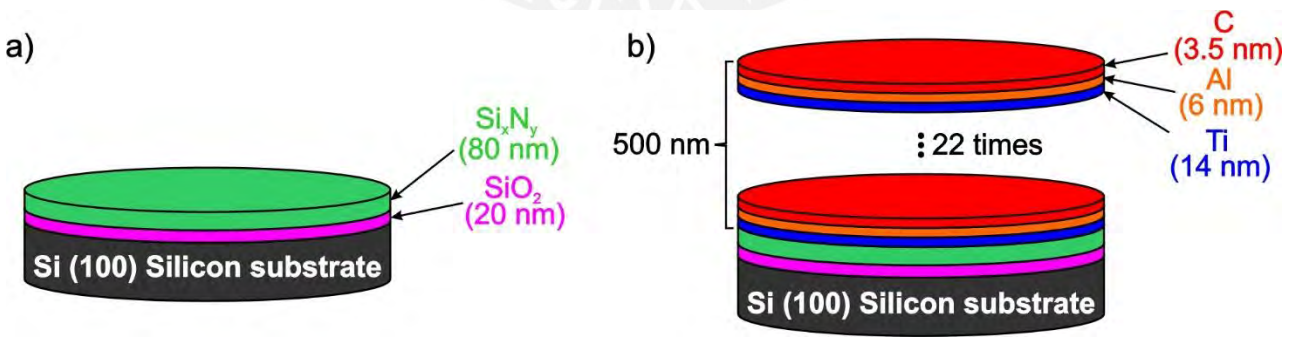


**Figure 3.2** *Schematic representation of $Ti_2AlC$ and $Ti_3AlC_2$ thin film deposition. a) diffusion barrier and substrate and b) Ti-Al-C multilayer systems.*

### 3.1.2 Annealing treatment

Rapid thermal processing (RTP) was used for annealing the components in a halogen lamp-based furnace (Jet First, Joint Industrial Processors for Electronics) with an Ar(600 sccm)/$H_2$(10 sccm) gas flow. The samples (silicon wafers with multilayers) were cut into 1x1 cm pieces (see Figure 3.3a). Inside the oven chamber, the square pieces were subjected to a vacuum. The samples were first heated at 200°C for 5 minutes to remove any remaining adsorbed water molecules (see Figure 3.3b). The samples were separated into two groups, and each group was heated at 10 K/s until a maximum temperature of 700°C and 950°C to obtain $Ti_2AlC$ and $Ti_3AlC_2$ phases, respectively. The holding time at the maximum temperature was 300 seconds. After that, the pieces were cooled down at a rate of 5 K/s until room temperature. Square samples with lateral dimensions of 1x1 $cm^2$ were used for structural and mechanical characterization, tribological and electro-tribological analyses (see Figure 3.3a).

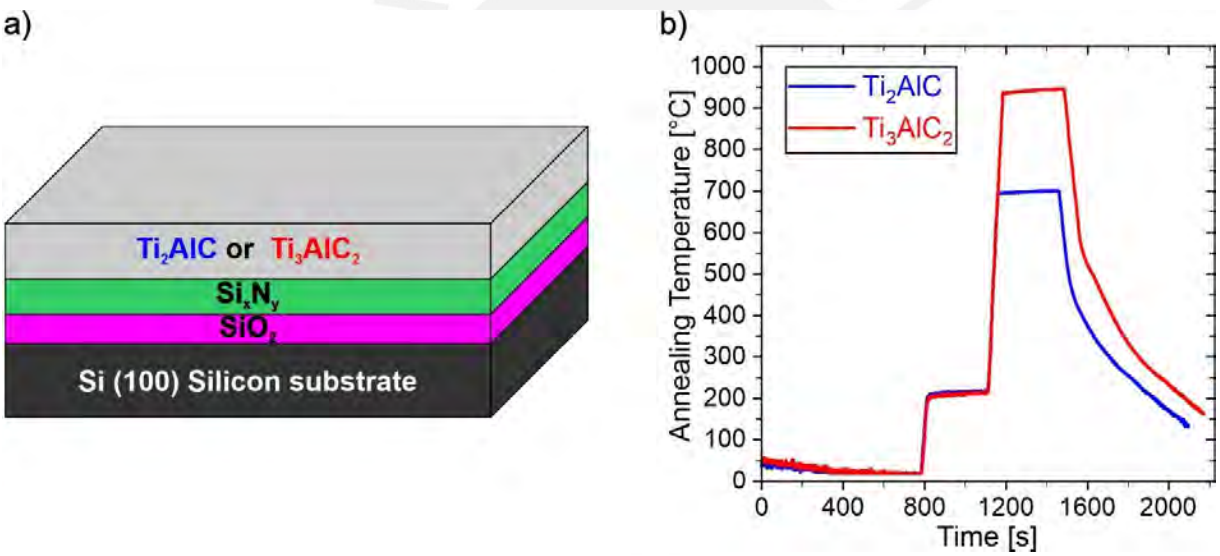


**Figure 3.3** *a) 1x1 cm square thin film samples after annealing for mechanical and tribological tests b) Thin films annealing temperature vs time.*

# Chapter 4. Characterization of the structural properties, composition and morphology of $Ti_2AlC$ and $Ti_3AlC_2$ thin films

## 4.1 Thin film characterization techniques are used to obtain structural properties and chemical composition as well as the surface roughness and morphology

The chemical composition of the thin films was performed by glow discharge optical emission spectroscopy (GD-OES, GDA 750, Spectuma Analytik GmbH Hof/Saale, Germany). This equipment includes a 2.5 mm diameter Grimm-type glow-discharge source and a Paschen-Runge type polychromator (2400 groves/mm, 750 mm diameter of Rowland's circle). This characterization was performed before and after annealing the films. Profiles of atomic concentration as a function of penetration depth were measured in DC and RF excitation modes.

The crystal structure of the thin films, density and lattice parameters were analyzed using X-ray diffraction patterns obtained by Bruker D8 Discover diffractometer with Cu $K_\alpha$ radiation (λ=1.5406 Å). Diffraction patterns were obtained in the 2θ range of 5-80° using a fixed incidence angle of incidence of 2° for the grazing incidence (GI-XRD) setup and a Goebel mirror to obtain a parallel beam. This setup was used to minimize the influence of the silicon substrate in the results. The acceleration voltage and current used were 40 kV and 40 mA, respectively. Lattice parameters and densities were calculated by using the GI-XRD patterns, Bragg's law, and the interplanar distance for the hexagonal crystal structure [165]. A Lorentzian fit [166] was applied to calculate the intensity and angular values corresponding to the diffraction peaks. The coefficient of determination ($R^2$) of the GI-XRD fits for $Ti_2AlC$ and $Ti_3AlC_2$ was 0.967 and 0.995, respectively.

The film's texture was determined by analyzing the diffraction patterns obtained by the Bragg-Brentano configuration (BB-XRD). This was done using the Bruker D8 Discover equipped with an Euler cradle (μXRD) and a Goebel mirror. This configuration with a parallel beam is known as a pseudo-BB. The type of scanning applied was coupled 2θ/θ with a 2D Vantec 500 detector. Quantitatively, the texture coefficient of the films was determined using equation 3.1 [167,168].

$$RTC_{(hkl)} = \frac{I_{hkl}/I_{hkl,p}}{\sum_1^n I_{hkl}/I_{hkl,p}} \cdot 100\% \quad (4.1)$$

Where $RTC_{(hkl)}$ represents the relative texture coefficient of a given hkl plane, $I_{hkl}$ represents the intensity corresponding to the hkl plane obtained from the thin film BB-XRD measurement, $I_{hkl,p}$ is the intensity in the hkl plane of the untextured $Ti_2AlC$ and $Ti_3AlC_2$ powder samples. This information was extracted from the powder diffraction file (PDF) database PDF 29-0095 ($Ti_2AlC$) and PDF 52-0875 ($Ti_3AlC_2$) [169]. The intensity of the peaks and the angles corresponding to the hkl planes were determined by a Lorentzian fit. The Lorentzian fit's coefficient of determination ($R^2$) was 0.956 and 0.992 for $Ti_2AlC$ and $Ti_3AlC_2$, respectively.

The structural characterization of the vibrations of the bonds between atoms was determined by Raman spectroscopy. This characterization was performed using a Renishaw inVia™ confocal micro-Raman microscope. The spectrometer was equipped with a 1200 groove/mm diffraction grating and a 100x objective lens with 0.85 numerical aperture (N.A.). The excitation wavelength of the laser used was 633 nm (He-Ne laser). The characteristic vibrational frequencies of the chemical bonds allow the identification of $Ti_2AlC$ and $Ti_3AlC_2$ phases.

The surface roughness of the $Ti_2AlC$ and $Ti_3AlC_2$ films were determined by atomic force microscopy (AFM, Dimension Icon device from Bruker). Surface scanning was performed using the PeakForce tapping mode equipped with a ScanAsyst air probe (made of silicon nitride with a spring constant of 0.4 N $m^{-1}$ and a resonance frequency of 70 kHz) in an Ar-filled glove box. Measurements were carried out at a constant scan rate of 1 Hz, and the PeakForce setpoint was set at 0.05 V.

### 4.2 The chemical composition profiles of $Ti_2AlC$ and $Ti_3AlC_2$

Figure 4.1 shows the elemental composition profiles of the films in at% as a function of the penetration depth obtained using the GD-OES technique. Figure 4.1a) shows a schematic representation of the cavity left by the GD-OES test. It can be seen that the resolution of the measurement decreases with depth. This is due to the redeposition of the sputtered material at the edges of the analyses crater and increasing inhomogeneities at the crater bottom [170]. An excellent resolution on the nanometer scale can be obtained in depths close to the surface (first few nanometers). The as-deposited film (Figure 4.1b)) shows a clear multilayer structure of individual layers with sudden changes in Ti-Al-C concentration as a function of thickness. At approximately 500 nm depth, the Ti-Al-C atomic concentration tends to zero, which verifies the total film thickness. Mainly nitrogen, oxygen and silicon are observed between 500 and 600 nm. Thus in this depth, the composition of the diffusion barrier composed of $SiO_2$ and $Si_xN_y$ was measured. At a depth greater than 600 nm, only the silicon of the wafer is shown.

The concentration profiles shown in Figure 4.1c) and d) correspond to the films annealed at 700°C ($Ti_2AlC$) and 950°C ($Ti_3AlC_2$), respectively. In both cases, along the whole film thickness, a reasonably

homogeneous concentration can be observed mainly in the middle part of the film. However, a considerable variation in concentration on the surface and at a depth of approximately 500 nm can be seen. The latter may be due to the decrease in resolution with the depth of the GD-OES technique. In the case of Figure 4.1d), an explicit diffusion of Al can be observed towards the film's top surface. In combination with the oxygen present, the formation of aluminum oxide on the film's surface could be assumed [163,171]. The decrease of Al along the film thickness due to diffusion towards the surface could be responsible for the formation of the $Ti_3AlC_2$ phase at a temperature of 950°C. Furthermore, it is observed that nitrogen tends to diffuse slightly into the film with increasing the annealing temperature.

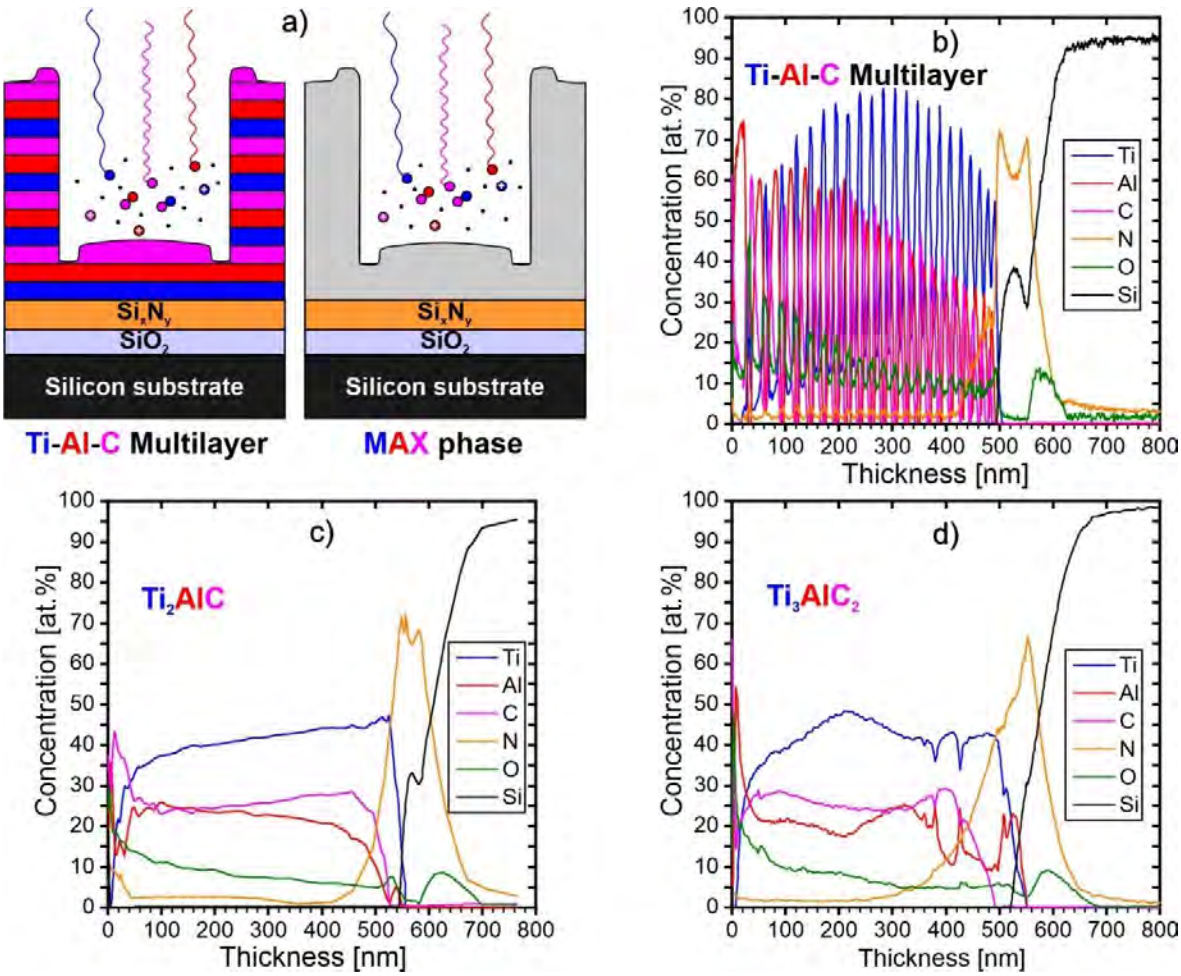


**Figure 4.1** *a) Schematic representation of GD-OES measurement of thin films. Composition profiles as a function of the thickness of (b) Ti-Al-C multilayer systems, c) $Ti_2AlC$, and d) $Ti_3AlC_2$.*

### 4.3 XRD and Raman measurements

The X-ray diffraction patterns of the thin films and their respective crystallographic planes are shown in Figure 4.2a). The crystalline nature of both thin films is verified by the characteristic diffraction patterns of the MAX phases observed in the X-ray diffraction measurement. The diffusion process induced by the annealing treatment results in the formation of two different MAX phases even though the same initial multilayer system was used. Based on the results obtained by X-ray diffraction, the samples heated to 700°C only indicates the presence of the $Ti_2AlC$ phase, while at 950 °C, the $Ti_3AlC_2$ phase is predominantly observed with smaller traces of aluminum oxide ($Al_2O_3$). The aluminum diffuses towards the surface, promoting the formation of the $Ti_3AlC_2$ phase. Additionally, recent publications report that the $Ti_3AlC_2$ phase also shows the development of low concentrations of $Al_2O_3$ near the surface [163,171].

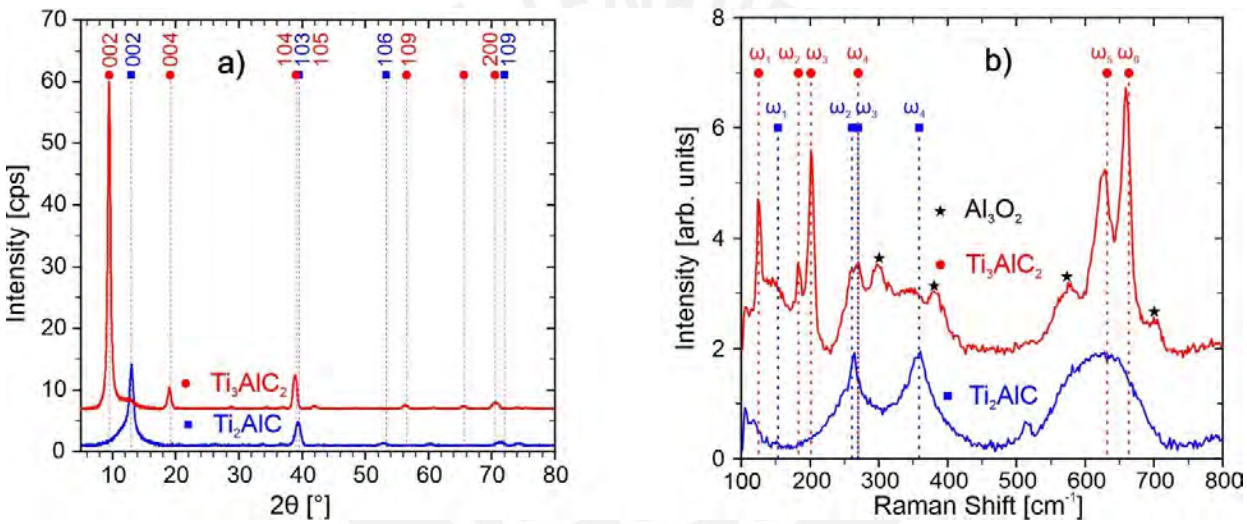


**Figure 4.2** *a) GI-XRD patterns and b) Raman spectra of $Ti_2AlC$ (blue color) and $Ti_3AlC_2$ (red color) MAX phase thin films obtained at 700°C and 950°C, respectively.*

The Raman spectra of $Ti_2AlC$ and $Ti_3AlC_2$ are shown in Figure 4.2b). The vertical lines represent the locations of the peaks reported by Presser et al. [172]. Table 4.1 shows the peaks of $Ti_2AlC$ and $Ti_3AlC_2$ obtained from the Raman spectra (experimental and calculated) and their corresponding vibrational modes. The values measured in this work are in good agreement with those found in the literature (see Table 4.1). For the $Ti_2AlC$ sample, all Raman-active modes $\omega_2$, $\omega_3$ (~264.8 $cm^{-1}$) and $\omega_4$ (360.3 $cm^{-1}$) are associated with the Ti-Al vibrations, whereas no displacement involves C atoms [173,174]. In the current study, as Feng et al. [175] reported, the peak $\omega_1$ (usually at ~150 $cm^{-1}$) associated with $Ti_2AlC$ cannot be distinguished from the background. Moreover, the peak corresponding to $\omega_3$ is not clearly distinguishable from $\omega_2$. Wang et al. [176] reported the same experimental values for $\omega_2$ and $\omega_3$ (266.0 $cm^{-1}$). Leaffer et al. [177] suggested this could happen in MAX phases. The reason for this is still unclear but might be related to how the crystals are aligned concerning the Raman laser source [178]. The $Ti_3AlC_2$ sample

shows six Raman-active modes. The peaks $\omega_1$ (124.5 $cm^{-1}$), $\omega_2$ (182.6 $cm^{-1}$), $\omega_3$ (201.2 $cm^{-1}$), $\omega_4$ (270.9 $cm^{-1}$), $\omega_5$ (628.0 $cm^{-1}$) and $\omega_6$ (659.1 $cm^{-1}$) can be associated to Ti-C vibrations while the peaks related to the Ti-Al vibrations correspond to the peaks $\omega_1$, $\omega_3$, and $\omega_5$ mentioned above [173]. The additional peaks that appear at ~297 $cm^{-1}$, ~380 $cm^{-1}$, ~575 $cm^{-1}$ and ~705 $cm^{-1}$ can be attributed to the presence of $Al_2O_3$ at the surface [179,180]. The XRD findings and Raman results confirm the formation of $Ti_2AlC$ and $Ti_3AlC_2$ MAX phases thin films.

**Table 4.1** *Raman-active vibrational modes for $Ti_2AlC$ and $Ti_3AlC_2$ based on* [172].

| ***MAX phase*** | ***Wavenumbers (ω, in $cm^{-1}$) and their corresponding Raman vibrational modes*** | | | | | | |
|---|---|---|---|---|---|---|---|
| *$Ti_2AlC$* | $\omega_1$, $E_{2g}$ | $\omega_2$, $E_{2g}$ | $\omega_3$, $E_{1g}$ | $\omega_4$, $A_{1g}$ | Comments, reference | | |
| | - | 264.8 | 264.8 | 360.3 | This work | | |
| | - | 269.0 | 269.0 | 359.0 | Exp., [175] | | |
| | 153.3 | 260.9 | 270.3 | 358.7 | Exp., [172] | | |
| | - | 266.0 | 266.0 | 359.0 | Exp., [176] | | |
| | 149.9 | 262.1 | 268.1 | 365.1 | Exp., [174] | | |
| | 146.0 | 265.0 | 266.0 | 365.0 | Cal., [172] | | |
| | 151.0 | 256.0 | 270.0 | 366.0 | Cal., [177] | | |
| *$Ti_3AlC_2$* | $\omega_1$, $E_{2g}$ | $\omega_2$, $E_{1g}$ | $\omega_3$, $E_{2g}$ | $\omega_4$, $A_{1g}$ | $\omega_5$, $E_{1g}$ and $E_{2g}$ | $\omega_6$, $A_{1g}$ | Comments, reference |
| | 124.5 | 182.6 | 201.2 | 270.9 | 628.0 | 659.1 | This work |
| | - | 183.4 | 201.5 | 270.2 | 632.2 | 663.2 | Exp., [172] |
| | 125.0 | 182.0 | 197.0 | 268.0 | 620.0 and 621.0 | 655.0 | Cal., [172] |

### 4.3.1 Lattice parameters and density of $Ti_2AlC$ and $Ti_3AlC_2$

Figure 4.3a) and b) show the crystalline unit cell of the $Ti_2AlC$ and $Ti_3AlC_2$ phases, respectively. The variables **c** and **a** observed in both figures are the lattice parameters which define the unit cell. The distance between two parallel planes is known as the interplanar distance ($d_{hkl}$). The interplanar distance is given by half of the lattice parameter **c**. Bragg's law determines this distance (see Equation 4.2). The layered crystalline structure of the MAX phases is anisotropic; therefore, their properties depend on the preferred orientations.

$$d_{hkl} = \frac{n\lambda}{2\,sin\,\theta} \tag{4.2}$$

Where n is an integer usually equal to 1, λ is the wavelength of the X-rays, and θ is the angular position corresponding to the crystallographic planes.

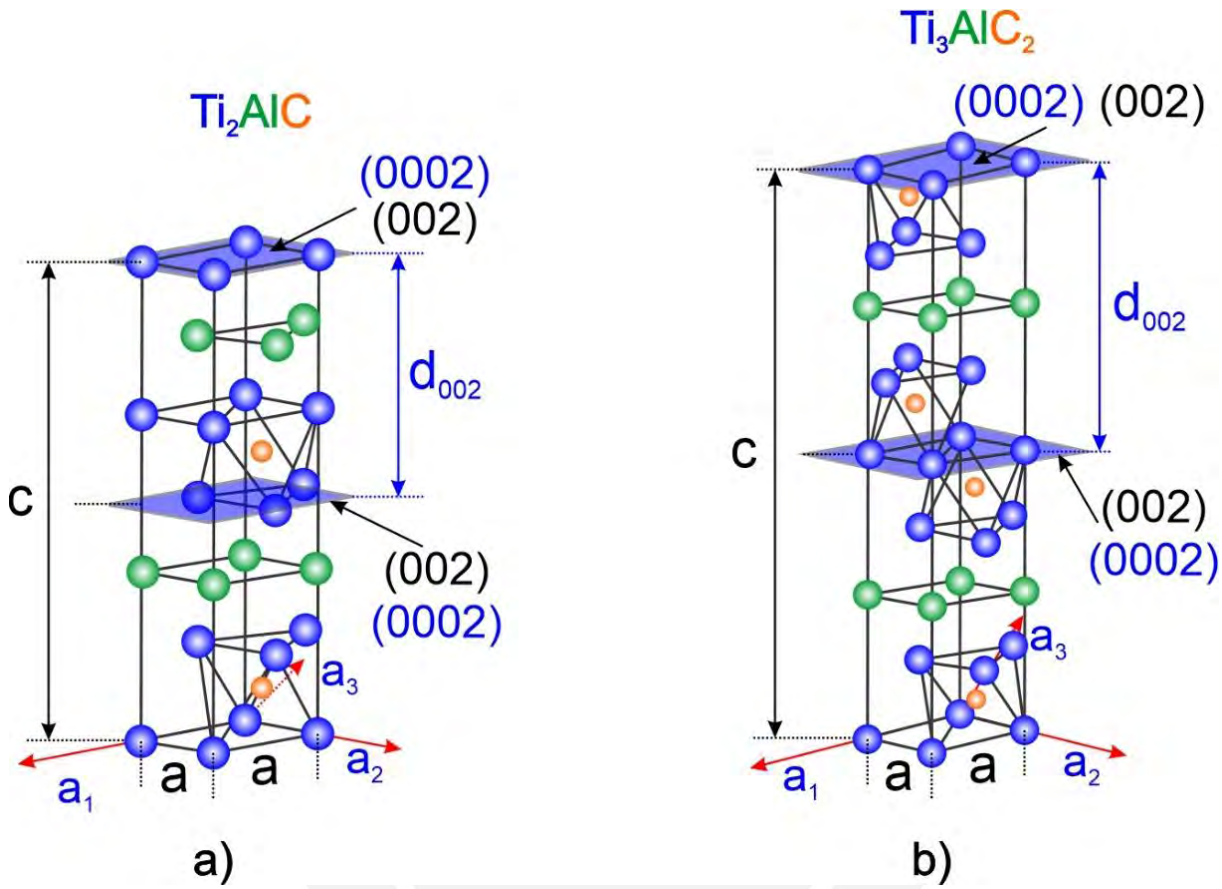


**Figure 4.3** *Crystal structure and lattice parameters of the MAX phases. a) $Ti_2AlC$ and b) $Ti_3AlC_2$.*

Figure 4.4a) shows the Miller indices of the $Ti_2AlC$ phase with their respective crystallographic planes. This data was obtained from the PDF 29-0095 database. Miller indices can be represented indistinctly by two types of notations (hkl) and (hkil), where i is a function of the two other components h and k: i = -(h+k). Using these Miller indices offers the possibility of locating the positions of the atoms in the unit cell. In Figure 4.4a) all the possible crystallographic planes are shown since this data corresponds to an XRD measurement of powder material. Powders commonly are non-textured materials or without preferred orientation. At the same time, the planes highlighted in blue correspond to the $Ti_2AlC$ thin film prepared in this work. As the film has a preferred orientation, certain crystallographic planes are not present in the XRD diffractogram. Figure 4.4b) shows the spatial orientation of the planes corresponding to the $Ti_2AlC$ thin film.

a)

| 2θ (°) | Miller Index (hkl) | | | (hkil) | | | |
|---|---|---|---|---|---|---|---|
| | h | k | l | h | k | i | l |
| 13.0 | 0 | 0 | 2 | 0 | 0 | 0 | 2 |
| 34.0 | 1 | 0 | 0 | 1 | 0 | -1 | 0 |
| 34.7 | 1 | 0 | 1 | 1 | 0 | -1 | 1 |
| 39.5 | 1 | 0 | 3 | 1 | 0 | -1 | 3 |
| 39.7 | 0 | 0 | 6 | 0 | 0 | 0 | 6 |
| 43.4 | 1 | 0 | 4 | 1 | 0 | -1 | 4 |
| 53.3 | 1 | 0 | 6 | 1 | 0 | -1 | 6 |
| 60.9 | 1 | 1 | 0 | 1 | 1 | -2 | 0 |
| 71.6 | 2 | 0 | 0 | 2 | 0 | -2 | 0 |
| 72.0 | 1 | 0 | 9 | 1 | 0 | -1 | 9 |
| 75.2 | 1 | 1 | 6 | 1 | 1 | -2 | 6 |
| 85.2 | 2 | 0 | 6 | 2 | 0 | -2 | 6 |
| 101.8 | 2 | 0 | 9 | 2 | 0 | -2 | 9 |
| 104.9 | 2 | 1 | 3 | 2 | 1 | -3 | 3 |
| 115.9 | 1 | 1 | 12 | 1 | 1 | -2 | 12 |
| 135.9 | 2 | 1 | 9 | 2 | 1 | -3 | 9 |

b)

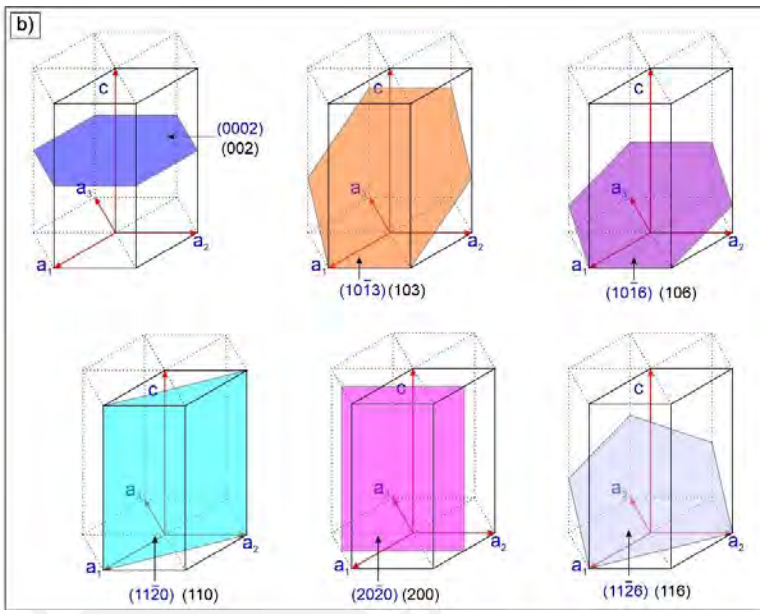


**Figure 4.4** *a) Miller index obtained from data base PDF 29-0095 and b) crystallographic planes of $Ti_2AlC$.*

Figure 4.5a) shows the Miller indices of the $Ti_3AlC_2$ phase with their respective crystallographic planes. This data was obtained from the PDF 52-0875 database. Figure 4.5b) shows the spatial orientation of the planes corresponding to the $Ti_3AlC_2$ thin film. It can be seen that the $Ti_3AlC_2$ phase, unlike the $Ti_2AlC$ phase, shows two basal planes (002) and (004). These two planes are the most intense in X-ray diffraction. The relative texture coefficient results indicate that this phase has a preferred basal orientation.

a)

| 2θ (°) | Miller Index (hkl) | | | (hkil) | | | |
|---|---|---|---|---|---|---|---|
| | h | k | l | h | k | i | l |
| 9.5 | 0 | 0 | 2 | 0 | 0 | 0 | 2 |
| 19.2 | 0 | 0 | 4 | 0 | 0 | 0 | 4 |
| 33.7 | 1 | 0 | 0 | 1 | 0 | -1 | 0 |
| 34.0 | 1 | 0 | 1 | 1 | 0 | -1 | 1 |
| 35.1 | 1 | 0 | 2 | 1 | 0 | -1 | 2 |
| 36.8 | 1 | 0 | 3 | 1 | 0 | -1 | 3 |
| 38.8 | 0 | 0 | 8 | 0 | 0 | 0 | 8 |
| 39.0 | 1 | 0 | 4 | 1 | 0 | -1 | 4 |
| 41.8 | 1 | 0 | 5 | 1 | 0 | -1 | 5 |
| 44.9 | 1 | 0 | 6 | 1 | 0 | -1 | 6 |
| 48.5 | 1 | 0 | 7 | 1 | 0 | -1 | 7 |
| 52.4 | 1 | 0 | 8 | 1 | 0 | -1 | 8 |
| 56.6 | 1 | 0 | 9 | 1 | 0 | -1 | 9 |
| 60.3 | 1 | 1 | 0 | 1 | 1 | -2 | 0 |
| 61.0 | 1 | 1 | 2 | 1 | 1 | -2 | 2 |
| 65.7 | 1 | 0 | 11 | 1 | 0 | -1 | 11 |
| 70.6 | 2 | 0 | 0 | 2 | 0 | -2 | 0 |
| 70.6 | 1 | 0 | 12 | 1 | 0 | -1 | 12 |

b)

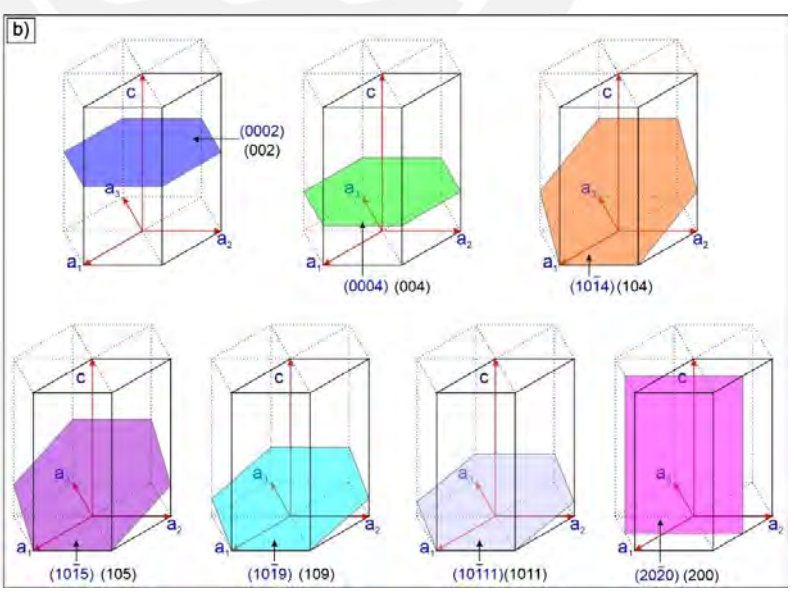


**Figure 4.5** *a) Miller index obtained from data base PDF 52-0875 and b) crystallographic planes of $Ti_3AlC_2$.*

The lattice parameters a and c can be determined using equation 4.3. In order to use this equation, the Miller indices of the crystallographic planes must be known. Since equation 4.3 has two variables a and c, the solution of this equation is restricted to first using the basal planes in order to determine one of the lattice parameters. The other lattice parameter can be determined using the previously determined lattice parameter. Where $d_{hkl}$ is the interplanar distance corresponding to each crystallographic plane, h, k and l are the Miller indices, a and c the lattice parameters that define the unit cell.

$$\frac{1}{d_{hkl}^2} = \frac{4}{3}\left(\frac{h^2 + hk + k^2}{a^2}\right) + \frac{l^2}{c^2} \tag{4.3}$$

If the lattice parameters a and c were determined, it would be possible to find the volume of the unit cell using equation 4.4. It is worth mentioning that the hexagonal structure is composed of three rhomboid prisms. To determine the density of the $Ti_2AlC$ and $Ti_3AlC_2$ films, the volume of the unit cell must be determined as well as the total atomic weight of the atoms contained in the unit cell. Equation 4.5 connects the density with the number of atoms present in the unit cell. Where $n_i$ is the number of atoms of Ti, Al, and C. $A_{wi}$ represents the atomic weights of Ti, Al, and C. V is the unit cell volume, and $N_A$ is Avogadro's number ($6.0222 \cdot 10^{23}$ at/mol).

$$V = \frac{\sqrt{3}a^2 c}{2} \tag{4.4}$$

$$\rho = \frac{\sum_{i=1}^{3} n_i A_{wi}}{V N_A} \tag{4.5}$$

Table 4.2 shows a summary of the data used to calculate the lattice parameters and the density corresponding to the $Ti_2AlC$ phase.

**Table 4.2** *Values used for calculating the lattice parameters and the density of the $Ti_2ALC$ phase.*

| Variables | Values | Units |
|---|---|---|
| λ | 0.15406 | nm |
| n | 1 | - |
| $n_{Al}$ | 2 | N° Atoms of Al |
| $A_{wAl}$ | 26.982 | The atomic weight of Al (g/mol) |
| $n_C$ | 2 | N° Atoms of C |
| $A_{wC}$ | 12.011 | The atomic weight of C (g/mol) |
| $n_{Ti}$ | 4 | N° Atoms of Ti |
| $A_{wTi}$ | 47.876 | The atomic weight of Ti (g/mol) |
| V | $1.089 \cdot 10^{22}$ | Unit cell volume ($cm^3$) |

Table 4.3 shows the values used, and the results of the calculations performed to determine the lattice parameters and the density of the $Ti_2AlC$ phase.

**Table 4.3** *Process for obtaining the lattice parameters and the density of $Ti_2AlC$ thin film.*

| **$Ti_2AlC$ MAX phase** | | | | | | | | | | | | | |
|---|---|---|---|---|---|---|---|---|---|---|---|---|---|
| **Miller Index PDF 29-0095** | | | | | **$Ti_2AlC$ - Fit** | | **Lattice parameters a and c** | | | | **Density** | | |
| Miller Index | | | 2θ | Intensity | 2θ | Intensity | θ | $d_{hkl\text{-}Spacing}$ | a | c | Volume | | ρ |
| h | k | l | (°) | $I_{(hkl),p}$ | (°) | $I_{(hkl)}$ | (°) | nm | nm | nm | $nm^3$ | $cm^3$ | $g/cm^3$ |
| 0 | 0 | 2 | 13.01 | 14281 | 12.97 | 11.98 | 6.48 | 0.682 | | 1.364 | 0.110 | 1.1E-22 | 4.05 |
| 1 | 0 | 3 | 39.55 | 36619 | 39.35 | 3.89 | 19.67 | 0.229 | 0.306 | | | | |
| 1 | 0 | 6 | 53.29 | 5127 | 52.85 | 0.34 | 26.43 | 0.173 | | 1.372 | 0.112 | 1.1E-22 | 3.99 |
| 1 | 1 | 0 | 60.90 | 5127 | 60.23 | 0.20 | 30.11 | 0.154 | 0.307 | | | | |
| 2 | 0 | 0 | 71.63 | 732 | 71.31 | 0.57 | 35.65 | 0.132 | 0.305 | | | | |
| 1 | 1 | 6 | 75.21 | 4028 | 74.31 | 0.28 | 37.15 | 0.128 | | | | | |
| | | | | | | | Lattice parameters (nm) | | 0.306 | 1.368 | **Density ($g/cm^3$)** | | **4.02** |
| | | | | | | | Standard deviation | | 0.001 | 0.004 | Standard deviation | | 0.03 |

Table 4.4 summarises the data used for calculating the lattice parameters and the density corresponding to the $Ti_3AlC$ phase.

**Table 4.4** *Values used for calculating the lattice parameters and the density of the $Ti_3ALC_2$ phase.*

| Variables | Values | Units |
|---|---|---|
| λ | 0.15406 | nm |
| n | 1 | - |
| $n_{Al}$ | 2 | N° Atoms of Al |
| $A_{wAl}$ | 26.982 | The atomic weight of Al (g/mol) |
| $n_C$ | 4 | N° Atoms of C |
| $A_{wC}$ | 12.011 | The atomic weight of C (g/mol) |
| $n_{Ti}$ | 6 | N° Atoms of Ti |
| $A_{wTi}$ | 47.876 | The atomic weight of Ti (g/mol) |
| V | $1.530 \cdot 10^{22}$ | Unit cell volume ($cm^3$) |

Table 4.5 shows the calculations performed to determine the lattice parameters and the density of the $Ti_3AlC_2$ phase. It should be mentioned that the $Ti_3AlC_2$ phase has a higher volume than the $Ti_2AlC$ phase. Furthermore, the $Ti_3AlC_2$ phase contains more atoms within its unit cell and is somewhat denser.

**Table 4.5** *Process for obtaining the lattice parameters and the density of $Ti_3AlC_2$ thin film.*

| **$Ti_3AlC_2$ MAX phase** | | | | | | | | | | | | | |
|---|---|---|---|---|---|---|---|---|---|---|---|---|---|
| **Miller Index PDF 52-0875** | | | | | **$Ti_3AlC_2$ - Fit** | | **Lattice parameters a and c** | | | | **Density** | | |
| Miller Index | | | 2θ | Intensity | 2θ | Intensity | θ | $d_{hkl\text{-}Spacing}$ | a | c | Volume | | ρ |
| h | k | l | (°) | $I_{(hkl),p}$ | (°) | $I_{(hkl)}$ | (°) | nm | nm | nm | $nm^3$ | $cm^3$ | $g/cm^3$ |
| 0 | 0 | 2 | 9.52 | 9887 | 9.48 | 54.211 | 4.74 | 0.932 | | 1.864 | 0.153 | 1.53E-22 | 4.22 |
| 0 | 0 | 4 | 19.15 | 1831 | 19.01 | 3.362 | 9.50 | 0.467 | | 1.866 | 0.150 | 1.5E-22 | 4.32 |
| 1 | 0 | 4 | 39.04 | 36619 | 38.88 | 5.845 | 19.44 | 0.231 | 0.308 | | | | |
| 1 | 0 | 5 | 41.82 | 10253 | 41.96 | 0.357 | 20.98 | 0.215 | 0.304 | | | | |
| 1 | 0 | 9 | 56.57 | 4394 | 56.36 | 0.577 | 28.18 | 0.163 | | 1.856 | 0.152 | 1.52E-22 | 4.25 |
| 1 | 0 | 11 | 65.67 | 1831 | 65.57 | 0.348 | 32.79 | 0.142 | | 1.850 | | | |
| 2 | 0 | 0 | 70.57 | 4028 | 70.62 | 1.081 | 35.31 | 0.133 | 0.308 | | | | |
| | | | | | | | Lattice parameters (nm) | | 0.307 | 1.859 | **Density ($g/cm^3$)** | | **4.26** |
| | | | | | | | Standard deviation | | 0.002 | 0.006 | Standard deviation | | 0.04 |

So far, literature states that thin films are less dense than the same bulk materials as the thin-film density depends on deposition conditions [181,182]. In Table 4.6, the lattice parameters obtained by XRD are shown. This allows an estimation of the thin film densities, which can be correlated to the mechanical properties. It can be seen that the lattice parameters and density values of $Ti_2AlC$ and $Ti_3AlC_2$ thin films are similar to those reported in the literature for the same bulk MAX phases. The density of $Ti_2AlC$ ($4.02 \pm 0.03$ $g/cm^3$) is slightly less than the theoretical value (4.11 $g/cm^3$). The accuracy of density measurements depends on the characterization technique. In this sense, Cullity [165] suggests that the bulk density determined from weight and volume or Archimedes' method is generally lower than values obtained from XRD. This is ascribed to defects such as minor cracks and porosities. In contrast, the density of $Ti_3AlC_2$ ($4.26 \pm 0.04$ $g/cm^3$) is slightly higher than DFT values (4.22 and 4.21 $g/cm^3$) from Table 4.6. Tzenov and Barsoum [183] reported the density of $Ti_3AlC_2$ (4.20 $g/cm^3$) with ~4 vol% of impurities or secondary phases (mostly $Al_2O_3$). The defects in the crystal structure, impurities, and internal stress could be reasons for the variation of these reported values based on XRD measurements.

**Table 4.6** *Lattice parameters and density of bulk MAX phases from literature and thin films of this work.*

| *MAX phase* | *Lattice parameters [Å]* | | *Density [g/cm³]* | *Density obtained method* | *Reference* |
|---|---|---|---|---|---|
| | **a** | **C** | | | |
| ***Ti₂AlC*** | 3.060 ± 0.001 | 13.684 ± 0.004 | 4.02 ± 0.03 | XRD measurements | This work |
| | 3.040 | 13.600 | 4.11 | Theoretical calculation | [78] |
| | 3.051[a] | 13.637[a] | 4.10[b] | Archimedes' method | [53,184] |
| | 3.067 | 13.750 | 3.99 | DFT simulations | [185] |
| | 3.050 | 13.647 | 3.97 | Archimedes' method | [49] |
| ***Ti₃AlC₂*** | 3.066 ± 0.002 | 18.592 ± 0.006 | 4.26 ± 0.04 | XRD measurements | This work |
| | 3.075 | 18.578 | 4.25[c] | XRD measurements | [186] |
| | 3.079 | 18.589 | 4.23 | XRD measurements | [85] |
| | 3.072 | 18.732 | 4.22[d] | DFT simulations | [187] |
| | 3.083 | 18.660 | 4.21 | DFT simulations | [185] |
| | 3.065 | 18.487 | 4.20 | - | [183] |
| | - | - | 4.21 | Archimedes' method | [188] |

[a]from Ref. [184], [b]from Ref. [53], [c] and [d] calculated using lattice parameters from Ref. [186] and Ref. [187], respectively.

### 4.3.2 Texture analysis of $Ti_2AlC$ and $Ti_3AlC_2$

The thin films were analyzed by two-dimensional X-ray diffraction (2D-XRD). Figure 4.6a) and b) show the X-ray diffraction patterns with their respective crystallographic planes identified by their Miller indices. The diffraction patterns of both films were obtained by integrating both 2D macros in the gamma direction (see Figure 4.7). 2D-XRD gives valuable information such as grain size, internal stress and texture.

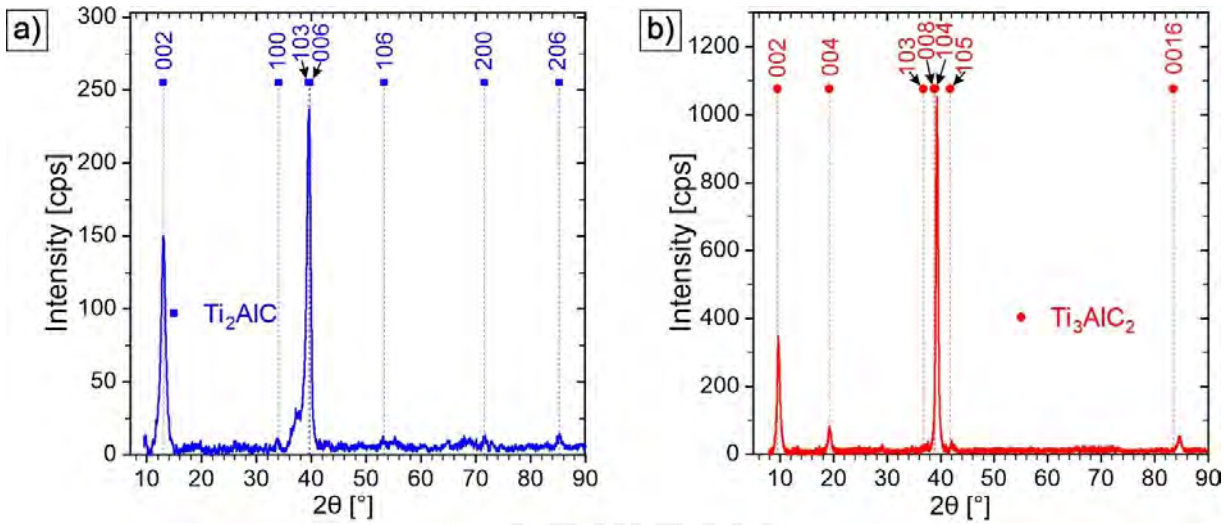


**Figure 4.6** *BB-XRD diffraction patterns of a) $Ti_2AlC$ and b) $Ti_3AlC_2$, respectively.*

In Figure 4.7, the preferred crystallographic orientation of thin films can be seen qualitatively as the intensity variation along the gamma direction of diffraction rings. The $Ti_2AlC$ thin film shows as preferred orientation four planes (002), (103), (006), (200) and (206). In the same way, the preferred orientations for $Ti_3AlC_2$ are mainly the following basal planes (002), (004), (008) and (0016). For both frames, the dark ellipse on the left side is the total reflection of the primary beam on the surface, and the dark spot on the right side is the silicon substrate peak.

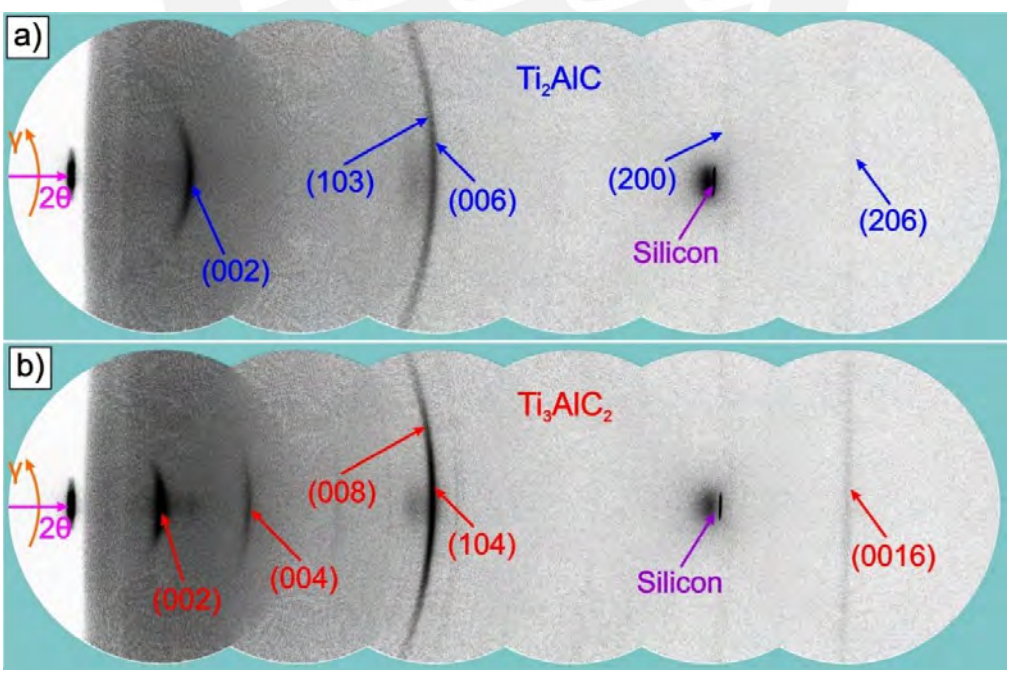


**Figure 4.7** *Two-dimensional (2D) XRD 2θ-θ frames of a) $Ti_2AlC$ and b) $Ti_3AlC_2$, respectively.*

Figure 4.8 shows the RTC values corresponding to the different crystallographic planes of $Ti_2AlC$ and $Ti_3AlC_2$ thin films. Both samples possess a hexagonal crystal structure and are textured. The qualitative information of the texture shown in Figure 4.7 agrees with the results calculated and shown in Figure 4.8. A polycrystalline material would show an equal distribution of the possible orientations in the crystal, leading to an RTC of 14.29% for the seven orientations shown. Thus, all values of the RTC higher than 14.29% could be considered as preferred crystallographic orientation or texture.

Figure 4.8a) shows the basal (002), prismatic (200) and pyramidal ((103) and (206)) planes as preferred orientations for $Ti_2AlC$ thin film. On the other hand, $Ti_3AlC_2$ shows preferred orientation mainly in the basal planes (002), (004), (008), and (0016) as can be seen in Figure 4.8b). The texture of $Ti_2AlC$ has a mix of basal, prismatic and pyramidal planes, while the $Ti_3AlC_2$ shows only basal planes parallel to the surface of the thin films. Therefore, it can be expected that this texture of the $Ti_3AlC_2$ MAX phase thin film will predominantly influence its mechanical properties. On the other hand, for the $Ti_2AlC$ phase thin film, the mix of preferable orientations lead to less anisotropy. Thus, the properties are less susceptible than the highly textured films.

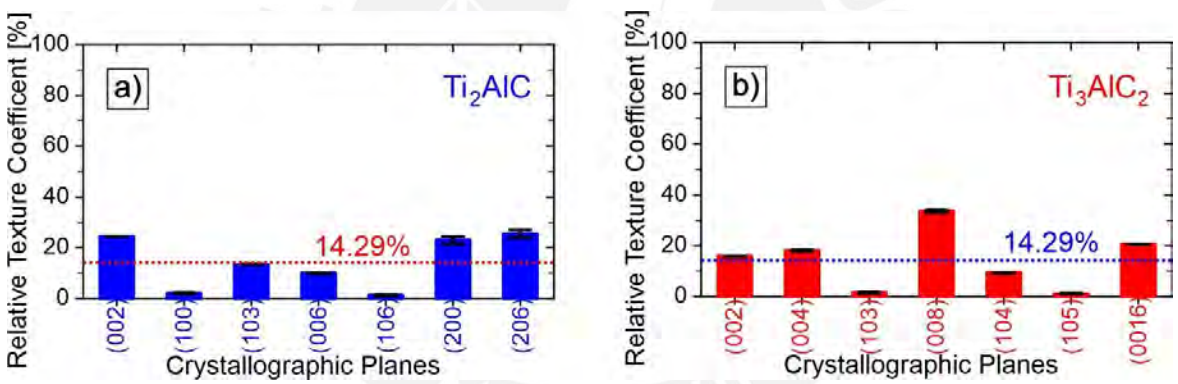


**Figure 4.8** *The intensity changes in the gamma direction suggest that both films have preferential orientations. The relative texture coefficients for a) $Ti_2AlC$ and b) $Ti_3AlC_2$, respectively.*

The layered crystalline structure makes the MAX phases slightly anisotropic concerning properties such as mechanical, electrical, magnetic, etc. [189]. The RTC values give a good first approximation of the behavior of the MAX phases when they are subjected to friction and wear. It is known that macroscopic properties such as resistance, hardness, ductility, and friction depend on elastic constants. The constants $c_{11}$ and $c_{33}$ describe the deformation stiffness parallel to the a and c axes, respectively [190,191]. The elastic constants for these materials are $c_{11}$ = 338 GPa and $c_{33}$ = 348 GPa for $Ti_2AlC$ and $c_{11}$ = 277 GPa and $c_{33}$ = 242 GPa for $Ti_3AlC_2$, respectively [192,193].

## 4.4 Atomic force microscopy of $Ti_2AlC$ and $Ti_3AlC_2$

The surface morphology of both thin films as determined by AFM is depicted in Figure 4.9. $Ti_2AlC$ and $Ti_3AlC_2$ have an average surface roughness ($R_a$) of around 4 and 12 nm, respectively. The $Ti_2AlC$ film seems to have smaller grains, according to the AFM images, whereas the $Ti_3AlC_2$ film gives the impression of showing much coarser grains close to the surface. This observation may be explained by the fact that $Ti_3AlC_2$ was annealed at a higher temperature.

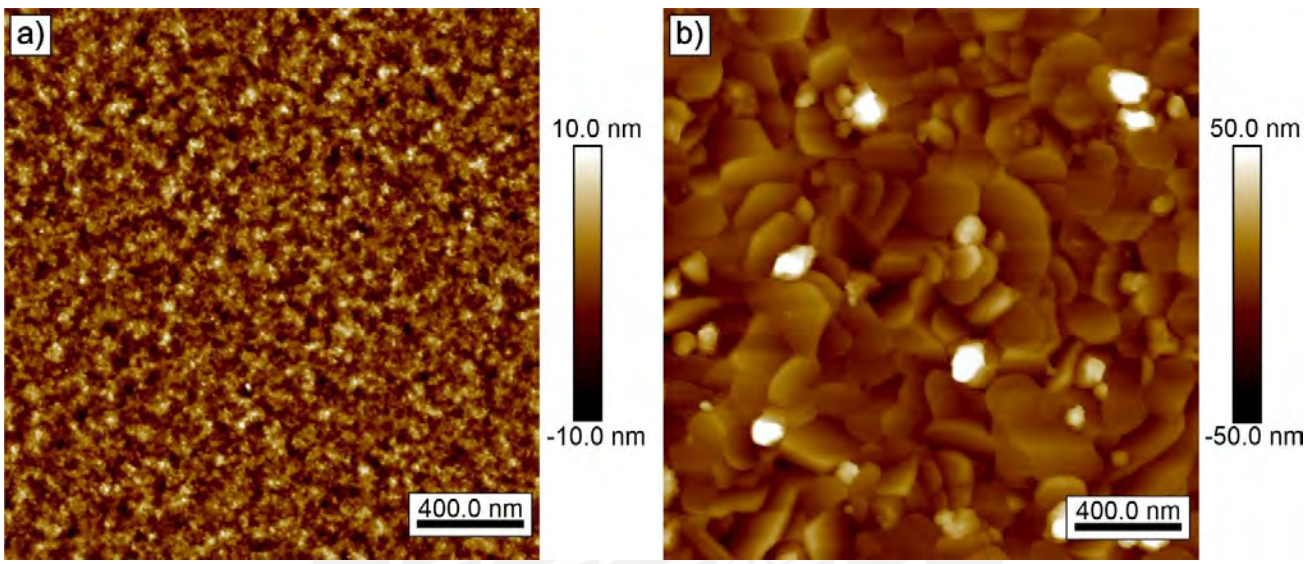


**Figure 4.9** *AFM images of the surfaces of a) $Ti_2AlC$ and b) $Ti_3AlC_2$ thin films, respectively.*

## 4.5 Conclusions

This chapter evaluated the composition and structural properties of $Ti_2AlC$ and $Ti_3AlC_2$ thin films. GD-OES, XRD and Raman spectroscopy results confirmed the formation of thin films of the pure phases $Ti_2AlC$ and $Ti_3AlC_2$ at annealing temperatures of 700 and 950°C, respectively. The density obtained from X-ray diffraction shows that the $Ti_2AlC$ phase (4.02 ± 0.03 g/cm$^3$) is less dense than the $Ti_3AlC_2$ phase (4.26 ± 0.04 g/cm$^3$). This could be attributed to the $Ti_3AlC_2$ phase containing more atoms within its unit cell. The $Ti_2AlC$ thin film has a mixed preferred orientation, while the $Ti_3AlC_2$ phase has a preferred basal orientation. AFM measurements reveal that the average surface roughness ($R_a$) of $Ti_2AlC$ and $Ti_3AlC_2$ is approximately 4 and 12 nm, respectively. These properties will be correlated with the results of the tribological and electro-tribological tests.

# Chapter 5. Mechanical and tribological performance of $Ti_2AlC$ and $Ti_3AlC_2$ thin films

## 5.1 Introduction

This chapter begins with the experimental details of hardness and tribological measurements. In this chapter, the mechanical properties are correlated to the tribological performance of the two types of thin films. Furthermore, for a better discussion, the results obtained in chapter 4 (characterization of $Ti_2AlC$ and $Ti_3AlC_2$ films) are used. In addition, the hardness of $Ti_2AlC$ (11.6 ± 0.3 GPa) and $Ti_3AlC_2$ (5.3 ± 0.9 GPa) thin films is reported and analyzed. Moreover, the friction coefficients of both films are investigated. These results are discussed based on the film's texture, grain size and surface roughness. Finally, the track left by tribological tests is studied.

## 5.2 Experimental details

### 5.2.1 Hardness measurements of $Ti_2AlC$ and $Ti_3AlC_2$

The hardness of the thin films was determined using the nanoindenter (Picodentor HM500, Helmut Fischer GmbH). This device features a diamond indenter with a typical Vickers indenter shape. Hardness was determined using the model proposed by Oliver and Pharr [194]. In addition, hardness measurements were performed following the Enhanced Stiffness Procedure (ESP) developed by Helmut Fischer GmbH. For this later, a maximum load of 10 mN was used. This normal load was divided into 20 cycles of loading and unloading. The unloading was carried out until reaching 65% of the force applied in the previous cycle. Since the film's hardness depends on the measurement's depth, the substrate's influence is almost unavoidable. This method is advantageous since it estimates the hardness at low and different penetration depths. In this way, the effect of the substrate is reduced. The reported hardness values were measured at a depth of 50 nm. This depth is equivalent to 10% of the film thickness, as suggested by DIN EN ISO 14577 - 4:2017 [195] and ASTM E2546 - 15 [196]. In total, ten measurements were taken for each sample, and average values were obtained with their respective standard deviations.

### 5.2.2 Tribological measurements of $Ti_2AlC$ and $Ti_3AlC_2$

Tribological measurements were performed under dry sliding conditions and at room temperature using a reciprocating ball-on-flat micro tribometer (Tetra-Basalt Must, Germany). The micro tribometer uses a 100Cr6 (AISI 52100) bearing steel ball (3 mm diameter) as a counter material. 100Cr6 steel is corrosion-resistant and is often used in various moving machine components. The coefficient of friction (CoF) was

calculated using the ratio of $F_t/F_n$. Where $F_t$ and $F_n$ represent the friction force and the normal force, respectively. The sliding speed ($V_s$) was set at 0.5 mm $s^{-1}$. The tests were performed using the following three normal forces: 50, 250 and 500 mN (see Figure 5.1). The total stroke length was 2.5 mm, and the number of cycles for each test was 100, resulting in a total sliding distance of 500 mm. For each force, three repetitions were performed with the test conditions described above. The average values of the CoF with their respective standard deviations are reported.

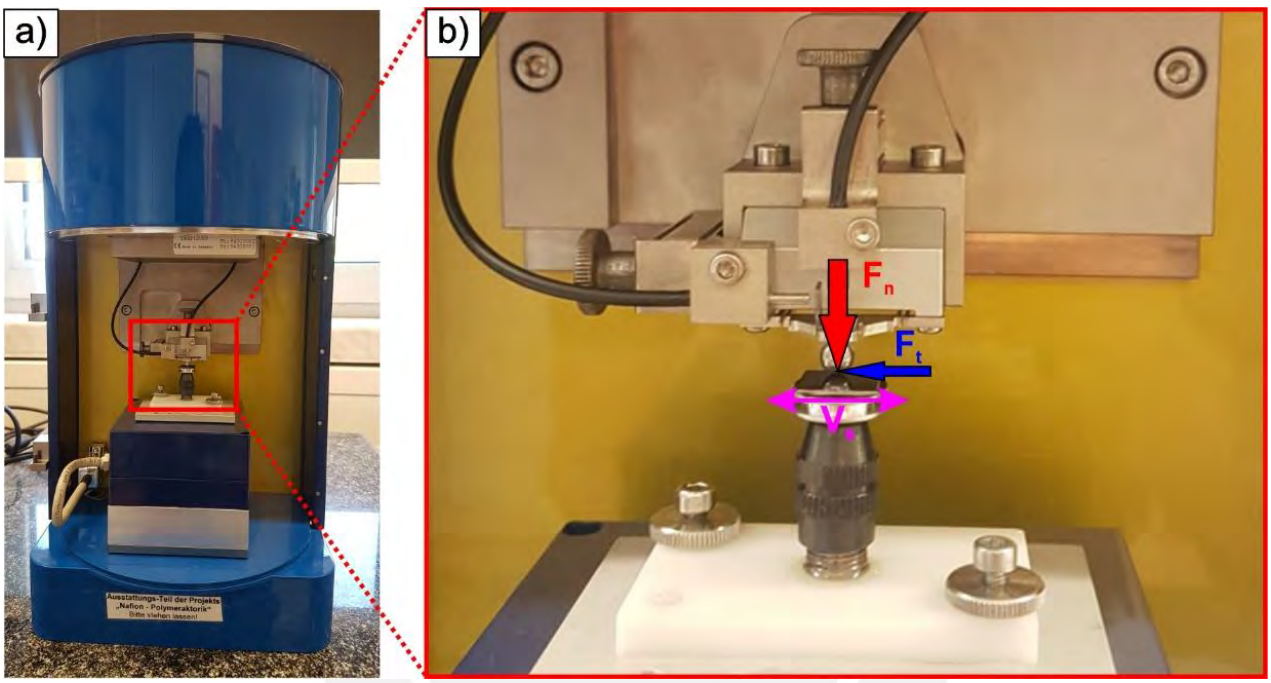


**Figure 5.1** *Ball on flat reciprocating Micro-Tribometer Tetra–Basalt. a) a general view of the used tribometer and b) details of the test configuration.*

### 5.2.3 Chemical composition and wear profile of worn tracks

The chemical composition of the worn tracks and the possible formation of tribofilms were investigated using Scanning Electron Microscopy (SEM, FEI Quanta 650). This device features an energy-dispersive X-ray detector (EDX). The acceleration voltage and emission current were set to 10 kV and 25 µA, respectively.

3D wear profiles were determined by atomic force microscopy (AFM, Dimension Icon device from Bruker). Due to the large size of the worn track, a scan rate of 0.1 Hz was used to avoid probe tip damage. A linear flattening procedure was applied to the wear track to eliminate tilt error.

## 5.3 Results and discussion

### 5.3.1 Mechanical performance of $Ti_2AlC$ and $Ti_3AlC_2$

Figure 5.2a) shows the load-displacement curves for $Ti_2AlC$, $Ti_3AlC_2$ and silicon, respectively. It can be seen that the lowest depth of penetration corresponds to the $Ti_2AlC$ phase indicating the highest hardness. On the other hand, Figure 5.2b) shows the hardness of $Ti_2AlC$, $Ti_3AlC_2$ and pure silicon as a function of the penetration depth. The results show that, at a depth of 50 nm, the hardness value of the $Ti_2AlC$ phase (11.6 ± 0.3 GPa) is approximately two times higher than the value corresponding to the $Ti_3AlC_2$ phase (5.3 ± 0. 9 GPa). This can be mainly attributed to its smaller grain size (see Figure 4.9). Grain boundaries act as energy barriers that impede the movement of dislocations [197,198].

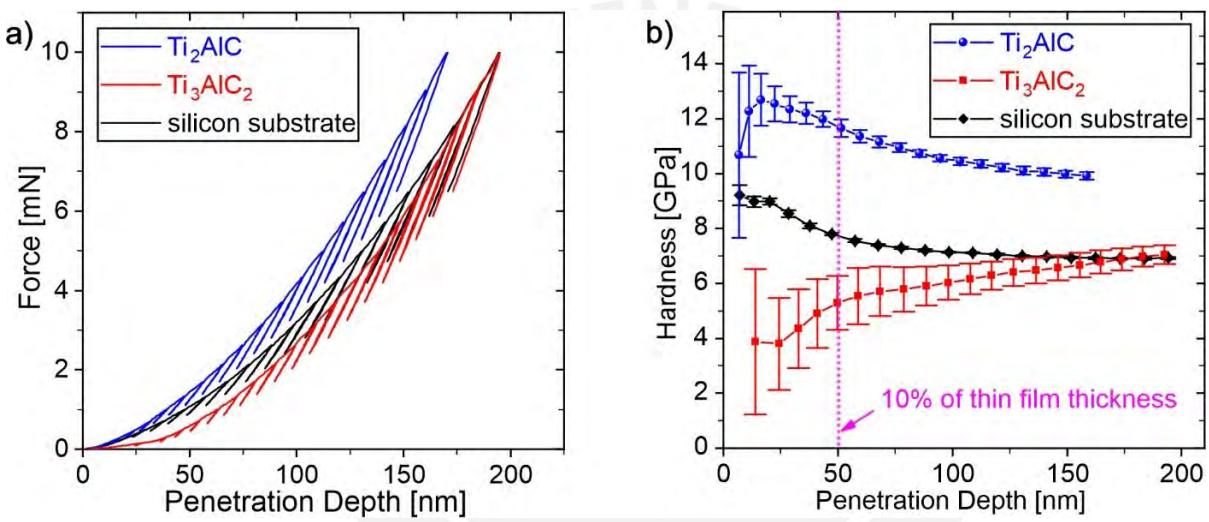


**Figure 5.2** *a) Curves corresponding to the load-displacement and b) hardness as a function of the penetration depth of $Ti_2AlC$, $Ti_3AlC_2$ and pure silicon tested at 10 mN.*

The hardness reported in the literature varies between 4.5 – 15.8 GPa and 1.0 – 11.4 GPa for $Ti_2AlC$ and $Ti_3AlC_2$, respectively [163]. It is observed that the results obtained are within the reported ranges. In Figure 5.2b), a significant dispersion of hardness can be seen at low penetration depths at around 10 nm. This variation in hardness is more critical in the rougher and softer film. The literature reports that this effect could be due to the surface roughness and the indentation size effect [199]. The surface roughness of the thin films was determined in Chapter 4, which are 4 nm and 12 nm for $Ti_2AlC$ and $Ti_3AlC_2$, respectively. At low penetration depths, a higher roughness increases the standard deviation of the measurements. At high penetration depths, it is observed that the hardness decreases for the $Ti_2AlC$ phase while it increases for the $Ti_3AlC_2$ phase. In both cases, they tend to be a constant at high penetration depths and furthermore resemble the hardness close to silicon. These results can be

attributed to the influence of substrate hardness. However, for the softer phase, the effect of the substrate is much more significant [200]. For example, at 150nm penetration, the hardness of the $Ti_3AlC_2$ phase approaches the hardness of pure silicon, a typical case of the hardness behavior of a soft film on a harder substrate [109,201].

### 5.3.2 Tribological behavior of $Ti_2AlC$ and $Ti_3AlC_2$

Figure 5.3a) shows a schematic representation of the tribological test of thin films against the bearing steel ball. Figure 5.3b) shows the CoF results obtained for the $Ti_2AlC$ and $Ti_3AlC_2$ phases as a function of the normal force. The results suggest that the CoF depends on the applied normal force [115,126]. The CoF of $Ti_2AlC$ thin films exhibits an increasing trend from 0.21 to 0.42 with increasing normal force from 50 to 500 mN. While the $Ti_3AlC_2$ phase shows a more marked CoF increase from 0.64 to 0.91 for 50 and 250 mN, respectively, and then shows a slight decrease to 0.83 for a force of 500 mN.

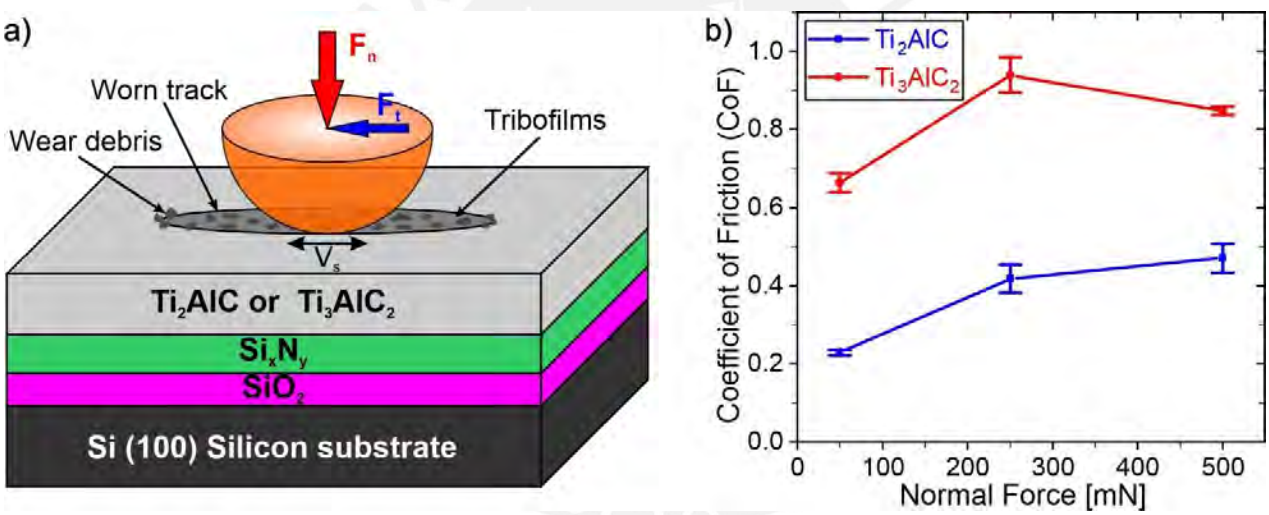


***Figure 5.3** a) a) Schematic representation of the wear track resulting from the tribological tests. b) The CoF of $Ti_2AlC$ and $Ti_3AlC_2$ against 100Cr6 for different normal loads (connection lines are visual guides only).*

Based on the results found in Chapter 4, it can be stated that the thin films of $Ti_2AlC$ and $Ti_3AlC_2$ show a certain degree of texture. In addition, they have different grain sizes, hardness and roughness levels. These properties influence the tribological behavior of the films. The reciprocating nature of the tribological test leads to a change in the tangential force direction with each cycle (see Figure 5.3a). Also, the tangential force acts parallel to the surface of thin films. Depending on the preferred orientation or texture of the films, the basal planes of the nanolaminate thin films can be oriented in the direction parallel to the surface. The tangential force could delaminate these basal planes quite easily. The layered crystal

structure of the MAX phases is very similar to the crystal structure of graphite [192]. The RTC results suggest that the $Ti_3AlC_2$ phase has a preferred orientation in the direction of the basal planes, which is parallel to the surface of the $Ti_3AlC_2$ film. In contrast, the $Ti_2AlC$ phase combines preferred orientations (basal, prismatic and pyramidal). As explained previously, the basal planes of the $Ti_3AlC_2$ phase are edge-indented by the tangential force and the direction of the indentation changes with each cycle. This causes delamination of the nanolaminar layers due to sliding dislocations of the basal planes. This generates cracks and laminar debris parallel to the basal planes in the worn track [133]. In contrast, due to the mixed preferred orientation for the $Ti_2AlC$ phase, delamination and debris generation is expected to be reduced.

The variation of the CoF as a function of the applied normal force is shown in Figure 5.3b). This transition from low CoF at low forces to high CoF at high forces can be attributed to the accumulation of wear debris between the friction surfaces. This causes abrasion of the third body. Since the $Ti_2AlC$ phase is harder than the $Ti_3AlC_2$ (see Figure 5.2b)), the hardness becomes important in this thin-film tribological system. The higher hardness of $Ti_2AlC$ reduces the probability of generating wear debris, reducing third-body abrasion and, thus, the coefficient of friction.

### 5.3.3 Wear track analysis

Figure 5.4 shows the SEM micrographs and the results of the chemical composition of the track obtained by EDX. Measurements were taken on the $Ti_2AlC$ wear track in a direction perpendicular to the slip direction. These measurements were taken for three different normal loads (50, 250 and 500 mN). Figure 5.4a), c), and e) show the linear scan measured in the SEM micrographs, while Figure 5.4b), d), and f) summarize the elemental chemical composition obtained along the blue arrow indicated in their respective SEM micrograph.

In the region outside the wear track, the concentration of the elements (Ti, Al and C) of the $Ti_2AlC$ phase remains almost constant. Additionally, small amounts of Si, O and N can be observed, and these elements are used as a diffusion barrier ($Si_xN_y$ and $SiO_2$) and are present in the substrate (Si). An acceleration voltage of 10 kV was used to quantitatively identify the atomic concentration of the film and the substrate. These data provide qualitative information on the change in thickness produced by tribological wear. An increase in silicon concentration indicates a reduction in thickness.

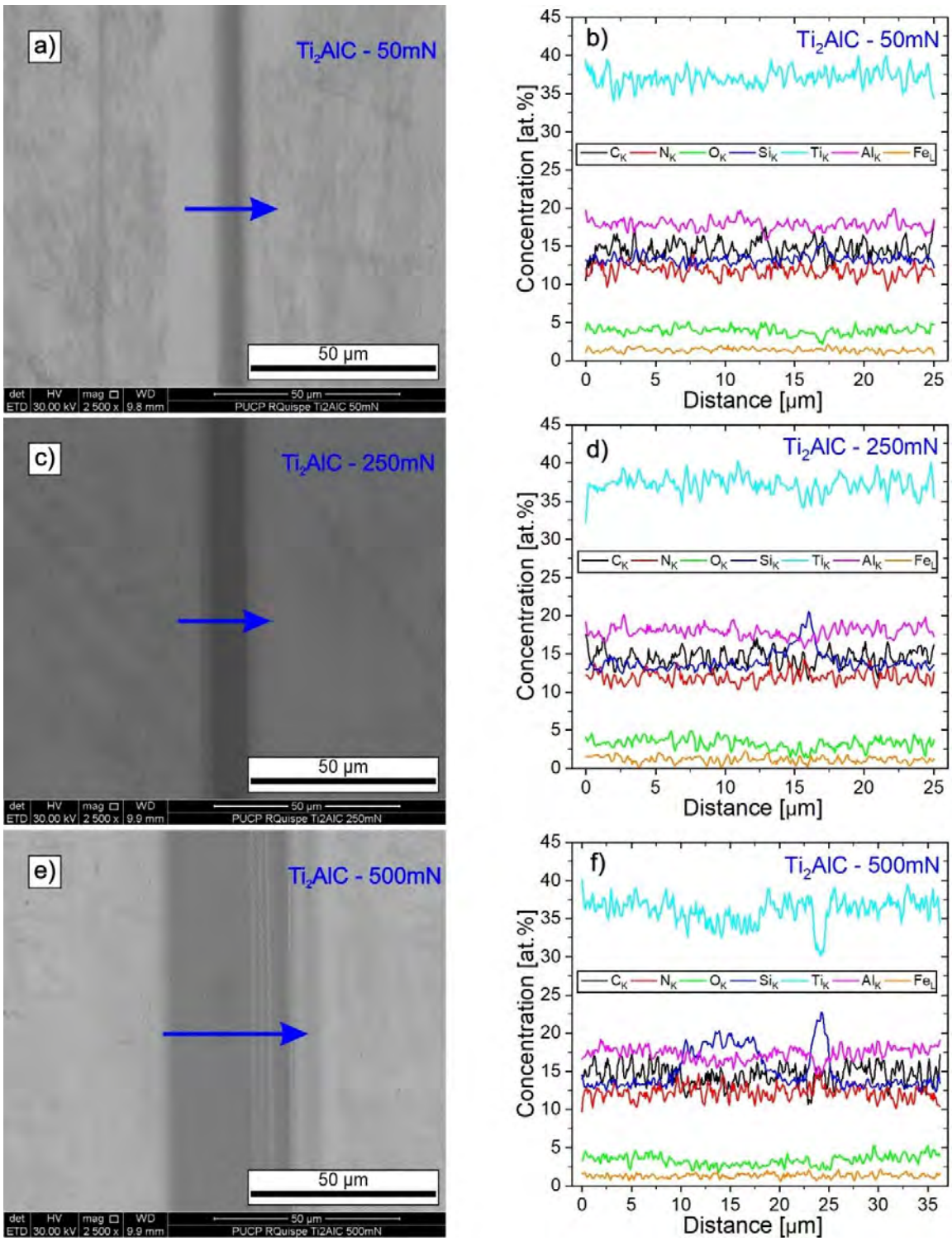


**Figure 5.4** *SEM-EDX analysis of $Ti_2AlC$ at 10 kV. SEM-micrographs of the wear track at a) 50, c) 250, and e) 500 mN. Track composition at b) 50, d) 250, and f) 500 mN.*

Figure 5.4b) shows line scan results corresponding to a normal force of 50mN. The curves corresponding to this measurement show an almost constant trend of the atomic concentration inside and outside the track. These results suggest that the wear is minimal and does not alter the atomic concentration of the measurements. On the other hand, Figure 5.4d) and f), corresponding to normal forces of 250 and 500 mN, respectively, show slight changes in atomic concentration within the wear track. A slight increase in the concentration of silicon and a decrease in the concentration of titanium and aluminum are shown. This suggested a reduction in film thickness at the wear track and increased CoF due to debris. Furthermore, for a normal load of 500 mN, an increase in the width of the wear track and silicon concentration in the track is observed compared to the other wear tracks.

Finally, it is possible to detect tiny traces of iron atoms (around 1.50 at. %) in the wear tracks for 50 and 500 mN. The presence of iron atoms in the wear track indicates a transfer of material from the counter material to the film, thus verifying adhesive wear.

Similar to the results described for $Ti_2AlC$, Figure 5.5a) to f) show the wear tracks and the chemical composition of $Ti_3AlC_2$ thin films after tribological testing with normal loads of 50, 250, and 500 mN, respectively. Figure 5.5b), d), and f) show an almost constant elemental composition of the MAX phase at the track limits for all tracks. For the track obtained at 50 mN (Figure 5.5b)), a slight increase in the oxygen and iron concentration in the middle of the track can be observed. However, all remaining elements do not show significant changes, which suggests that only minor wear has occurred.

Figure 5.5d) and f) show that the amount of iron and oxygen notably increases with increasing normal load. At the track limits, the elemental composition remains almost constant. Furthermore, it can be observed that oxygen increases in the same proportion as iron. The presence of oxygen and iron verifies material transfer from the counter-material and points towards the potential formation of iron oxides during friction. Additionally, the concentration of silicon increases in the wear track, while the main elements of the MAX phase decrease with increasing normal load. This can be attributed to a considerable decrease in film thickness due to wear, which holds especially true in the middle part of the track (highest velocity) and for higher loads.

Furthermore, comparing the SEM micrographs tracks of $Ti_3AlC_2$ and $Ti_2AlC$, the $Ti_3AlC_2$ phase demonstrates a considerably larger width. For instance, at 50 mN, the wear track width for $Ti_3AlC_2$ is approximately 130 µm, whereas the width of $Ti_2AlC$ is only about 10 µm.

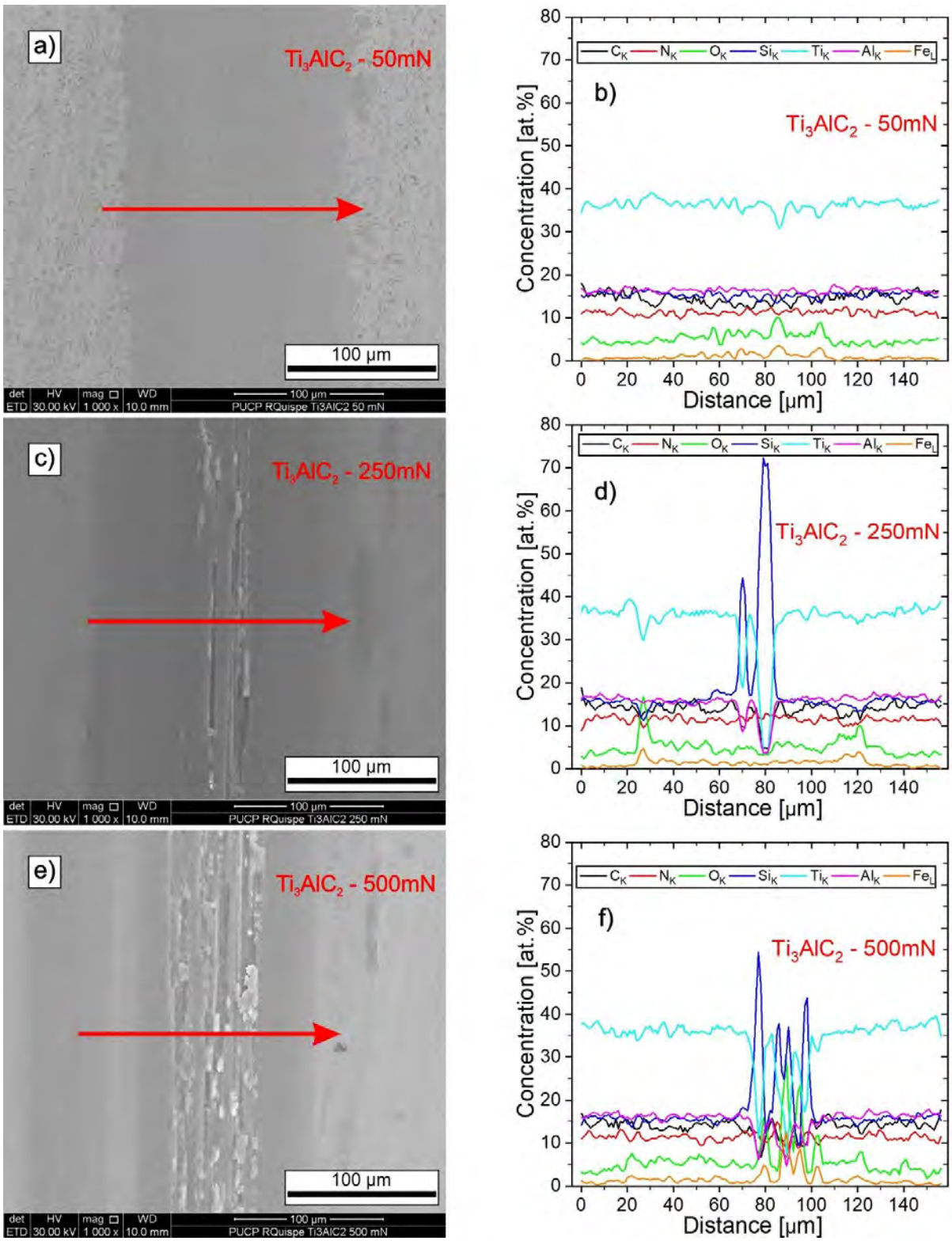


**Figure 5.5** *SEM-EDX analysis of $Ti_3AlC_2$ at 10 kV. SEM-micrographs of the wear track at a) 50, c) 250, and e) 500 mN. Track composition at b) 50, d) 250, and f) 500 mN.*

Figure 5.6a) shows a 3D AFM image of the wear track of $Ti_2AlC$ at 500 mN. The track has a width of approximately 15 µm. The debris formation can be explained by layer delamination, kinking band formation, and crack generation in the basal planes as described in [115]. Furthermore, Figure 5.6b) shows a part of the wear track of $Ti_3AlC_2$ at 500 mN. In this case, the wear track is considerably broader and did not fit into the measurement range of the AFM. Nevertheless, Figure 5.6b) reveals that the surface of the $Ti_3AlC_2$ has a higher roughness than the wear track of $Ti_2AlC$. Since $Ti_3AlC_2$ has a lower hardness, the sample demonstrates more severe wear, thus resulting in extensive damage and higher friction.

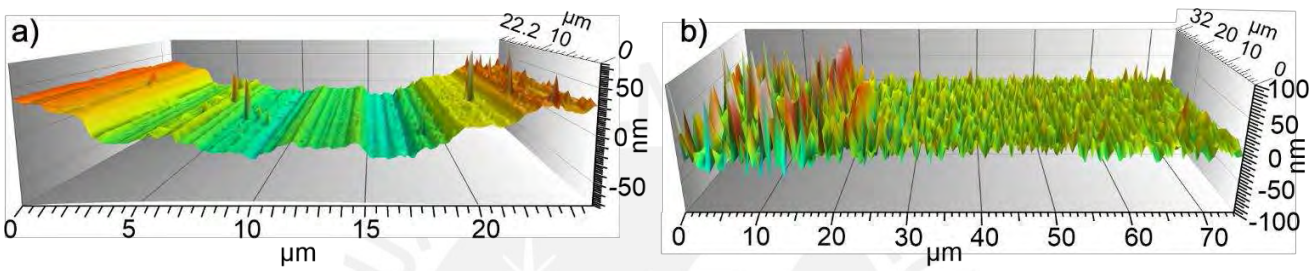


**Figure 5.6** *Wear track profiles measured by AFM after tribological tests using a normal of 500 mN for a) $Ti_2AlC$ and b) $Ti_3AlC_2$ (part of the track), respectively.*

Some recent experimental studies and atomistic simulations on the deformation mechanism of layered crystalline solids suggest the formation of ripplocation boundaries at the initial state, which are capable of propagating rapidly, thus forming kinkings [202,203]. Figure 5.7 shows the kinking formation in the wear track of $Ti_2AlC$ at 500 mN. During the tribological test, the normal and tangential forces (friction forces) are perpendicular and parallel to the basal planes, respectively. In this case, the friction force acts on the basal planes in edge-on compression. After tribological testing, kink bands in opposite directions can be observed (Figure 5.7), which may originate from ripples of the atomic layers or ripplocations [204]. The current literature is mainly limited to simulations and experimental studies on monocrystalline materials. In these studies, an edge-on compression load is applied in the basal planes. More detailed analyses of normal and tangential forces acting on polycrystalline materials are needed.

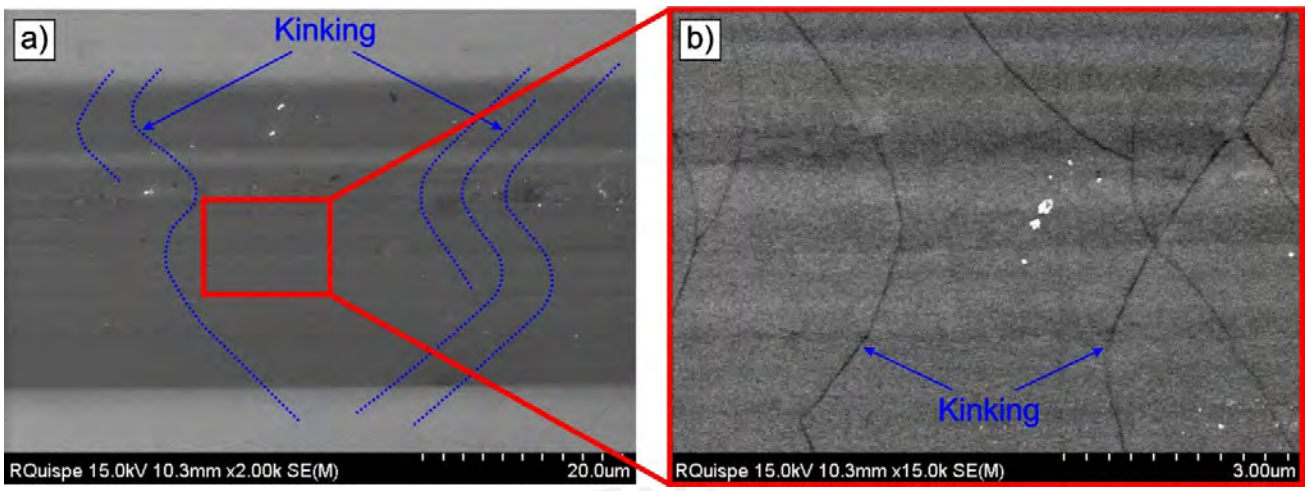


**Figure 5.7** *SEM micrographs of the kinking formation were observed in the wear track after tribological testing of $Ti_2AlC$ at 500 mN.*

## 5.4 Conclusions

In this chapter, the hardness and tribological properties of the $Ti_2AlC$ and $Ti_3AlC_2$ phases were evaluated. Tribological properties obtained under dry sliding conditions were correlated with hardness and the results of roughness, grain size, and texture. Nanoindentation tests show that the $Ti_2AlC$ phase (11.6 ± 0.3 GPa) is harder than $Ti_3AlC_2$ (5.3 ± 0.9 GPa). This higher hardness of the $Ti_2AlC$ phase can be attributed to the preferred mixed orientation and smaller grain size compared to the $Ti_3AlC2$ phase. The $Ti_2AlC$/bearing steel ball system shows a CoF between 0.21 and 0.42 in a normal load range of 50 to 500 mN. However, the $Ti_3AlC_2$/bearing steel ball system shows CoF values between 0.64 and 0.91 for the same normal load range. Based on the results, the $Ti_2AlC$ phase shows better tribological properties than $Ti_3AlC_2$. This behavior can be attributed to its higher hardness, smaller grain size and lower surface roughness. The SEM-EDX analysis of the worn tracks reveals that there is a transfer of material from the ball to the thin film ($Ti_3AlC_2$). This generated a wear debris accumulation between the sliding surfaces, causing a third-body abrasion and a high frictional force and wear.

# Chapter 6. Electro-tribological performance under electric current of $Ti_2AlC$ and $Ti_3AlC_2$ thin films

## 6.1 Introduction

This chapter correlates electrical and mechanical properties with thin film electro-tribological performance. The resistivities of the $Ti_2AlC$ and $Ti_3AlC_2$ thin films were 0.73 and 0.45 μΩ·m, respectively. Tribological tests were carried out under electric current. The variation of the coefficient of friction (CoF) and the electrical contact resistance (ECR) is evaluated as a function of the sliding distance. A connection between the CoF and the ECR is evident. In small sections, it can be seen that the CoF increases while the ECR decreases. Furthermore, the wear track left by the tribological tests is studied. SEM-EDX analyzed the contact surface of the counter material. Fusion and material transfer between the film and bearing steel ball were found.

## 6.2 Experimental details

### 6.2.1 Electrical resistivity measurements of $Ti_2AlC$ and $Ti_3AlC_2$ thin films

The electrical resistivity of the thin films was determined using the linear Van der Pauw method applying an electrical current of 0.1 mA. The measurement system consists of a Keithley 2400 current source and two Keithley multimeters to measure the resulting current and voltage. The four contact tips use a spring system to maintain uniform pressure on the film and establish good electrical contact. Current-voltage measurements were performed to ensure that all samples have ohmic behavior.

### 6.2.2 Setup of tribology under electrical currents of $Ti_2AlC$ and $Ti_3AlC_2$

Figure 6.1 shows a schematic representation of the tribological test under electric current. The Keithley SourceMeter device was used to supply 10, 50 and 100 mA electrical current during the tribological experiments. The electric current and voltage passing through the electrical contact between the ball and the MAX phase thin film were measured using an amperemeter and voltmeter. These current and voltage data were collected using the LabVIEW program to process the data later and determine the Electrical Contact Resistance (ECR). Tribological tests under electric current were carried out using a reciprocate ball-on-flat micro-tribometer similar to the previously shown measurements (Tetra-Basalt Must, Germany) with a 3 mm diameter 100Cr6 bearing steel ball as a counter material. The normal forces used were: 50, 250 and 500 mN, the sliding speed was 0.5 mm/s. The stroke length was 2.5 mm, and the number of cycles was 100, resulting in a total sliding distance of 500 mm for each measurement.

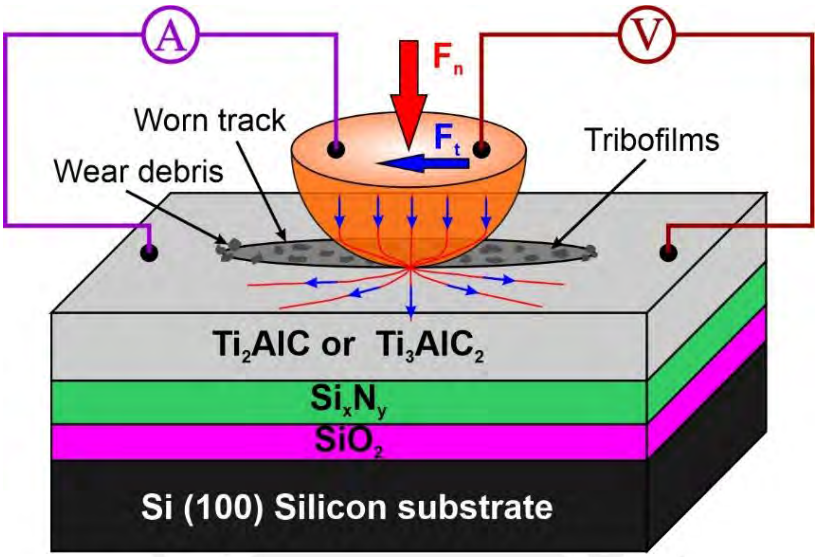


**Figure 6.1** *Schematic representation of the tribological test under electric current.*

## 6.3 Results and discussion

### 6.3.1 Electrical properties of $Ti_2AlC$ and $Ti_3AlC_2$

The electrical conductivity in MAX phases predominantly involves the transport of electrons. The electrons should overcome grain boundaries, which might act as barriers to electron movement. The size of the grains influences the electrical resistivity of thin films. The resistivity increases with decreasing grain size. This is mainly due to electron scattering at the grain boundaries and the film surface [70,205–207]. On the one hand, the $Ti_2AlC$ thin film has a small grain size of ~10 nm. Thus, the resistivity of the $Ti_2AlC$ film (0.73 μΩ·m) is slightly higher than the values reported in the literature 0.36-0.44 μΩ·m (see Table 6.1). On the other hand, the $Ti_3AlC_2$ thin film has a considerably larger grain size than the $Ti_2AlC$ phase. Figure 4.9 shows a qualitative comparison of the grain size of both phases. Therefore, a lower resistivity is expected due to the lower dispersion effect of the grain boundaries. Thus, the $Ti_3AlC_2$ phase has a resistivity of 0.45 μΩ·m, and this value is within the range reported in the literature for this phase (0.29-0.51 μΩ·m).

**Table 6.1.** *Electrical resistivity and hardness of $Ti_2AlC$ and $Ti_3AlC_2$ MAX phases.*

| MAX phase | Electrical resistivity [μΩ·m] | | Hardness [GPa] | |
|---|---|---|---|---|
| | Experimental | Literature | Experimental | Literature |
| **$Ti_2AlC$** | 0.731 ± 0.002 | 0.36[53], 0.36[208], 0.37[184], 0.40[49], 0.44[209], | 11.6 ± 0.3 | 4.5[184], 4.8[210], 5.5[208], 5.8[49], 15.8[35] |
| **$Ti_3AlC_2$** | 0.452 ± 0.001 | 0.29[188], 0.35[183], 0.387[211], 0.51[209], | 5.3 ± 0.9 | 1.0[212], 3.5[183], 2.5-4.7[188], 11.4[85] |

### 6.3.2 Tribological performance under electrical current of $Ti_2AlC$ and $Ti_3AlC_2$

Figure 6.2-3 and 6.5-6 show the results of the tribological tests under the electric current of the $Ti_2AlC$ and $Ti_3AlC_2$ thin films, respectively. It is worth mentioning that the CoF and the ECR were determined simultaneously in the same electro-tribological experiment.

#### *6.3.2.1 Tribology and electrical contact resistance of $Ti_2AlC$ thin film*

Figure 6.2a), b), c), and d) show the evolution of the CoF and the ECR for the $Ti_2AlC$ film as a function of the sliding distance. The testing parameters were 50 mN and the electric currents of 0, 10, 50 and 100 mA. Figure 6.2a) shows the evolution of the CoF for the $Ti_2AlC$ phase at 50 mN but without electric current. In this case, the CoF remains around 0.19. In the tests with electric current, a slight increase in CoF is observed with the increasing electric current. This increase in CoF could be due to welding, erosion, and material transfer due to friction under electrical current flow.

Figure 6.2b) shows a high variation of the ECR during the electro-tribological test under 50 mN and 10 mA conditions. This suggests that the ECR depends on the normal force, the applied current intensity and the surface conditions of the real contact area. The 100Cr6 steel ball has an initial roughness of 16 nm [114], and the $Ti_2AlC$ and $Ti_3AlC_2$ films have a roughness of 4 and 12 nm [30]. In addition, the ball and film may have a surface layer of insulating oxide and adsorbed water molecules. The force of 50 mN and the current of 10 mA are not enough to establish good electrical contact. This results in a wide variation of the ECR, with a slight reduction at the end of the test. Figure 6.2c) shows a much more stable and lower ECR at the same 50 mN force but with an electrical current of 50 mA. Here it should be noted that a current intensity of 50 mA might lead to removing possible oxide layers. Thus, the formation of better electrical contact results in higher stability and a decrease in the ECR. This effect is known as softening of the interface due to the increase in temperature by the electric current. This softening could increase

the contact area. Figure 6.2d) shows a similar trend to that described previously but an even lower ECR, with specific local and momentary trends to decrease when CoF increases.

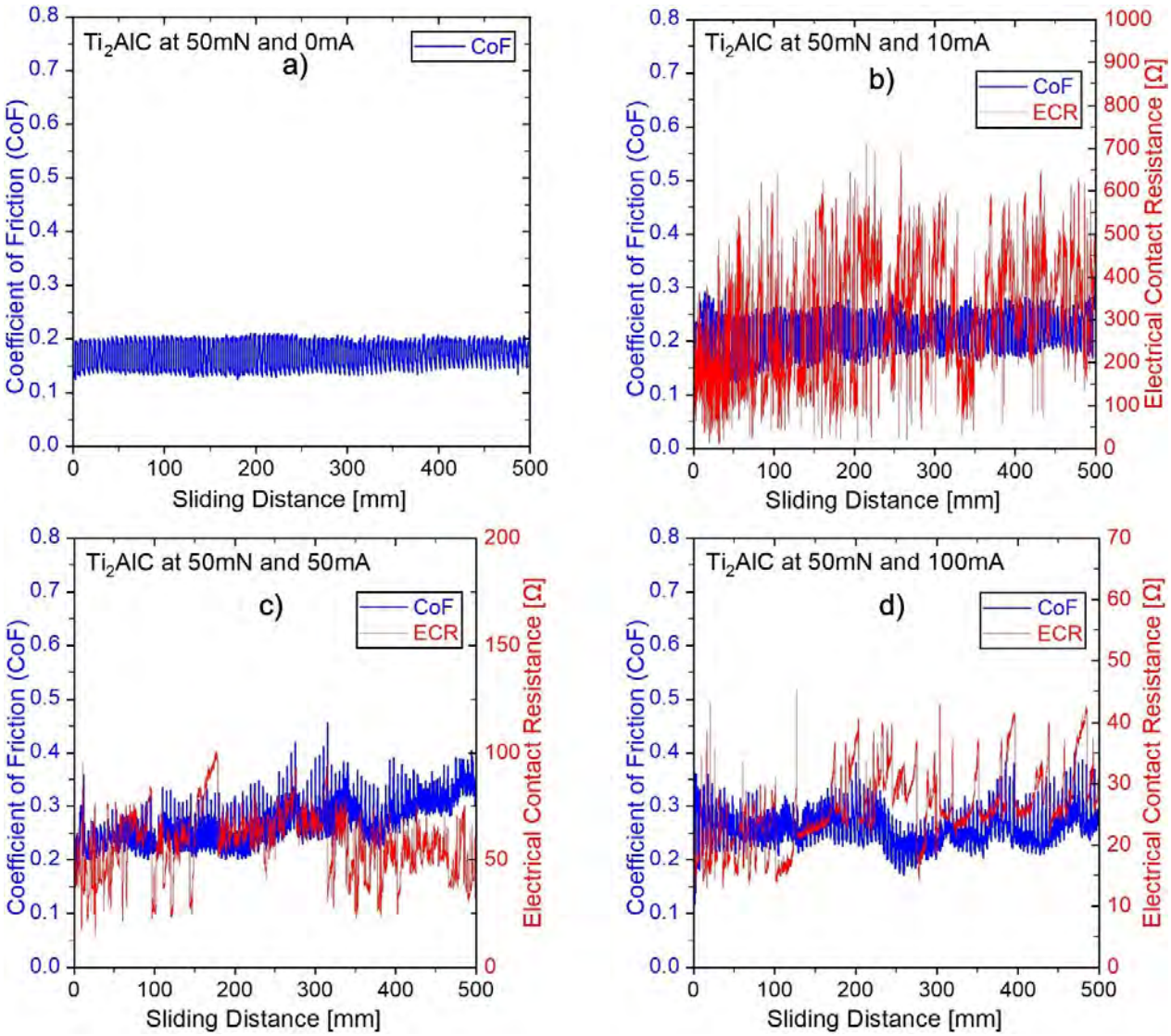


**Figure 6.2** *Coefficient of friction and electrical contact resistance of $Ti_2AlC$ at 50 mN: a) 0, b) 10, c) 50, and d) 100 mA.*

Figure 6.3a), b), c), and d) show the CoF and ECR at 500 mN and 0, 10, 50 and 100 mA for $Ti_2AlC$ thin films. It is observed that a higher electric current has a more stable and lower value of ECR, while an increase in CoF is observed compared to the tests using a force of 50 mN. The real electrical contact area between the ball and the thin film available for conduction increases due to the increasing normal force [160]. This decreases the ECR and, at the same time, increases the CoF. However, even mechanical contact between the ball and the film exists. Still, it does not guarantee excellent electrical

contact because it could be insulating oxide layers at the interface generated by the tribological test. The oxides or tribo-films of the track decrease the CoF but increase the ECR. Investigations on sliding contacts suggest that the electric current favors the formation of insulating oxide layers, resulting in a reduction of CoF [74,213,214]. On the other hand, the results suggest that the possible fracture and dispersion of the oxides increase the CoF and decrease the ECR momentarily. The sudden change and possible loss of the real electrical contact area due to the tribological test explains the large dispersion of the ECR values.

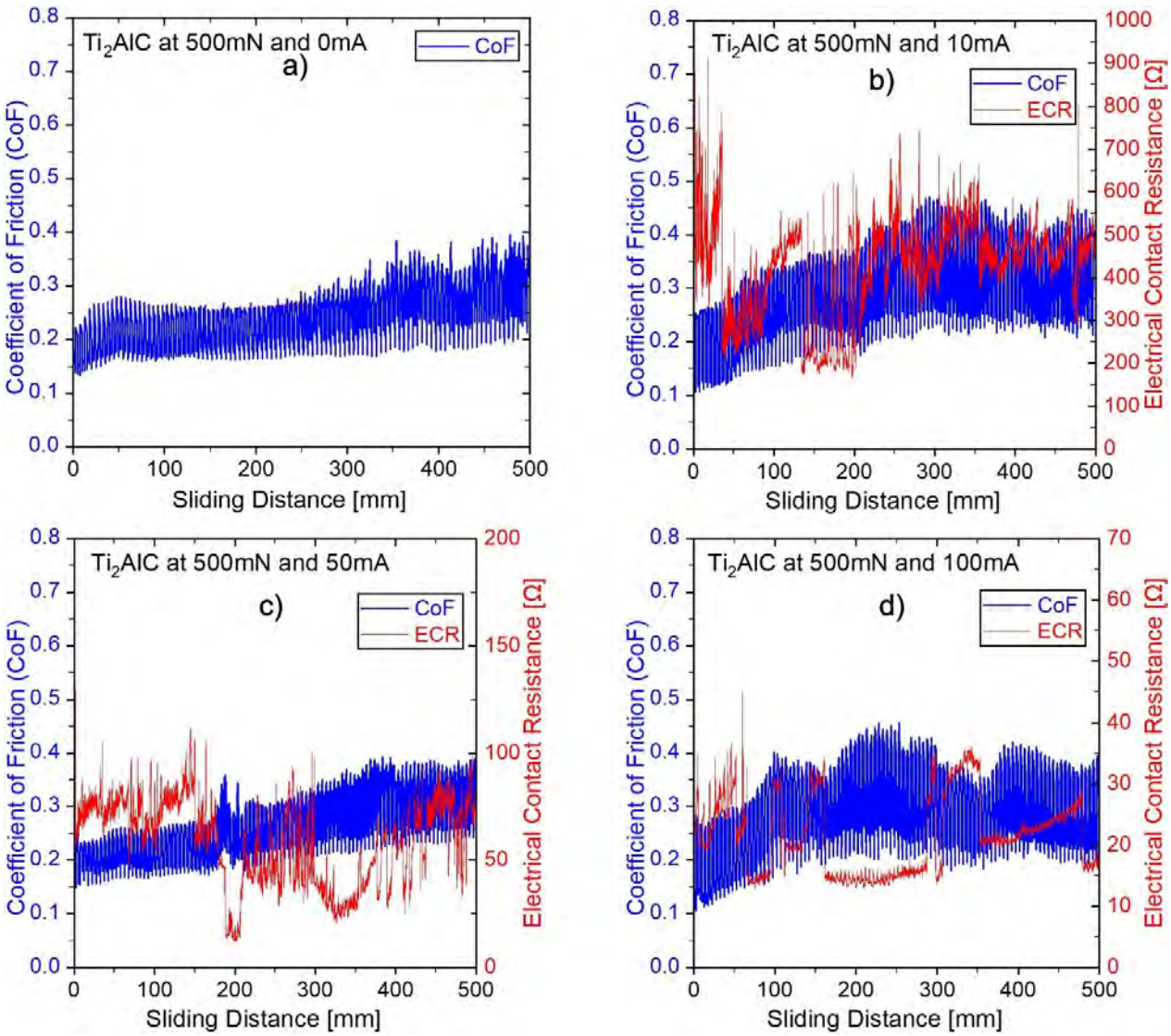


**Figure 6.3** *Coefficient of friction and electrical contact resistance of $Ti_2AlC$ at 500 mN: a) 0, b) 10, c) 50, and d) 100 mA.*

The contact interface temperature can exceed the melting point if the contacts become momentarily separated [157] or if tribo-films composed of insulating oxides form at the interface. For steel, the boiling temperature corresponds to a voltage difference between the contacts of 0.55 V [160]. The final part of the boiling stage manifests as an explosion of superheated ionized steam, the same one that precedes the formation of the electric arc with an arc voltage of 10 to 15 V [157].

Figure 6.4a) and b) show the tracks of the $Ti_2AlC$ samples tested at 50 mN (10 mA) and 500 mN (100 mA), respectively. The worn track at 50 mN is considerably smaller than the track obtained after the 500 mN test. This change in size is somewhat to be expected using a force with a difference of 10 times between both tracks. Furthermore, the increase in the size of the track at 100 mA could be due to the softening of the contact interface as a result of the increase in temperature. In addition, it is observed that the films were not removed from the substrate.

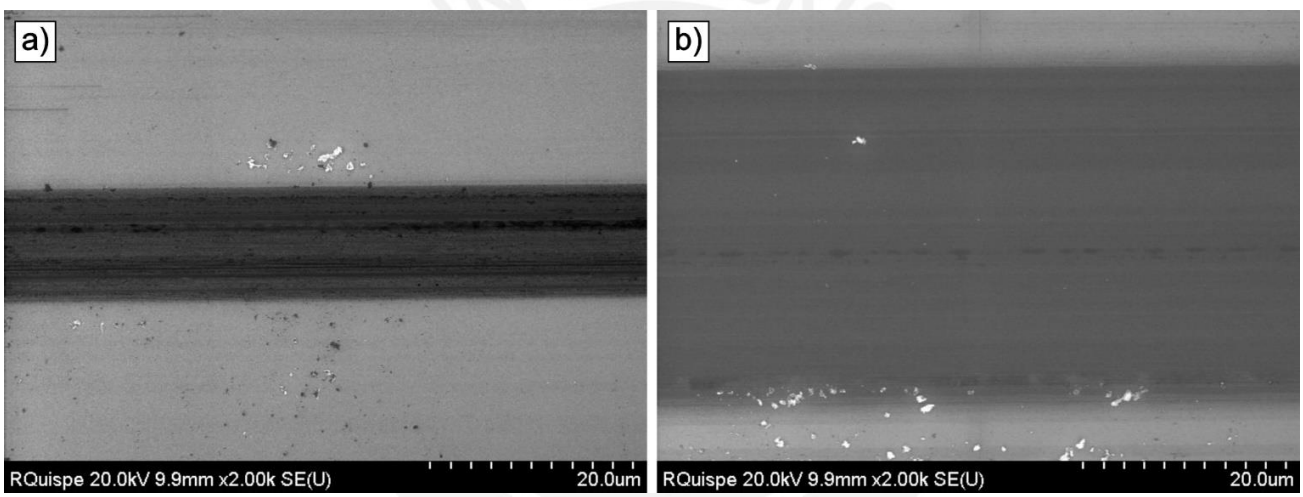


**Figure 6.4** *SEM micrographs of the $Ti_2AlC$ tracks. a) 50 mN and 10 mA, and b) 500 mN and 100 mA.*

### *6.3.2.2 Tribology and electrical contact resistance of $Ti_3AlC2$ thin film*

Figure 6.5 shows the friction coefficient and electrical contact resistance of the $Ti_3AlC_2$-steel ball tribo-pair at a normal force of 50 mN under electrical currents of 0, 10, 50 and 100 mA. The CoF of the tribo-pair without electric current (0 mA) and at 10 mA is in the range of 0.6-0.85 and 0.4-0.95, respectively. In addition, a running-in effect can be seen at the beginning; after this effect, the CoF decreases progressively with sudden increases due to possible momentary welds. Figure 6.5b) shows the ECR and CoF at 50 mN and 10 mA. In the beginning, it can observe a slight increase in the ERC to later remain stable around 300 Ω. The CoF and ECR results suggest that the film remains intact under these test

conditions. Figure 6.5c) shows the results of ECR and CoF at 50 mN and 50 mA, below 250mm of sliding distance; a stable value is observed with slight increases in ECR. The CoF shows the typical initial running effect in this material. However, at a sliding distance greater than 250 mm, an apparent abrupt increase in ECR and change in CoF is observed. This undoubtedly suggests the complete removal of the film. Figure 6.5d) shows the results of ECR and CoF at 50 mN and 100 mA. The trend is very similar to that previously described, but at 100 mA the results suggest that the film is removed from the substrate even at a shorter sliding distance (~150 mm).

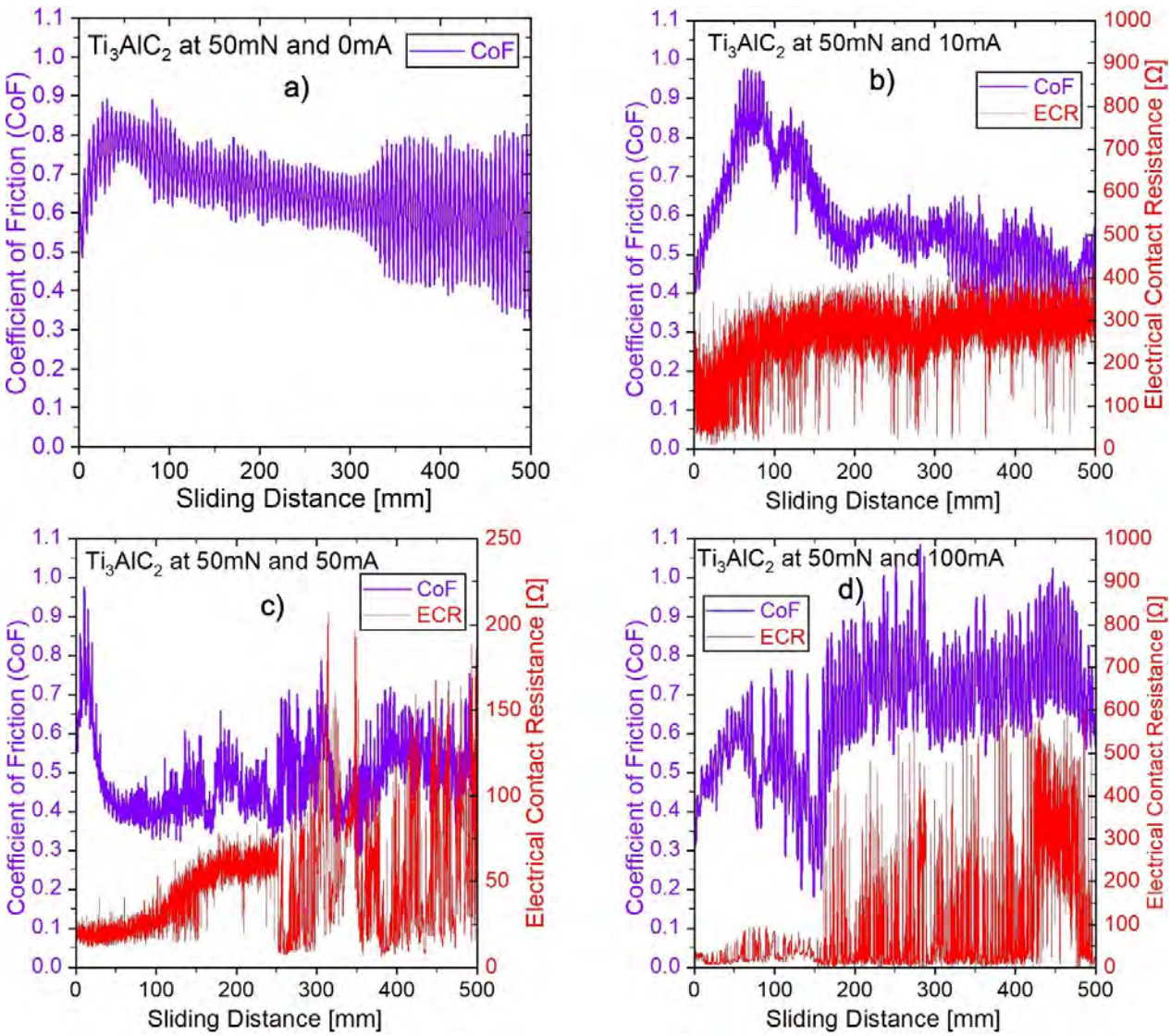


**Figure 6.5** *Coefficient of friction and electrical contact resistance of $Ti_3AlC_2$ at 50 mN: a) 0, b) 10, c) 50, and d) 100 mA.*

The previously discussed phenomena could be attributed to the interface temperature of the tribo-pair being slightly higher than the system temperature in good electrical contact. However, in sliding contact due to the formation of oxides, the interface temperature increases and accelerates the deterioration of the contact area. The damage is cumulative, leading to increased ECR, increased interfacial temperature, erosion, possible momentary welding joints, material transfer, short-circuit conditions, and eventual failure of the contact interface [160].

Figure 6.6 shows the CoF and ECR of $Ti_3AlC_2$-steel ball tribo-pair, at normal force of 500 mN, under electrical currents of 0, 10, 50 and 100 mA. Figure 6.6a) shows that the CoF remains constant without electric current at around 0.9. Figure 6.6b) shows the CoF and ECR at 500 mN and 10 mA. The CoF remains constant at approximately 0.55; similarly, a stable ECR is observed at about 400 Ω. As in the previous case at 10 mA, the CoF and ECR results suggest that the film remains intact under these test conditions. Figure 6.6c) shows the CoF and ECR at 500 mN and 50 mA. The results show that the CoF increases progressively with the increase of the sliding distance. The abrupt increase of the ECR demonstrates that the film becomes removed at sliding distances less than 100 mm. Figure 6.6d) shows the CoF and ECR at 500 mN and 100 mA. The CoF shows a running effect, which varies between 0.45-0.75 until reaching the sliding distance of 350 mm, to increase subsequently. The ECR shows different behavior for sliding distances less than and greater than 250 mm. The low ERC at distances less than 250 mm could be due to the higher normal force (500 mN) favors the formation of good electrical contact between the film and the steel ball. It shows a temporary increase in the ERC due to possible losses of electrical contact by sliding and reciprocating movement of the tribological test. But above 250 mm, a progressive rise in ECR is observed. This result suggests that, at this point starts, the film's destruction.

The previously discussed behavior could be due to the CoF being increased by debris on the track, flash welds, and eroded interface. As the electrical contact interface deteriorates, these molten and eroded zones rub over new areas in the worn path, causing the electrical contact to overheat and oxides to form due to high-temperature material transfer and reaction chemistry with the surrounding medium. In the same way, the ERC is also increased, mainly because the oxides in the contact interface and the erosion reduce the real electrical contact area, increasing the resistance to the passage of the electric current.

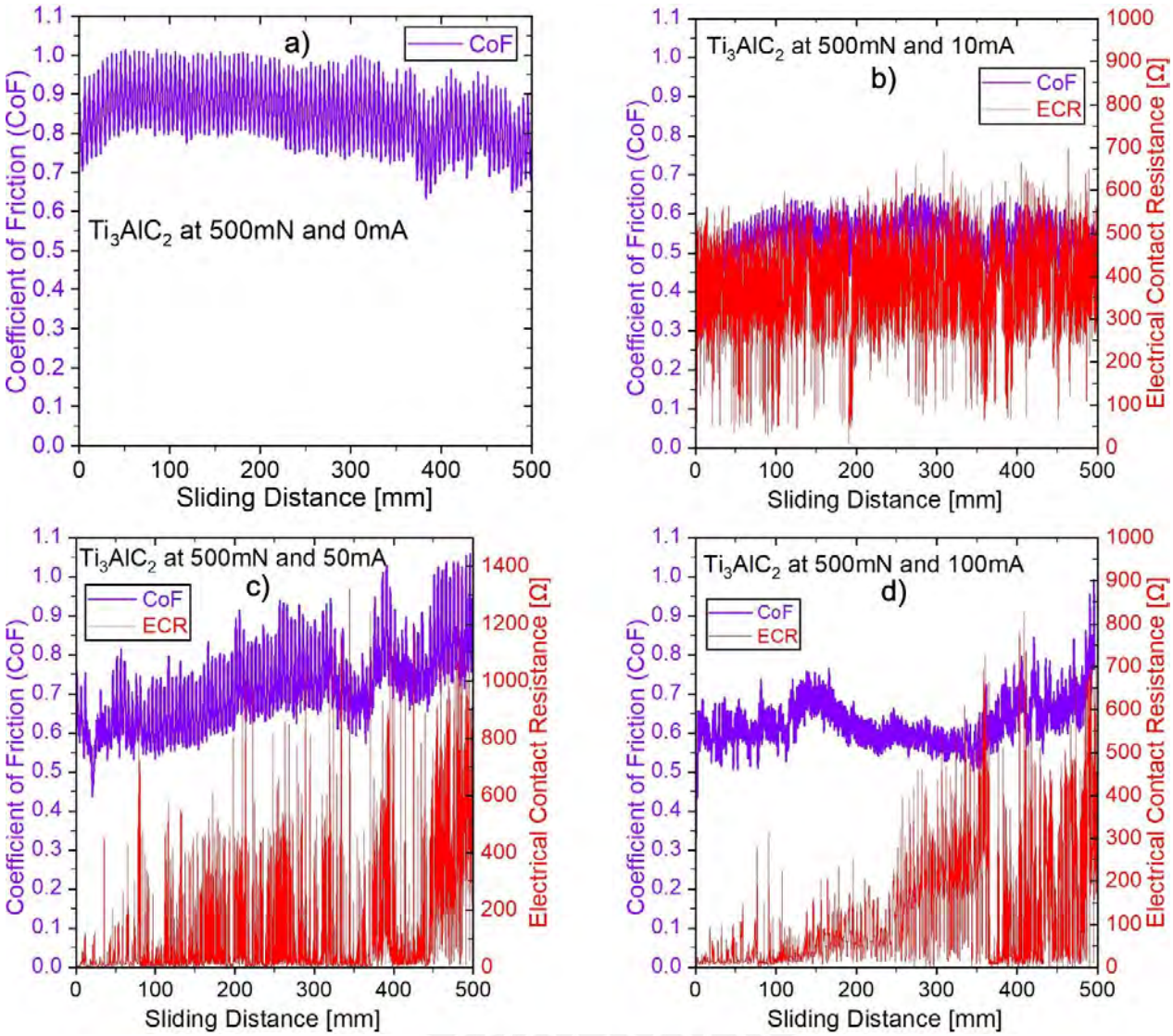


**Figure 6.6** *Coefficient of friction and electrical contact resistance of $Ti_3AlC_2$ at 500 mN: a) 0, b) 10, c) 50, and d) 100 mA.*

Figure 6.7a) shows the tracks of the $Ti_3AlC_2$ samples tested at 50 mN and 10 mA. A medium-worn track with no evidence of film removal is shown in this micrograph. However, Figure 6.7b) shows the catastrophic failure of the $Ti_3AlC_2$ film after the electro-tribological test at 500mN and 100 mA. The film was completely removed during the electro-tribological test. In addition, electric arcs are responsible for the film's deterioration and remotion from the substrate.

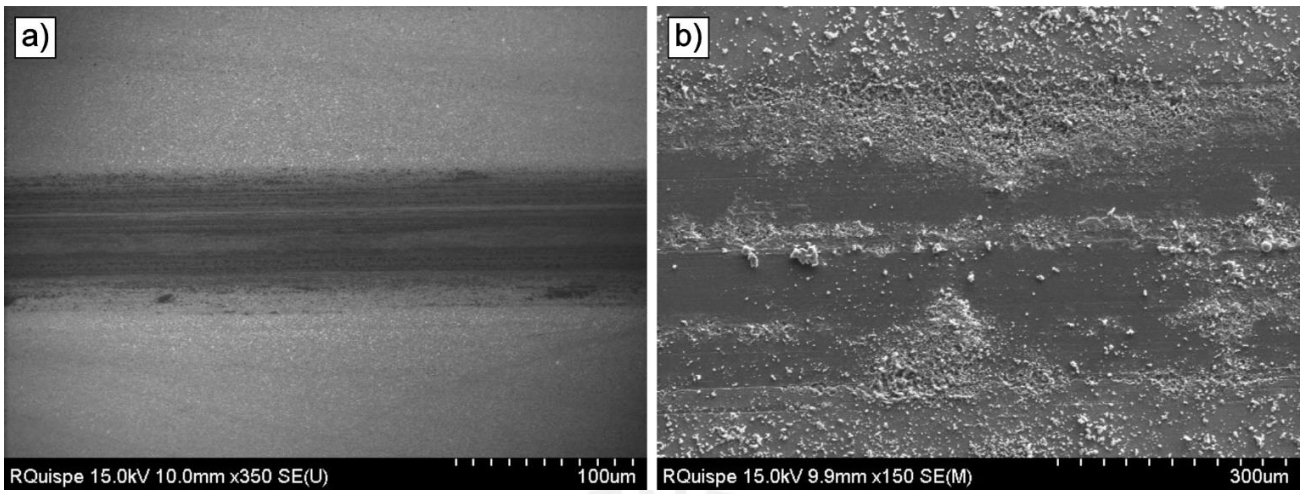


**Figure 6.7** *SEM micrographs of the $Ti_3AlC_2$ tracks. a) 50 mN and 10 mA, and b) 500 mN and 100 mA.*

### *6.3.2.3 Analysis of the balls used in the electro-tribological test.*

Figure 6.8 shows various SEM micrographs and the composition of the ball as a counter body after the electro-tribological assay of $Ti_2AlC$ against 100Cr6 at 500 mN and 100 mA. Figure 6.8a) shows a general view of the 3 mm diameter ball used in the measurements. Figure 6.8b) offers a magnification of the contact area. Figure 6.8c) shows the eroded surface in greater detail. The formation of pores, solidifications, pits and protuberances produced by the electric arcs formed during the test can be seen. Due to the high energy of the electric arc, it is observed that certain points of the contact surface of the ball melt and subsequently solidify. Figure 6.8d) shows a typical brittle fracture in the enlarged image of the eroded area B. The generation and propagation of cracks could be due to embrittlement resulting from the high temperatures and the formation of oxides on the ball contact area. Figure 6.8e) shows an enlarged image of area A, showing circular cavities produced by material erosion. Figure 6.8f) shows the composition of certain points of interest in the contact area. The presence of Ti, Al and C atoms is observed. This clearly indicates a material transfer from the thin film ($Ti_2AlC$) to the ball. In addition, a high oxygen concentration could be observed in the different zones, which suggests that due to the high temperatures generated by the electric arc and the interaction in the surrounding medium, aluminum, titanium and iron oxides are formed. The other elements observed in less quantity are typical of the composition of 100Cr6 steel.

Only a tiny part of this eroded area could conduct electrical current, whereas on the rest of the surface, due to the formation of insulating oxides and debris from arcing and abrasive wear, no electric current flows. This real electrical contact area dramatically influences the electrical contact resistance. This is

why a significant variability of the ECR can be observed described in the previous sections. When electric current passes through the contact surfaces, the current flow is concentrated at the contact points or asperities. The local current density increases to a very high value, generating heat in the contact area. Depending on the resistance of the oxide film (tribo-films) formed during the electro-tribological test, the current's slow passage or the arc's formation in the contact zone occurs. The main consequence of arcing is the wear of the film and counterpart surfaces by removing molten material in the arc, resulting in cracks and burnt craters (see Figure 6.8c)). Due to this, the surface roughness and the mechanical wear of both surfaces are increased. Arcing, cratering, mechanical polishing of contact surfaces, and released metal particles cause rust on the worn path and counterpart. Therefore, the deterioration of the contact surfaces gradually increases.

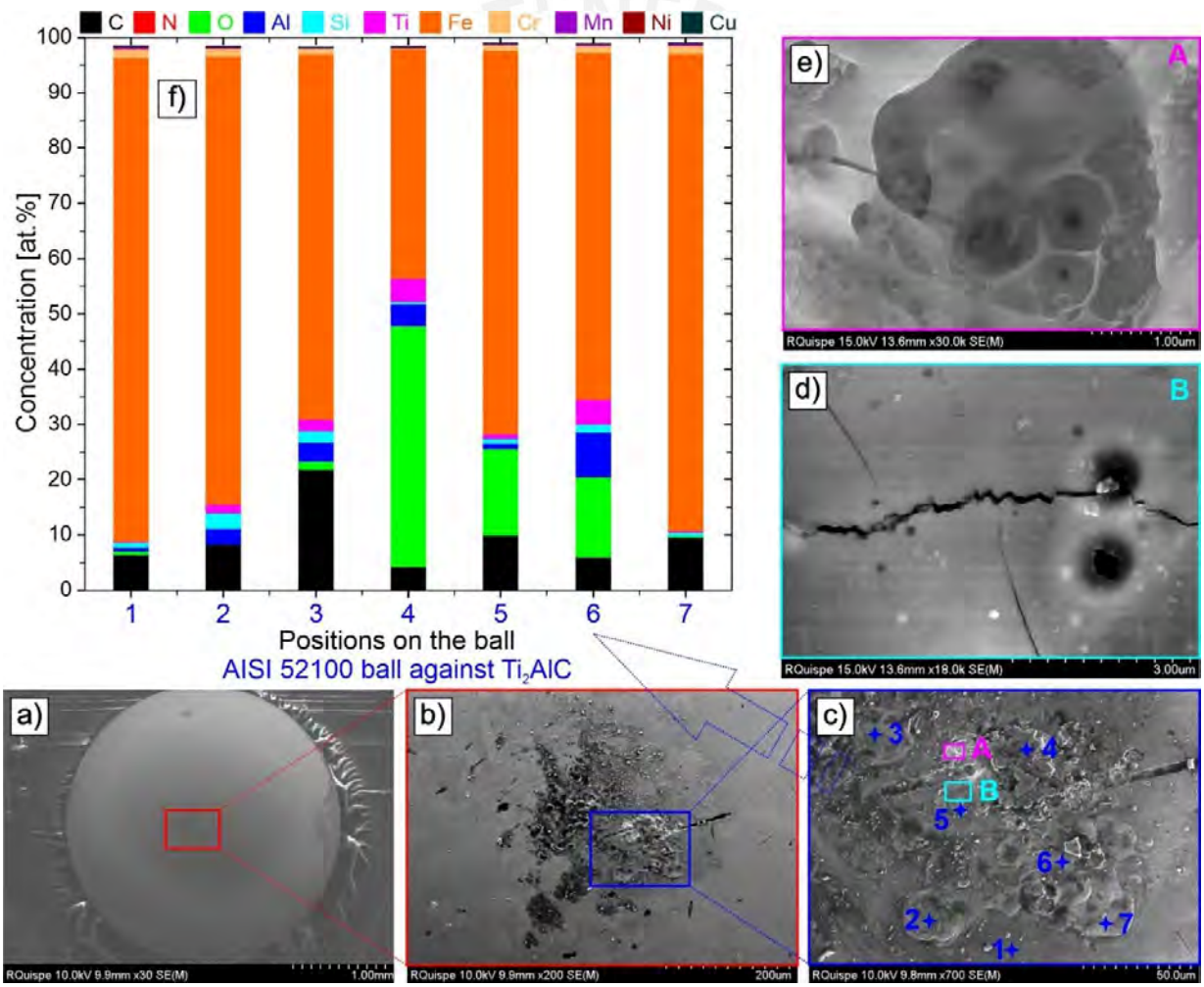


**Figure 6.8** *SEM micrographs and composition of the AISI 52100 ball after the electro-tribological test against $Ti_2AlC$ film at 500 mN and 100 mA. a) ball, b) contact region, c) enlarged of b), d) crack propagation, e) porous, and e) chemical composition of the contact region.*

Figure 6.9 shows SEM micrographs and the composition of the ball after the electro-tribological test of $Ti_3AlC_2$ against 100Cr6 at 500 mN and 100 mA. Figure 6.9a) shows a low-magnification general view of the 100Cr6 ball. Figure 6.9b) shows a magnification of the contact area. The eroded area is considerably more significant than in Figure 6.8b). In addition, the hardness of the $Ti_3AlC_2$ film is lower than that of the $Ti_2AlC$ film. The softer film favors a higher contact area under the same test conditions. Figure 6.9c) shows an enlargement of the eroded area, showing the formation of craters, pores, solidifications, pitting and protuberances resulting from tribological wear and the electric arcs formed during the test. Figure 6.9d) shows an enlarged image of region B of Figure 6.9c). The debris formation can be seen in greater detail. Figure 6.9e) shows an enlarged image of region A of Figure 6.9c). The material removal in the form of circular craters and the erosion caused by the high energies produced by the electric arc are observed. Figure 6.9f) shows the composition of specific points of interest on the eroded surface of the contact area. A higher concentration of Ti, Al and C is observed compared to the composition of Figure 6.8f). It can also observe a high oxygen concentration in all the analyzed points, which suggests the formation of aluminum, titanium and iron oxides; these oxides are a product of the electric arc and the chemical reactions that occurred during the electro-tribological test.

Due to the soft nature of the film, more significant plastic deformation is generated. This greater contact area causes an increase in the CoF and an additional increase in the interface temperature due to the electric current. The formation of insulating oxides on the surface (tribo-film) causes the properties of the tribo-pair to change during the test. This generation of debris and oxides are decisive in changing the ECR, CoF, and the film's subsequent destruction. However, the formation of oxides is not entirely negative since $TiO_2$ and $SiO_2$ improve the wettability of the molten material and suppress spattering, reducing the erosion of the film [215].

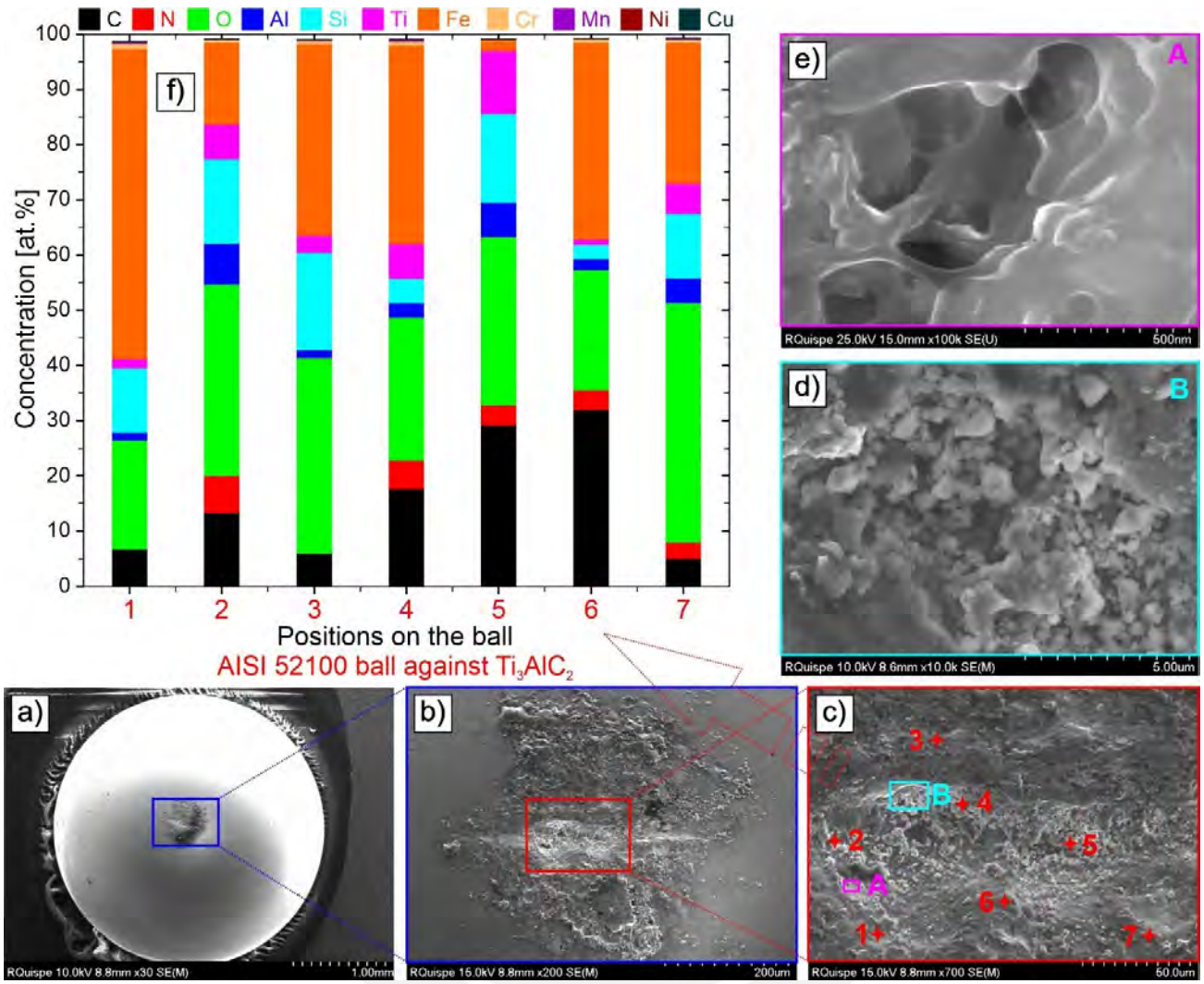


**Figure 6.9** *SEM micrographs and composition of the AISI 52100 ball after the electro-tribological test against $Ti_3AlC_2$ film at 500 mN and 100 mA. a) ball, b) contact region, c) enlarged of b), d) eroded area, e) porous and e) chemical composition of the contact region.*

Figure 6.10a) and b) show that the $Ti_2AlC$ phase compared to the $Ti_3AlC_2$ phase, is less susceptible to the increase in CoF with increasing normal force. This behavior of the $Ti_2AlC$ phase can be attributed to the fact that it is harder, has a smaller grain size and has less surface roughness [30]. The softer phase could generate the formation and accumulation of wear debris on the contact surfaces, causing third-body abrasion. Furthermore, previous results show that the $Ti_2AlC$ thin film has a mixed preferred orientation, while the $Ti_3AlC_2$ phase has a preferred basal orientation. Figure 6.10c) and d) show that a current of 50 mA or more is critical for both phases. However, phase $Ti_2AlC$ experiences a lower increase in ECR compared to phase $Ti_3AlC_2$. The different behavior of CoF and ECR for both phases tested under the same conditions shows that the films' hardness, roughness and electrical properties affect the CoF

and ECR. The variation of the ECR depends on many factors, as mentioned before. However, at low normal loads, the variation of the ECR is higher. This variation of the ECR becomes less noticeable when the normal contact force increases [47].

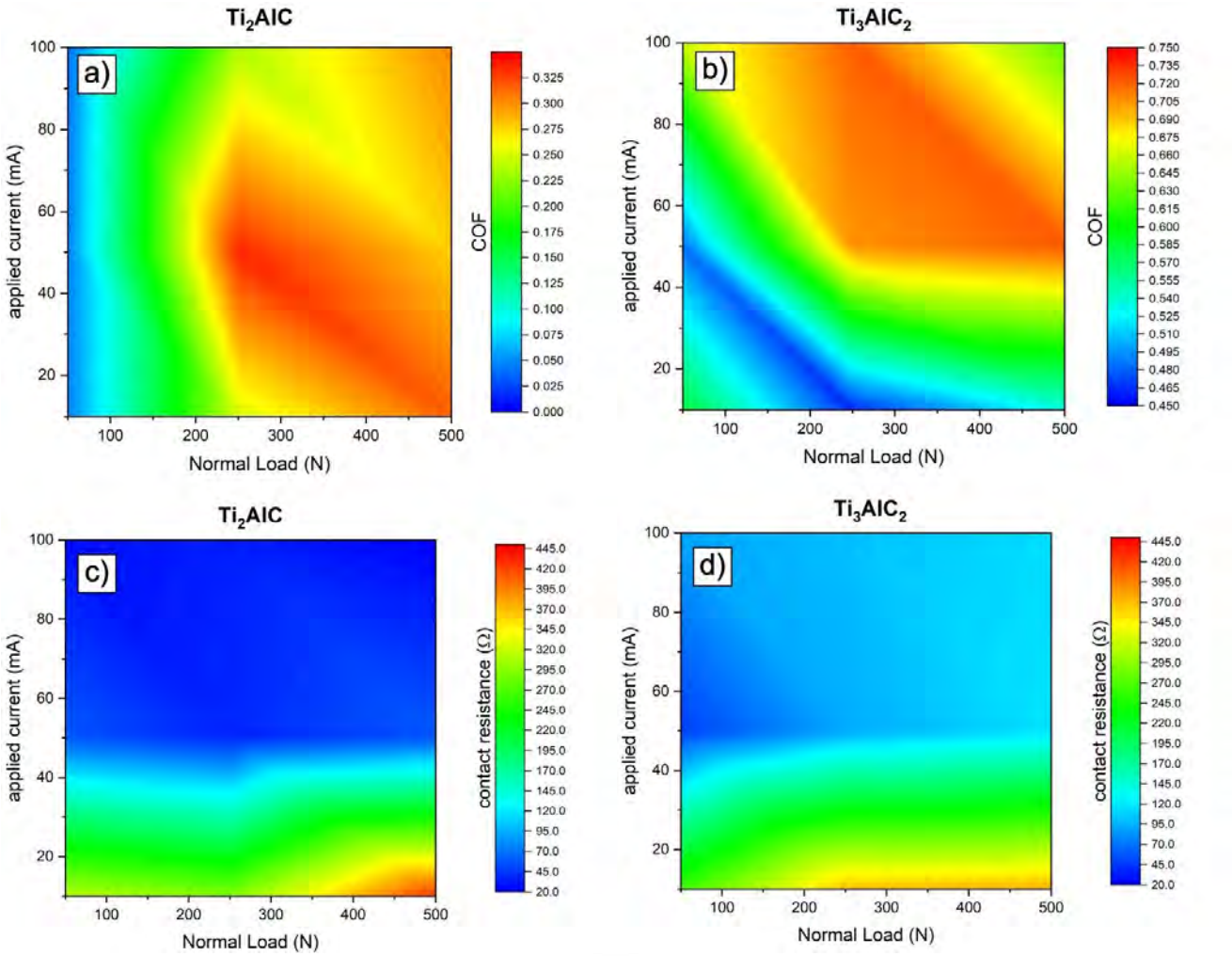


**Figure 6.10** *General summary of CoF for a) $Ti_2AlC$ and b) $Ti_3AlC_2$, and the ECR for a) $Ti_2AlC$ and b) $Ti_3AlC_2$.*

## 6.4 Conclusions

In this chapter, the electrical properties and electro-tribological performance of $Ti_2AlC$ and $Ti_3AlC_2$ films were assessed. The results show that the electro-tribological behavior is influenced by the normal force, the electric current and the tribofilms generated in the dry sliding contact. CoF and ECR were analyzed under forces of 50, 250 and 500 mN and an electrical load of 10, 50 and 100 mA. Local trends of friction coefficient decrease are observed when the contact resistance increases. This could be due to the tribo-films in the track working as electrical insulators. For hard $Ti_2AlC$ film, a force of 50 mN is insufficient to

maintain good electrical contact. This results in a high deviation of the contact resistance value. The contact area is a function of the normal force. However, for the soft $Ti_3AlC_2$ film, a force of 50 mN generates a stable value of contact resistance, which could be due to the significant increase in the contact area for the lower hardness film. An increase in electrical current from 10 to 100 mA for $Ti_2AlC$ causes the contact resistance to decrease considerably. This could be because a higher electrical current increases the temperature at the interface. The contact interface becomes softened by temperature, reflecting an increase in the real contact area.

In contrast, an increase in electric current from 10 to 100 mA for $Ti_3AlC_2$ causes film erosion and arc formation at the contact interface. This could be due to the $Ti_3AlC_2$ phase having a lower hardness than $Ti_2AlC$. Additionally, before the film rupture, the lower resistivity of the $Ti_3AlC_2$ phase and the higher value of CoF help maintain lower ECR values. SEM-EDX analysis of the ball shows internal cavities and an eroded surface due to electric arcs. Furthermore, these results suggest that the increase the contact resistance could be due to the formation of oxides.

# General conclusion and future works

## General conclusion

This thesis investigates the synthesis and structural characterization, mechanical and tribological properties, and the electro-tribological performance of the $Ti_2AlC$ and $Ti_3AlC_2$ thin films. The films were obtained by depositing a Ti-Al-C multilayer system and subsequent annealing in a vacuum and controlled atmosphere of argon and hydrogen. The Ti-Al-C multilayer system was deposited by sputtering on silicon substrates. A double layer of $SiO_2$ and $Si_xN_y$ was used as a diffusion barrier between the film and the substrate. The thicknesses of the individual monolayers controlled the stoichiometry of the film. To obtain a 500 nm thick film, the Ti-Al-C sequence was repeated 22 times with individual thicknesses of 14, 6 and 3.5 nm, respectively. The results of XRD, GD-OES and Raman spectroscopy confirm that the $Ti_2AlC$ phase forms at a temperature of 700°C, while the $Ti_3AlC_2$ phase forms at 950°C. The density determined from the XRD measurements shows that the $Ti_2AlC$ phase (4.02 ± 0.03 g/cm$^3$) is less dense than the $Ti_3AlC_2$ phase (4.26 ± 0.04 g/cm$^3$). This could be because the $Ti_3AlC_2$ phase contains a higher number of atoms contained in its unit cell. The $Ti_2AlC$ thin film has a mixed preferred orientation, while the $Ti_3AlC_2$ phase has a preferred basal orientation. AFM measurements reveal that the average surface roughness ($R_a$) of $Ti_2AlC$ and $Ti_3AlC_2$ is approximately 4 and 12 nm, respectively.

The tribological performance of $Ti_2AlC$ and $Ti_3AlC_2$ films is correlated with hardness, surface roughness, grain size and texture. Nanoindentation tests show that the $Ti_2AlC$ phase (11.6 ± 0.3 GPa) is harder than $Ti_3AlC_2$ (5.3 ± 0.9 GPa). This higher hardness of the $Ti_2AlC$ phase can be attributed to the preferred mixed orientation and smaller grain size compared to the $Ti_3AlC_2$ phase. The $Ti_2AlC$/bearing steel ball system shows a CoF variation between 0.21 and 0.42 in a normal load range of 50 to 500 mN. Meanwhile, the $Ti_3AlC_2$/bearing steel ball system shows CoF values between 0.64 and 0.91 for the same normal load range. Based on the results, the $Ti_2AlC$ phase shows better tribological performance than $Ti_3AlC_2$. This behavior can be attributed to its higher hardness, smaller grain size and lower surface roughness. The SEM-EDX analysis of the worn tracks reveals a material transfer from the ball to the thin film ($Ti_3AlC_2$). This causes an accumulation of debris between the sliding surfaces, which causes a third-body abrasion and, consequently, a higher frictional force and wear.

The electrical properties and electro-tribological performance of $Ti_2AlC$ and $Ti_3AlC_2$ films are investigated. The results show that the electro-tribological performance is influenced by the normal force, the electric current and the tribo-films generated in the sliding contact. The electrical resistivity test shows that the $Ti_2AlC$ phase (0.731 ± 0.002 μΩ·m) has mayor resistivity than $Ti_3AlC_2$ (0.452 ± 0.001 μΩ·m). This could

be attributed to the smaller grain size of the $Ti_2AlC$ phase, which is an obstacle to the movement of electrons. In addition, the CoF and the ECR were evaluated under forces of 50, 250 and 500 mN and an electrical load of 10, 50 and 100 mA. The results show local trends of a decrease in CoF when the electrical contact resistance increases. This could be due to the tribo-films present in the wear track. It is shown that a force of 50 mN on the $Ti_2AlC$ film is insufficient to maintain good electrical contact. This is because the hardness of the phase reduces the real contact area. This resulted in a high deviation of the ECR value. The real contact area is a function of the normal force. In contrast, for the soft $Ti_3AlC_2$ film, a force of 50 mN generates a stable value of the ECR, which could be due to the significant increase in the real contact area since it is a film with less hardness. An increased electrical current from 10 to 100 mA for $Ti_2AlC$ causes the ECR to decrease considerably. This could be because a higher electrical current increases the temperature at the interface, softening the contact surfaces and increasing the real contact area. While an increase in electric current from 10 to 100 mA for $Ti_3AlC_2$ causes film erosion and electric arc formation at the contact interface. SEM-EDX analysis of the ball shows the formation of internal cavities, brittle failure and an eroded surface due to electric arcs. Furthermore, the SEM-EDX results suggest the formation of oxides that would increase the contact resistance. In an electro-tribological sliding contact, the variation of the ECR could be used to control the state of the thin films and the possible formation of tribo-films.

## Future works

As discussed in the theoretical background part, the hardness of thin films is one of the most critical parameters in the tribological study. In this thesis, the films of $Ti_2AlC$ and $Ti_3AlC_2$ were evaluated. These films had different values of hardness. The $Ti_2AlC$ phase is harder than the $Ti_3AlC_2$. A better tribological behavior was observed for the hard phase. In contrast, the $Ti_3AlC_2$ phase evaluated at 10 mA and 10 mN shows a good electro-tribological performance with lower ECR values than the $Ti_2AlC$ phase. This could be attributed to a larger contact area. Bowden and Tabor [110] and others suggest that soft coatings can reduce the coefficient of friction. However, this could cause excessive adhesive wear. On the other hand, a hard coating on a soft substrate can reduce wear by preventing ploughing [216]. Hard films have a good tribological performance in abrasive environments [109]. If the substrate is softer than the film, the hardness of the substrate should be increased to reduce the deflection failure of the coating [13]. Since the hardness of the film influences the tribological behavior, it is proposed to investigate the tribological behavior of both phases with different hardness values. For example, the film's hardness can be modified by changing the grain size and texture.

As previously discussed, the thickness of the thin film influences tribological behavior. The thesis focused on evaluating the mechanical, tribological and electro-tribological properties of the $Ti_2AlC$ and $Ti_3AlC_2$ phases of a single thickness of approximately 500 nm. Coatings are usually used for different purposes, including aesthetics, reducing friction and/or wear, functionalizing the surface, etc. Furthermore, if the substrate is not hard enough to support the film and the applied loads, the film could fail due to deflection [217]. This could be solved by increasing the thickness of the thin film [218]. Based on the previous discussion, it is highlighted that the thickness of the film plays a fundamental role in the mechanical and tribological behavior of films. It is suggested to investigate $Ti_2AlC$ and $Ti_3AlC_2$ films with different thickness values. The thicknesses reported in the literature vary from a few nanometers to micrometers. For example, Su et al. [219] obtained polycrystalline $Ti_2AlC$ films ranging from 150 nm to 400 nm. Furgeaud et al. [220] investigated the fabrication of the $Ti_3SiC_2$ thin films of 100 and 300 nm thick. On the other hand, Garkas et al. [221] fabricated coatings of 6 µm for $Ti_2AlN$ and 2.5 µm for $Ti_2AlC$.

In the present thesis, silicon was used as the substrate on which the multilayers were deposited to subsequently form the MAX phases by annealing heat treatment. In many industries, it is possible to find various applications on various substrates. Reports in the literature show that MAX phases can be successfully obtained on multiple substrates. Go et al. 2018 [222] obtained the $Cr_2AlC$ phase on stainless steel substrates using cold spray technology. Lu et al. [223] obtained a $Ti_3AlC_2$ coating on SS 304 stainless steel substrate by direct current and pulse magnetron sputtering. MAX phases have good electrochemical and electrocatalytic properties [224]. Furthermore, in vitro cytotoxicity studies towards various human cells suggest that the toxicity is almost negligible. Being considered safe and with biocompatible characteristics for future biomedical applications [225]. Given the previous discussion, it is suggested to synthesize the $Ti_2AlC$ and $Ti_3AlC_2$ phases on biocompatible substrates for possible biomedical applications.

Two-dimensional materials known as MXenes have attracted increasing attention in the field of tribology. These materials could be used in solid lubrication due to their low shear stress, as they are similar to graphene [39]. MXenes can form tribo-films resistant to wear and have low friction and self-lubricating capacity [40]. MAX phases can be used as precursors for creating MXenes [7]. In future work, obtaining the MAX phase on different substrates is suggested, subsequently generating the MXenes by chemical selective etching of the A element. The successful formation of MXenes on varied substrates could be a potential candidate for tribological applications.

# Bibliography

[1] P. Eklund, M. Beckers, U. Jansson, H. Högberg, L. Hultman, The Mn+1AXn phases: Materials science and thin-film processing, Thin Solid Films. 518 (2010) 1851–1878. https://doi.org/10.1016/j.tsf.2009.07.184.

[2] Z.M. Sun, Progress in research and development on MAX phases: a family of layered ternary compounds, International Materials Reviews. 56 (2011) 143–166. https://doi.org/10.1179/1743280410Y.0000000001.

[3] C. Dhakal, S. Aryal, R. Sakidja, W.Y. Ching, Approximate lattice thermal conductivity of MAX phases at high temperature, J Eur Ceram Soc. 35 (2015) 3203–3212. https://doi.org/10.1016/j.jeurceramsoc.2015.04.013.

[4] W. Jeitschko, H. Nowotny, F. Benesovsky, Ti2AlN, eine stickstoffhaltige H-Phase, Monatsh Chem. 94 (1963) 1198–1200. https://doi.org/10.1007/BF00905710.

[5] H. Nowotny, Strukturchemie einiger Verbindungen der Übergangsmetalle mit den elementen C, Si, Ge, Sn, Progress in Solid State Chemistry. 5 (1971) 27–70. https://doi.org/10.1016/0079-6786(71)90016-1.

[6] J. Gonzalez-Julian, Processing of MAX phases: From synthesis to applications, Journal of the American Ceramic Society. 104 (2021) 659–690. https://doi.org/10.1111/jace.17544.

[7] M. Naguib, M. Kurtoglu, V. Presser, J. Lu, J. Niu, M. Heon, L. Hultman, Y. Gogotsi, M.W. Barsoum, Two-dimensional nanocrystals produced by exfoliation of Ti3AlC2, Advanced Materials. 23 (2011) 4248–4253. https://doi.org/10.1002/adma.201102306.

[8] R. Grieseler, M.K. Camargo, M. Hopfeld, U. Schmidt, A. Bund, P. Schaaf, Copper-MAX-phase composite coatings obtained by electro-co-deposition: A promising material for electrical contacts, Surf Coat Technol. 321 (2017) 219–228. https://doi.org/10.1016/j.surfcoat.2017.04.060.

[9] Z. Sun, Y. Zhou, M. Li, Oxidation behaviour of Ti3SiC2-based ceramic at 900-1300°C in air, Corros Sci. 43 (2001) 1095–1109. https://doi.org/10.1016/S0010-938X(00)00142-6.

[10] S. Gupta, D. Filimonov, T. Palanisamy, T. El-Raghy, M.W. Barsoum, Ta2AlC and Cr2AlC Ag-based composites-New solid lubricant materials for use over a wide temperature range against Ni-based superalloys and alumina, Wear. 262 (2007) 1479–1489. https://doi.org/10.1016/j.wear.2007.01.028.

[11] K. Holmberg, A. Erdemir, Influence of tribology on global energy consumption, costs and emissions, Friction. 5 (2017) 263–284. https://doi.org/10.1007/s40544-017-0183-5.

[12] A. Erdemir, C. Donnet, Tribology of diamond-like carbon films: Recent progress and future prospects, J Phys D Appl Phys. 39 (2006) 311–327. https://doi.org/10.1088/0022-3727/39/18/R01.

[13] B. Podgornik, J. Vizintin, H. Ronkainen, K. Holmberg, Friction and wear properties of DLC-coated plasma nitrided steel in unidirectional and reciprocating sliding, 2000.

[14] J. Fontaine, C. Donnet, A. Erdemir, Fundamentals of the tribology of DLC coatings, in: Tribology of Diamond-Like Carbon Films: Fundamentals and Applications, 2008: pp. 139–154. https://doi.org/10.1007/978-0-387-49891-1_5.

[15] M. Madej, The effect of TiN and CrN interlayers on the tribological behavior of DLC coatings, Wear. 317 (2014) 179–187. https://doi.org/10.1016/j.wear.2014.05.008.

[16] Microstructure and property evolution of Cr-DLC films with different Cr content deposited by a hybrid beam technique, Vacuum. 85 (2011) 792. http://dx.doi.org/10.1016/j.vacuum.2010.11.013.

[17] T. Polcar, A. Cavaleiro, Review on self-lubricant transition metal dichalcogenide nanocomposite coatings alloyed with carbon, Surf Coat Technol. 206 (2011) 686–695. https://doi.org/10.1016/j.surfcoat.2011.03.004.

[18] H.H. Chien, K.J. Ma, S.V.P. Vattikuti, C.H. Kuo, C.B. Huo, C.L. Chao, Tribological behaviour of MoS2/Au coatings, Thin Solid Films. 518 (2010) 7532–7534. https://doi.org/10.1016/j.tsf.2010.05.040.

[19] T.W. Scharf, P.G. Kotula, S. v. Prasad, Friction and wear mechanisms in MoS2Sb2O 2Au nanocomposite coatings, Acta Mater. 58 (2010) 4100–4109. https://doi.org/10.1016/j.actamat.2010.03.040.

[20] D. Wang, M. Hu, D. Jiang, X. Gao, Y. Fu, J. Sun, L. Weng, Cabbage-like WS2/Ni bilayer thin film for improved tribological property, Surf Coat Technol. 358 (2019) 50–56. https://doi.org/10.1016/j.surfcoat.2018.11.026.

[21] M. Khadem, O. V. Penkov, H.K. Yang, D.E. Kim, Tribology of multilayer coatings for wear reduction: A review, Friction. 5 (2017) 248–262. https://doi.org/10.1007/s40544-017-0181-7.

[22] Y. Liu, M. Gubisch, L. Spiess, J. A. Schaefer, Sliding friction of nanocomposite WC 1-x/C coatings: Transfer film and its influence on tribology, J Nanosci Nanotechnol. 9 (2009) 3499–3505. https://doi.org/10.1166/jnn.2009.NS23.

[23] E. Martinez, J. Romero, A. Lousa, J. Esteve, Wear behavior of nanometric CrN/Cr multilayers, Surf Coat Technol. 163–164 (2003) 571–577. https://doi.org/10.1016/S0257-8972(02)00664-3.

[24] Investigation of multilayered TiSiC/NiC protective coatings, Vacuum. 120 (2015) 60. http://dx.doi.org/10.1016/j.vacuum.2015.06.019.

[25] Arc plasma deposition of TiSiN/Ni nanoscale multilayered coatings, Mater. Chem. Phys. 138 (2013) 500. http://dx.doi.org/10.1016/j.matchemphys.2012.12.010.

[26] J. Rong, J. Wu, J. Tu, X. Yu, J. Feng, Z. Yuan, Improving the mechanical and tribological properties of amorphous carbon-based films by an a-C/Zr/ZrN multilayered interlayer, Ceram Int. 45 (2019) 6950–6958. https://doi.org/10.1016/j.ceramint.2018.12.193.

[27] D. Yonekura, J. Fujita, K. Miki, Fatigue and wear properties of Ti-6Al-4V alloy with Cr/CrN multilayer coating, Surf Coat Technol. 275 (2015) 232–238. https://doi.org/10.1016/j.surfcoat.2015.05.014.

[28] M.A. Al-Bukhaiti, K.A. Al-Hatab, W. Tillmann, F. Hoffmann, T. Sprute, Tribological and mechanical properties of Ti/TiAlN/TiAlCN nanoscale multilayer PVD coatings deposited on AISI H11 hot work tool steel, Appl Surf Sci. 318 (2014) 180–190. https://doi.org/10.1016/j.apsusc.2014.03.026.

[29] S. Gupta, M.W. Barsoum, On the tribology of the MAX phases and their composites during dry sliding: A review, Wear. 271 (2011) 1878–1894. https://doi.org/10.1016/j.wear.2011.01.043.

[30] R. Quispe, C. Torres, L. Eggert, G.A. Ccama, M. Kurniawan, M. Hopfeld, J.L. Zárate, M.K. Camargo, A. Rosenkranz, J.A. Acosta, A. Bund, P. Schaaf, R. Grieseler, Tribological and Mechanical Performance of $Ti_2AlC$ and $Ti_3AlC_2$ Thin Films, Adv Eng Mater. (2022) 2200188. https://doi.org/10.1002/adem.202200188.

[31] J. Gonzalez-Julian, J. Llorente, M. Bram, M. Belmonte, O. Guillon, Novel Cr2AlC MAX-phase/SiC fiber composites: Synthesis, processing and tribological response, J Eur Ceram Soc. 37 (2017) 467–475. https://doi.org/10.1016/j.jeurceramsoc.2016.09.029.

[32] S. Ahmadifard, A. Momeni, S. Bahmanzadeh, S. Kazemi, Microstructure, tribological and mechanical properties of Al7075/Ti3AlC2 MAX-phase surface composite produced by friction stir processing, Vacuum. 155 (2018) 134–141. https://doi.org/10.1016/j.vacuum.2018.06.002.

[33] A. Haddad, N. Chiker, M. Abdi, M.E.A. Benamar, M. Hadji, M.W. Barsoum, Microstructure and tribological properties of boronized Ti2AlC MAX surfaces, Ceram Int. 42 (2016) 16325–16331. https://doi.org/10.1016/j.ceramint.2016.07.189.

[34] S. Gupta, D. Filimonov, T. Palanisamy, M.W. Barsoum, Tribological behavior of select MAX phases against Al2O3 at elevated temperatures, Wear. 265 (2008) 560–565. https://doi.org/10.1016/j.wear.2007.11.018.

[35] A. Loganathan, A. Sahu, C. Rudolf, C. Zhang, S. Rengifo, T. Laha, B. Boesl, A. Agarwal, Multi-scale tribological and nanomechanical behavior of cold sprayed Ti2AlC MAX phase coating, Surf Coat Technol. 334 (2018) 384–393. https://doi.org/10.1016/j.surfcoat.2017.11.067.

[36] S. Gupta, D. Filimonov, V. Zaitsev, T. Palanisamy, M.W. Barsoum, Ambient and 550 °C tribological behavior of select MAX phases against Ni-based superalloys, Wear. 264 (2008) 270–278. https://doi.org/10.1016/j.wear.2007.03.011.

[37] D. Davis, M. Srivastava, M. Malathi, B.B. Panigrahi, S. Singh, Effect of Cr2AlC MAX phase addition on strengthening of Ni-Mo-Al alloy coating on piston ring: Tribological and twist-fatigue life assessment, Appl Surf Sci. 449 (2018) 295–303. https://doi.org/10.1016/j.apsusc.2018.01.146.

[38] A. Rosenkranz, Y. Liu, L. Yang, L. Chen, 2D nano-materials beyond graphene: from synthesis to tribological studies, Appl Nanosci. (2020). https://doi.org/10.1007/s13204-020-01466-z.

[39] B.C. Wyatt, A. Rosenkranz, B. Anasori, 2D MXenes: Tunable Mechanical and Tribological Properties, Advanced Materials. (2021). https://doi.org/10.1002/adma.202007973.

[40] M. Marian, G.C. Song, B. Wang, V.M. Fuenzalida, S. Krauß, B. Merle, S. Tremmel, S. Wartzack, J. Yu, A. Rosenkranz, Effective usage of 2D MXene nanosheets as solid lubricant – Influence of contact pressure and relative humidity, Appl Surf Sci. 531 (2020). https://doi.org/10.1016/j.apsusc.2020.147311.

[41] A. Rosenkranz, P.G. Grützmacher, C. Gachot, H.L. Costa, Surface Texturing in Machine Elements − A Critical Discussion for Rolling and Sliding Contacts, Adv Eng Mater. 1900194 (2019) 1–20. https://doi.org/10.1002/adem.201900194.

[42] A. Rosenkranz, H.L. Costa, M.Z. Baykara, A. Martini, Synergetic effects of surface texturing and solid lubricants to tailor friction and wear – A review, Tribol Int. 155 (2021) 106792. https://doi.org/10.1016/j.triboint.2020.106792.

[43] D. Gropper, L. Wang, T.J. Harvey, Hydrodynamic lubrication of textured surfaces: A review of modeling techniques and key findings, Tribol Int. 94 (2016) 509–529. https://doi.org/10.1016/j.triboint.2015.10.009.

[44] A. Kovalchenko, O. Ajayi, A. Erdemir, G. Fenske, I. Etsion, The effect of laser surface texturing on transitions in lubrication regimes during unidirectional sliding contact, Tribol Int. 38 (2005) 219–225. https://doi.org/10.1016/j.triboint.2004.08.004.

[45] B. Mao, A. Siddaiah, Y. Liao, P.L. Menezes, Laser surface texturing and related techniques for enhancing tribological performance of engineering materials: A review, J Manuf Process. 53 (2020) 153–173. https://doi.org/10.1016/j.jmapro.2020.02.009.

[46] A. Rosenkranz, H.L. Costa, F. Profito, C. Gachot, S. Medina, D. Dini, Influence of surface texturing on hydrodynamic friction in plane converging bearings - An experimental and numerical approach, Tribol Int. 134 (2019) 190–204. https://doi.org/10.1016/j.triboint.2019.01.042.

[47] K.E. Trinh, E. Ramos-Moore, I. Green, C. Pauly, M. Zamanzade, F. Mucklich, Topographical and Microstructural Effects of Laser Surface Texturing on Tin-Coated Copper Electrical Connectors under Load Cycling, IEEE Trans Compon Packaging Manuf Technol. 7 (2017) 582–590. https://doi.org/10.1109/TCPMT.2017.2659224.

[48] X.H. Wang, Y.C. Zhou, Layered Machinable and Electrically Conductive Ti2AlC and Ti3AlC2 Ceramics: a Review, J Mater Sci Technol. 26 (2010) 385–416. https://doi.org/10.1016/s1005-0302(10)60064-3.

[49] Y. Bai, X. He, C. Zhu, G. Chen, Microstructures, electrical, thermal, and mechanical properties of bulk Ti2AlC synthesized by self-propagating high-temperature combustion synthesis with pseudo hot isostatic pressing, Journal of the American Ceramic Society. 95 (2012) 358–364. https://doi.org/10.1111/j.1551-2916.2011.04934.x.

[50] J. Ding, W.B. Tian, P. Zhang, M. Zhang, Y.M. Zhang, Z.M. Sun, Arc erosion behavior of Ag/Ti3AlC2 electrical contact materials, J Alloys Compd. 740 (2018) 669–676. https://doi.org/10.1016/j.jallcom.2018.01.015.

[51] H. Zhao, Y. Feng, Z. Zhou, G. Qian, J. Zhang, X. Huang, X. Zhang, Effect of electrical current density, apparent contact pressure, and sliding velocity on the electrical sliding wear behavior of Cu–Ti3AlC2 composites, Wear. 444–445 (2020) 203156. https://doi.org/10.1016/j.wear.2019.203156.

[52] W. Tian, P. Wang, G. Zhang, Y. Kan, Y. Li, D. Yan, Synthesis and thermal and electrical properties of bulk Cr2AlC, Scr Mater. 54 (2006) 841–846. https://doi.org/10.1016/j.scriptamat.2005.11.009.

[53] M.W. Barsoum, I. Salama, T. El-Raghy, J. Golczewski, W.D. Porter, H. Wang, H.J. Seifert, F. Aldinger, Thermal and electrical properties of Nb2AlC, (Ti, Nb)2AlC and Ti2AlC, Metall Mater Trans A Phys Metall Mater Sci. 33 (2002) 2775–2779. https://doi.org/10.1007/s11661-002-0262-7.

[54] M.W. Barsoum, H. Yoo, I.K. Polushina, V.Y. Rud, Y. v Rud, T. El-Raghy, Electrical conductivity, thermopower, and Hall effect of Ti3AlC2,Ti4AlN3, and Ti3SiC2, Phys Rev B. 62 (2000) 194–198. https://doi.org/10.1103/PhysRevB.62.10194.

[55] J. Lauridsen, J. Lu, P. Eklund, L. Hultman, Å. Öberg, M. Lindgren, L. Fast, E. Lewin, U. Jansson, Deposition of Ti-Si-C-Ag nanocomposite coatings as electrical contact material, Electrical Contacts, Proceedings of the Annual Holm Conference on Electrical Contacts. (2010) 288–294. https://doi.org/10.1109/HOLM.2010.5619528.

[56] P. Eklund, J. Emmerlich, H. Högberg, P.O.A. Persson, L. Hultman, O. Wilhelmsson, U. Jansson, P. Isberg, Synthesis and characterization of Ti-Si-C compounds for electrical contact applications, Electrical Contacts, Proceedings of the Annual Holm Conference on Electrical Contacts. 2005 (2005) 277–283. https://doi.org/10.1109/HOLM.2005.1518257.

[57] P. Wang, B. Mei, H. Xiao-lin, Z. Wei-bing, Synthesis of Ti2AlC by hot pressing and its mechanical and electrical properties, Transactions of Nonferrous Metals Society of China. 17 (2007) 1001–1004.

[58] D.D. Wang, W.B. Tian, A. bin Ma, J.X. Ding, C.S. Wang, Y.Y. You, P.G. Zhang, J. Chen, Y.M. Zhang, Z.M. Sun, Anisotropic properties of Ag/Ti3AlC2 electrical contact materials prepared by equal channel angular pressing, J Alloys Compd. 784 (2019) 431–438. https://doi.org/10.1016/j.jallcom.2019.01.083.

[59] H. Zhao, Y. Feng, G. Qian, X. Huang, S. Guo, X. Sun, Effect of Ti3AlC2 Content on Electrical Friction and Wear Behaviors of Cu–Ti3AlC2 Composites, Tribol Lett. 67 (2019). https://doi.org/10.1007/s11249-019-1211-6.

[60] M. Antler, Tribology of metal coatings for electrical contacts, Thin Solid Films. 84 (1981) 245–256. https://doi.org/10.1016/0040-6090(81)90022-5.

[61] N.K. Myshkin, Tribological problems in electrical contacts, Tribol Int. 24 (1991) 45–49. https://doi.org/10.1016/0301-679X(91)90062-E.

[62] D.D. Wang, W.B. Tian, C.J. Lu, J.X. Ding, Y.F. Zhu, M. Zhang, P.G. Zhang, Z.M. Sun, Comparison of the interfacial reactions and properties between Ag/Ti3AlC2 and Ag/Ti3SiC2 electrical contact materials, J Alloys Compd. 857 (2021) 157588. https://doi.org/10.1016/j.jallcom.2020.157588.

[63] X. Zhang, Y. Zhang, B. Tian, J. An, Z. Zhao, A.A. Volinsky, Y. Liu, K. Song, Arc erosion behavior of the Al2O3-Cu/(W, Cr) electrical contacts, Compos B Eng. 160 (2019) 110–118. https://doi.org/10.1016/j.compositesb.2018.10.040.

[64] H. Fashandi, M. Dahlqvist, J. Lu, J. Palisaitis, S.I. Simak, I.A. Abrikosov, J. Rosen, L. Hultman, M. Andersson, A. Lloyd Spetz, P. Eklund, Synthesis of Ti3AuC2 , Ti3AuC2 and Ti3IrC2 by noble metal substitution reaction in Ti3SiC2 for high-temperature-stable Ohmic contacts to SiC, Nat Mater. 16 (2017) 814–818. https://doi.org/10.1038/nmat4896.

[65] M. Braunovic, V. v. Konchits, N.K. Myshkin, Electrical Contacts Fundamentals, Applications and Technology, 2006.

[66] P. Liu, S. Bahadur, J.D. Verhoeven, Electrical Sliding Friction And Wear Behavior Of Cu-Nb In Situ Composites, IEEE Transactions on Components Packaging and Manufacturing Technology Part A. 17 (1994) 616–624. https://doi.org/10.1109/95.335042.

[67] A. Senouci, H. Zaidi, J. Frene, A. Bouchoucha, D. Paulmier, Damage of surfaces in sliding electrical contact copper/steel, Appl Surf Sci. 144–145 (1999) 287–291. https://doi.org/10.1016/S0169-4332(98)00915-5.

[68] P. Zhang, Y.Y. Lau, Scaling laws for electrical contact resistance with dissimilar materials, J Appl Phys. 108 (2010) 1–10. https://doi.org/10.1063/1.3457899.

[69] H. Prashad, Tribology in Electrical Environments, 2005.

[70] T.H. Gilani, D. Rabchuk, Electrical Resistivity of Gold Thin Film, Can J Phys. 96 (2018) 272–274.

[71] A. Senouci, J. Frene, H. Zaidi, Wear mechanism in graphite-copper electrical sliding contact, Wear. 225–229 (1999) 949–953. https://doi.org/10.1016/S0043-1648(98)00412-8.

[72] M. Antler, Sliding Wear of Metallic Contacts, IEEE Transactions on Components, Hybrids, and Manufacturing Technology. 4 (1981) 15–29. https://doi.org/10.1109/TCHMT.1981.1135784.

[73] Z.K. Chen, Wear and Contamination of Electroplated Gold Films in Line Contact, IEEE Transactions on Components, Hybrids, and Manufacturing Technology. 15 (1992) 378–385. https://doi.org/10.1109/33.148506.

[74] T. Ding, G.X. Chen, X. Wang, M.H. Zhu, W.H. Zhang, W.X. Zhou, Friction and wear behavior of pure carbon strip sliding against copper contact wire under AC passage at high speeds, Tribol Int. 44 (2011) 437–444. https://doi.org/10.1016/j.triboint.2010.11.022.

[75] T. Ding, G.X. Chen, Y.M. Li, H.J. Yang, Q.D. He, Arc erosive characteristics of a carbon strip sliding against a copper contact wire in a high-speed electrified railway, Tribol Int. 79 (2014) 8–15. https://doi.org/10.1016/j.triboint.2014.05.003.

[76] S.G. Jia, P. Liu, F.Z. Ren, B.H. Tian, M.S. Zheng, G.S. Zhou, Sliding wear behavior of copper alloy contact wire against copper-based strip for high-speed electrified railways, Wear. 262 (2007) 772–777. https://doi.org/10.1016/j.wear.2006.08.020.

[77] G. Mei, Impact of voltage on the electric sliding tribological properties of current collectors against overhead lines, Wear. 474–475 (2021) 203868. https://doi.org/10.1016/j.wear.2021.203868.

[78] M.W. Barsoum, The Mn+1AXn Phases: A New Class of Solids; Thermodynamically Stable Nanolaminates, Prog. Solid St. Chem. 28 (2000) 201–281. https://doi.org/10.1016/S0079-6786(00)00006-6.

[79] M. Sokol, V. Natu, S. Kota, M.W. Barsoum, On the Chemical Diversity of the MAX Phases, Trends Chem. 1 (2019) 210–223. https://doi.org/10.1016/j.trechm.2019.02.016.

[80] O. Berger, The correlation between structure, multifunctional properties and applications of PVD MAX phase coatings. Part II. Texture and high-temperature properties, Surface Engineering. 36 (2020) 268–302. https://doi.org/10.1080/02670844.2019.1611076.

[81] M. Magnuson, M. Mattesini, Chemical bonding and electronic-structure in MAX phases as viewed by X-ray spectroscopy and density functional theory, Thin Solid Films. 621 (2017) 108–130. https://doi.org/10.1016/j.tsf.2016.11.005.

[82] M.W. Barsoum, The Mn+1AXn Phases and their Properties, 2010.

[83] M. Radovic, M.W. Barsoum, MAX phases: Bridging the gap between metals and ceramics, American Ceramic Society Bulletin. 92 (2013) 20–27. www.ceramics.org.

[84] H. Chen, Y. Du, D. Wang, C. Zhang, G. Yang, B. Liu, Y. Gao, S. Shi, TiC/Ti3AlC2–Co plasma-sprayed coatings with excellent high-temperature tribological properties, Ceram Int. 44 (2018) 22520–22528. https://doi.org/10.1016/j.ceramint.2018.09.023.

[85] G.P. Bei, V. Gauthier-Brunet, C. Tromas, S. Dubois, Synthesis, characterization, and intrinsic hardness of layered nanolaminate Ti3AlC2 and Ti3Al0.8Sn0.2C2 solid solution, Journal of the American Ceramic Society. 95 (2012) 102–107. https://doi.org/10.1111/j.1551-2916.2011.04846.x.

[86] J. Lyu, E.B. Kashkarov, N. Travitzky, M.S. Syrtanov, A.M. Lider, Sintering of MAX-phase materials by spark plasma and other methods, J Mater Sci. 56 (2021) 1980–2015. https://doi.org/10.1007/s10853-020-05359-y.

[87] Y. Mizuno, K. Sato, M. Mrinalini, T.S. Suzuki, Y. Sakka, Fabrication of textured Ti3AlC2 by spark plasma sintering and their anisotropic mechanical properties, Journal of the Ceramic Society of Japan. 121 (2013) 366–369. https://doi.org/10.2109/jcersj2.121.366.

[88] C. Hu, Y. Sakka, S. Grasso, T. Suzuki, H. Tanaka, Tailoring Ti3SiC2 ceramic via a strong magnetic field alignment method followed by spark plasma sintering, Journal of the American Ceramic Society. 94 (2011) 742–748. https://doi.org/10.1111/j.1551-2916.2010.04186.x.

[89] J.P. Siebert, L. Bischoff, M. Lepple, A. Zintler, L. Molina-Luna, U. Wiedwald, C.S. Birkel, Sol-gel based synthesis and enhanced processability of MAX phase Cr2GaC, J Mater Chem C Mater. 7 (2019) 6034–6040. https://doi.org/10.1039/c9tc01416k.

[90] Q.T.H. Ta, N.M. Tran, J.S. Noh, Pressureless manufacturing of Cr2AlC compound and the temperature effect, Materials and Manufacturing Processes. 36 (2021) 200–208. https://doi.org/10.1080/10426914.2020.1819547.

[91] C. Racault, F. Langlais, R. Naslain, Y. Kihn, On the chemical vapour deposition of Ti3SiC2 from TiCl4-SiCl4-CH4-H2 gas mixtures - Part II An experimental approach, J Mater Sci. 29 (1994) 3941–3948. https://doi.org/10.1007/BF00355952.

[92] M. Stevens, H. Pazniak, A. Jemiola, M. Felek, M. Farle, U. Wiedwald, Pulsed laser deposition of epitaxial Cr2AlC MAX phase thin films on MgO(111) and Al2O3(0001), Mater Res Lett. 9 (2021) 343–349. https://doi.org/10.1080/21663831.2021.1920510.

[93] J.N. C. Furgeaud, F. Brenet, Multi-scale study of Ti3SiC2 thin film growth mechanisms obtained by magnetron sputtering, Acta Mater. (2019) 163–170. https://doi.org/10.1016/j.mtla.2019.100369.

[94] H. Högberg, L. Hultman, J. Emmerlich, T. Joelsson, P. Eklund, J.M. Molina-Aldareguia, J.P. Palmquist, O. Wilhelmsson, U. Jansson, Growth and characterization of MAX-phase thin films, Surf Coat Technol. 193 (2005) 6–10. https://doi.org/10.1016/j.surfcoat.2004.08.174.

[95] J. Haemers, R. Gusmão, Z. Sofer, Synthesis Protocols of the Most Common Layered Carbide and Nitride MAX Phases, Small Methods. 1900780 (2020) 1–32. https://doi.org/10.1002/smtd.201900780.

[96] M.W. Qureshi, X. Ma, G. Tang, B. Miao, J. Niu, Fabrication and mechanical properties of Cr2AlC max phase coatings on TiBw/ti6Al4V composite prepared by hipims, Materials. 14 (2021) 1–22. https://doi.org/10.3390/ma14040826.

[97] S.N. Perevislov, T. v. Sokolova, V.L. Stolyarova, The Ti3SiC2 max phases as promising materials for high temperature applications: Formation under various synthesis conditions, Mater Chem Phys. 267 (2021). https://doi.org/10.1016/j.matchemphys.2021.124625.

[98] L. Yong-Ming, P. Wei, L. Shuqin, C. Jian, Synthesis and mechanical properties of in-situ hot-pressed Ti3SiC2 polycrystals, Ceram Int. 28 (2002) 227–230. https://doi.org/10.1016/S0272-8842(01)00083-9.

[99] D.A. Hardwick, The mechanical of thin films: A review, Thin Solid Films. 154 (1987) 109–124.

[100] R.D. Gould, S. Kasap, A.K. Ray, Thin Films, in: Springer Handbook of Electronic and Photonic Materials, 2017: pp. 645–706. https://doi.org/10.1007/978-3-319-48933-9.

[101] R.P. Vinci, J.J. Vlassak, Mechanical behavior of thin films, Annual Review of Materials Science. 26 (1996) 431–462.

[102] H.J. Frost, DEFORMATION MECHANISMS IN THIN FILMS, 265 (1992).

[103] B. Bhushan, Introduction to Tribology, 2013. https://doi.org/10.1201/9780429448867-1.

[104] P.L. Menezes, S.P. Ingole, M. Nosonovsky, S. v. Kailas, M.R. Lovell, Tribology for Scientists and Engineers, 2013. https://doi.org/10.1007/978-1-4614-1945-7.

[105] W. Shizhu, H. Ping, Principles of Tribology, 2012. https://doi.org/10.1115/1.3453090.

[106] J.F. Archard, Contact and rubbing of flat surfaces, J Appl Phys. 24 (1953) 981–988. https://doi.org/10.1063/1.1721448.

[107] I.M. Hutchings, P. Shipway, Tribology: Friction and Wear of Engineering Materials, 2017.

[108] K. Holmberg, A. Matthews, H. Ronkainen, Coatings tribology-contact mechanisms and surface design, 1998.

[109] B. Podgornik, J.$ Ze, V.$ Zintin, Tribology of thin films and their use in the field of machine elements, 2003.

[110] F.P. Bowden, D. Tabor, Friction, lubrication and wear: A survey of work during the last decade, British Journal of Applied Physics. 17 (1966) 1521–1544. https://doi.org/10.1088/0508-3443/17/12/301.

[111] K. Holmberg, A. Matthews, Tribology of Coatings, in: Tribology Series, 1994: pp. 33–124. https://doi.org/10.1016/S0167-8922(08)70753-3.

[112] C. Donnet, A. Erdemir, Tribology of Diamond-Like Carbon Films: Fundamentals and Applications, 2008. https://doi.org/10.1007/978-0-387-49891-1.

[113] H. Pelletier, J. Krier, P. Mille, Characterization of mechanical properties of thin films using nanoindentation test, Mechanics of Materials. 38 (2006) 1182–1198. https://doi.org/10.1016/j.mechmat.2006.02.011.

[114] M. Hopfeld, R. Grieseler, A. Vogel, H. Romanus, P. Schaaf, Tribological behavior of selected Mn+1AXn phase thin films on silicon substrates, Surf Coat Technol. 257 (2014) 286–294. https://doi.org/10.1016/j.surfcoat.2014.08.034.

[115] J. Emmerlich, G. Gassner, P. Eklund, H. Högberg, L. Hultman, Micro and macroscale tribological behavior of epitaxial Ti3SiC2 thin films, Wear. 264 (2008) 914–919. https://doi.org/10.1016/j.wear.2007.06.013.

[116] S. Wang, J. Cheng, S. Zhu, Z. Qiao, J. Yang, Low friction properties of Ti3AlC2/SiC tribo-pair in sea water environment, Tribol Int. 103 (2016) 228–235. https://doi.org/10.1016/j.triboint.2016.06.045.

[117] S. Wang, J. Cheng, S. Zhu, Z. Qiao, J. Yang, W. Liu, Frictional properties of Ti3AlC2 ceramic against different counterparts in deionized water and artificial seawater, Ceram Int. 42 (2016) 4578–4585. https://doi.org/10.1016/j.ceramint.2015.11.153.

[118] S. Wang, J. Ma, S. Zhu, J. Cheng, Z. Qiao, J. Yang, W. Liu, High temperature tribological properties of Ti3AlC2 ceramic against SiC under different atmospheres, Mater Des. 67 (2015) 188–196. https://doi.org/10.1016/j.matdes.2014.11.043.

[119] Y. Hibi, K. Miyake, T. Murakami, S. Sasaki, Tribological behavior of SiC-reinforced Ti3SiC2-based composites under dry condition and under lubricated condition with water and ethanol, Journal of the American Ceramic Society. 89 (2006) 2983–2985. https://doi.org/10.1111/j.1551-2916.2006.01173.x.

[120] S. Ren, J. Meng, J. Wang, J. Lu, S. Yang, Tribocorrosion behavior of Ti3SiC2 in the dilute and concentrated sulfuric acid solutions, Wear. 269 (2010) 50–59. https://doi.org/10.1016/j.wear.2010.03.007.

[121] Y. Zhu, A. Zhou, Y. Ji, J. Jia, L. Wang, B. Wu, Q. Zan, Tribological properties of Ti3SiC2coupled with different counterfaces, Ceram Int. 41 (2015) 6950–6955. https://doi.org/10.1016/j.ceramint.2015.01.150.

[122] S. Myhra, J.W.B. Summers, E.H. Kisi, Ti3SiC2 - A layered ceramic exhibiting ultra-low friction, Mater Lett. 39 (1999) 6–11. https://doi.org/10.1016/S0167-577X(98)00206-7.

[123] F. Jiang, S.F. Ren, J.H. Meng, J.J. Lu, High Temperature Wear of Ti3AlC2 Sliding against Al2O3, Adv Mat Res. 177 (2011) 118–120. https://doi.org/10.4028/www.scientific.net/AMR.177.118.

[124] L. Cai, Z. Huang, W. Hu, S. Hao, H. Zhai, Y. Zhou, Fabrication, mechanical properties, and tribological behaviors of Ti2AlC and Ti2AlSn0.2C solid solutions, Journal of Advanced Ceramics. 6 (2017) 90–99. https://doi.org/10.1007/s40145-017-0221-9.

[125] L. Cai, Z. Huang, W. Hu, C. Lei, H. Zhai, Y. Zhou, Dry sliding behaviors and friction surface characterization of Ti3Al0.8Si0.2Sn0.2C2 solid solution against S45C steel, Ceram Int. 45 (2019) 2103–2110. https://doi.org/10.1016/j.ceramint.2018.10.115.

[126] Z. Sun, Y. Zhou, S. Li, Tribological Behavior of Ti3SiC2-based Material, Journal of Materials Sciences and Technology. 18 (2002) 142–145. http://www.jmst.org/EN/abstract/article_7114.shtml.

[127] Y. Zhang, G.P. Ding, Y.C. Zhou, B.C. Cai, Ti3SiC2- A self-lubricating ceramic, Mater Lett. 55 (2002) 285–289. https://doi.org/10.1016/S0167-577X(02)00379-8.

[128] A. Souchet, J. Fontaine, M. Belin, T. Le Mogne, J.L. Loubet, M.W. Barsoum, Tribological duality of Ti3SiC2, Tribol Lett. 18 (2005) 341–352. https://doi.org/10.1007/s11249-004-2761-8.

[129] D. Sarkar, B. Basu, S.J. Cho, M.C. Chu, S.S. Hwang, S.W. Park, Tribological properties of Ti3SiC2, Journal of the American Ceramic Society. 88 (2005) 3245–3248. https://doi.org/10.1111/j.1551-2916.2005.00569.x.

[130] D. Sarkar, B.V.M. Kumar, B. Basu, Understanding the fretting wear of Ti3SiC2, J Eur Ceram Soc. 26 (2006) 2441–2452. https://doi.org/10.1016/j.jeurceramsoc.2005.05.006.

[131] H. Zhai, Z. Huang, M. Ai, Tribological behaviors of bulk Ti3SiC2 and influences of TiC impurities, Materials Science and Engineering A. 435–436 (2006) 360–370. https://doi.org/10.1016/j.msea.2006.07.056.

[132] Z. Huang, H. Zhai, M. Guan, X. Liu, M. Ai, Y. Zhou, Oxide-film-dependent tribological behaviors of Ti3SiC2, Wear. 262 (2007) 1079–1085. https://doi.org/10.1016/j.wear.2006.11.003.

[133] J. Ma, F. Li, L. Fu, S. Zhu, Z. Qiao, J. Yang, W. Liu, Effect of counterface on the tribological behavior of Ti3AlC2 at ambient, Tribol Lett. 53 (2014) 311–317. https://doi.org/10.1007/s11249-013-0269-9.

[134] W. Hai, J. Zeng, S. Ren, J. Meng, J. Lu, Tribological behavior of self-mated Ti3SiC2 in Short-Chain n-Alcohols, glycol and glycerol under boundary lubrication, Tribol Lett. 55 (2014) 421–428. https://doi.org/10.1007/s11249-014-0374-4.

[135] L. Xu, D. Zhu, S. Grasso, T.S. Suzuki, A. Kasara, M. Tosa, B. Kim, Y. Sakka, M. Zhu, C. Hu, Effect of texture microstructure on tribological properties of tailored Ti3AlC2 ceramic, Journal of Advanced Ceramics. 6 (2017) 120–128. https://doi.org/10.1007/s40145-017-0224-6.

[136] T. El-Raghy, P. Blau, M.W. Barsoum, Effect of grain size on friction and wear behavior of Ti3SiC2, Wear. 238 (2000) 125–130.

[137] X. Shi, W. Zhai, M. Peng, Z. Zhu, M. Wang, Z. Xu, J. Yao, S. Song, A. Qamar Ud Din, Synthesis and tribological behaviors of Ti3SiC2 material prepared by vacuum sintering technique, Journal Wuhan University of Technology, Materials Science Edition. 28 (2013) 417–424. https://doi.org/10.1007/s11595-013-0706-5.

[138] Z.Y. Huang, H.X. Zhai, Y. Zhou, Y.F. Wang, Z.L. Zhang, Sliding Friction Behavior of Bulk Ti3SiC2 under Difference Normal Pressures, Key Eng Mater. 280–283 (2005) 1353–1356. https://doi.org/10.4028/www.scientific.net/KEM.280-283.1353.

[139] J. Ma, F. Li, J. Cheng, L. Fu, Z. Qiao, W. Liu, J. Yang, Tribological Behavior of Ti3AlC2 Against SiC at Ambient and Elevated Temperatures, Tribol Lett. 50 (2013) 323–330. https://doi.org/10.1007/s11249-013-0126-x.

[140] W. Hai, S. Ren, J. Meng, J. Lu, Tribo-oxidation of self-mated Ti3SiC2 at elevated temperatures and low speed, Tribol Lett. 48 (2012) 425–432. https://doi.org/10.1007/s11249-012-0036-3.

[141] S. Ren, J. Meng, J. Lu, S. Yang, Tribological behavior of Ti 3SiC 2 sliding against Ni-based alloys at elevated temperatures, Tribol Lett. 31 (2008) 129–137. https://doi.org/10.1007/s11249-008-9345-y.

[142] W. Dang, S. Ren, J. Zhou, Y. Yu, L. Wang, The tribological properties of Ti3SiC2/Cu/Al/SiC composite at elevated temperatures, Tribol Int. 104 (2016) 294–302. https://doi.org/10.1016/j.triboint.2016.09.008.

[143] W. Dang, S. Ren, J. Zhou, Y. Yu, Z. Li, L. Wang, Influence of Cu on the mechanical and tribological properties of Ti3SiC2, Ceram Int. 42 (2016) 9972–9980. https://doi.org/10.1016/j.ceramint.2016.03.099.

[144] Z. Xu, B. Xue, X. Shi, Q. Zhang, W. Zhai, J. Yao, Y. Wang, Sliding Speed and Load Dependence of Tribological Properties of Ti3SiC2/TiAl Composite, Tribology Transactions. 58 (2015) 87–96. https://doi.org/10.1080/10402004.2014.951748.

[145] Z. Huang, H. Xu, H. Zhai, Y. Wang, Y. Zhou, Strengthening and tribological surface self-adaptability of Ti3AlC2by incorporation of Sn to form Ti3Al(Sn)C2 solid solutions, Ceram Int. 41 (2015) 3701–3709. https://doi.org/10.1016/j.ceramint.2014.11.042.

[146] L. Wu, J. xin Chen, M. yue Liu, Y. wang Bao, Y. chun Zhou, Reciprocating friction and wear behavior of Ti3AlC2 and Ti3AlC2/Al2O3 composites against AISI52100 bearing steel, Wear. 266 (2009) 158–166. https://doi.org/10.1016/j.wear.2008.06.009.

[147] C. Hu, Y. Zhou, Y. Bao, D. Wan, Tribological properties of polycrystalline Ti3SiC2 and Al2O3-reinforced Ti3SiC2 composites, Journal of the American Ceramic Society. 89 (2006) 3456–3461. https://doi.org/10.1111/j.1551-2916.2006.01253.x.

[148] J. Yang, W. Gu, L.M. Pan, K. Song, X. Chen, T. Qiu, Friction and wear properties of in situ (TiB2+TiC)/Ti3SiC2 composites, Wear. 271 (2011) 2940–2946. https://doi.org/10.1016/j.wear.2011.06.017.

[149] X. Shi, M. Wang, W. Zhai, Z. Zhu, Z. Xu, Q. Zhang, S. Song, J. Yao, A.Q. ud Din, Friction and wear behavior of NiAl-10wt%Ti3SiC2 composites, Wear. 303 (2013) 9–20. https://doi.org/10.1016/j.wear.2013.02.013.

[150] T. Sun, Q. Wang, D.L. Sun, G.H. Wu, Y. Na, Study on dry sliding friction and wear properties of Ti2AlN/TiAl composite, Wear. 268 (2010) 693–699. https://doi.org/10.1016/j.wear.2009.11.007.

[151] R. Zhang, K. Feng, J. Meng, F. Liu, S. Ren, W. Hai, A. Zhang, Tribological behavior of Ti3SiC2 and Ti3SiC2/Pb composites sliding against Ni-based alloys at elevated temperatures, Ceram Int. 42 (2016) 7107–7117. https://doi.org/10.1016/j.ceramint.2016.01.099.

[152] J. Cao, Z. Yin, H. Li, G. Gao, X. Zhang, Tribological and mechanical properties of Ti2AlC coating at room temperature and 800°C, Ceram Int. 44 (2018) 1046–1051. https://doi.org/10.1016/j.ceramint.2017.10.045.

[153] M. Zhou, W. Lu, X. Liu, W. Zhai, P. Zhang, G. Zhang, Fretting wear properties of plasma-sprayed Ti3SiC2coatings with oxidative crack-healing feature, Tribol Int. 118 (2018) 196–207. https://doi.org/10.1016/j.triboint.2017.10.009.

[154] Q. Gao, J.L. Li, Y.W. Ye, X. Jiang, Y. Wang, J.M. Hu, Tribological behaviors of TiSiC coating in seawater environment, Mater Res Express. 4 (2017). https://doi.org/10.1088/2053-1591/aa5233.

[155] Q.D. Xiao, S. Wu, Tribological behaviours of Ti3 SiC2 under current carrying conditions, Advances in Applied Ceramics. 113 (2014) 381–388. https://doi.org/10.1179/1743676114Y.0000000193.

[156] Z. Huang, H. Zhai, M. Li, X. Liu, Y. Zhou, Friction Behaviors and Effects on Current-Carrying Wear Characteristics of Bulk Ti3AlC2, Tribology Transactions. 57 (2014) 300–307. https://doi.org/10.1080/10402004.2013.871377.

[157] R. Holm, Electric Contacts, Fourth Edi, 1981. https://doi.org/10.1007/978-3-662-06688-1.

[158] J.M. Bennett, Recent developments in surface roughness characterization, Meas Sci Technol. 3 (1992) 1119. https://doi.org/https://doi.org/10.1088/0957-0233/3/12/001.

[159] J.A. Greenwood, J.B.P. Williamson, Contact of nominally flat surfaces, Proc R Soc Lond A Math Phys Sci. 295 (1966) 300–319. https://doi.org/10.1098/rspa.1966.0242.

[160] P.G. Slade, Electrical Contacts: Principles and Applications, Second Edi, Taylor & Francis Group, 2014.

[161] J.A. Greenwood, Constriction resistance and the real area of contact, British Journal of Applied Physics. 17 (1966) 1621. https://doi.org/https://doi.org/10.1088/0508-3443/17/12/310.

[162] R.E. Cuthrell, D.W. Tipping, Electric contacts. II. Mechanics of closure for gold contacts, J Appl Phys. 44 (1973) 4360–4365. https://doi.org/10.1063/1.1661964.

[163] C. Torres, R. Quispe, N.Z. Calderón, L. Eggert, M. Hopfeld, C. Rojas, M.K. Camargo, A. Bund, P. Schaaf, R. Grieseler, Development of the phase composition and the properties of Ti2AlC and Ti3AlC2 MAX-phase thin films – A multilayer approach towards high phase purity, Appl Surf Sci. 537 (2021) 147864. https://doi.org/10.1016/j.apsusc.2020.147864.

[164] R. Grieseler, Untersuchung der Eigenschaften sowie der Anwendung von reaktiven Mehrschichtsystemen in der Aufbau-und Verbindungstechnik, 2015. www.tu-ilmenau.de/wt.

[165] B.D. Cullity, Elements of X-ray Diffraction, 1978.

[166] A. Mariscal, A. Quesada, A. Tarazaga Martín-Luengo, M.A. García, A. Bonanni, J.F. Fernández, R. Serna, Europium monoxide nanocrystalline thin films with high near-infrared transparency, Appl Surf Sci. 456 (2018) 980–984. https://doi.org/10.1016/j.apsusc.2018.06.180.

[167] L.Ph. Bérubé, G. L´Espérance, A Quantitative Method of Determining the Degree of Texture of Zinc Electrodeposits, J Electrochem Soc. 136 (1989) 2314. https://doi.org/10.1149/1.2097318.

[168] M.K. Camargo, I. Tudela, U. Schmidt, A.J. Cobley, A. Bund, Ultrasound assisted electrodeposition of Zn and Zn-TiO2 coatings, Electrochim Acta. 198 (2016) 287–295. https://doi.org/10.1016/j.electacta.2016.03.078.

[169] JCPDS-ICCD, Powder Diffraction Files. Bd Sets 1-50,70-88. PDF-3. International Centre for Diffraction Data., Newtown Square. PN (n.d.) 2000.

[170] M. Wilke, G. Teichert, R. Gemma, A. Pundt, R. Kirchheim, H. Romanus, P. Schaaf, Glow discharge optical emission spectroscopy for accurate and well resolved analysis of coatings and thin films, in: Thin Solid Films, 2011: pp. 1660–1667. https://doi.org/10.1016/j.tsf.2011.07.058.

[171] R. Grieseler, B. Hähnlein, M. Stubenrauch, T. Kups, M. Wilke, M. Hopfeld, J. Pezoldt, P. Schaaf, Nanostructured plasma etched, magnetron sputtered nanolaminar Cr2AlC MAX phase thin films, Appl Surf Sci. 292 (2014) 997–1001. https://doi.org/10.1016/j.apsusc.2013.12.099.

[172] V. Presser, M. Naguib, L. Chaput, A. Togo, G. Hug, M.W. Barsoum, First-order Raman scattering of the MAX phases: Ti2AlN, Ti2AlC0.5N0.5, Ti2AlC, (Ti0.5V0.5)2AlC, V2AlC, Ti3AlC2, and Ti3GeC2, Journal of Raman Spectroscopy. 43 (2012) 168–172. https://doi.org/10.1002/jrs.3036.

[173] V. Presser, M. Naguib, L. Chaput, A. Togi, G. Hug, M.W. Barsoum, Erratum: First-order Raman scattering of the MAX phases: Ti 2 AlN, Ti 2 AlC 0.5 N 0.5 , Ti 2 AlC, (Ti 0.5 V 0.5 ) 2 AlC, V 2 AlC, Ti 3 AlC 2 , and Ti 3 GeC 2, Journal of Raman Spectroscopy. 44 (2013) 1060–1060. https://doi.org/10.1002/jrs.4325.

[174] J.E. Spanier, S. Gupta, M. Amer, M.W. Barsoum, Vibrational behavior of the Mn+1AXn phases from first-order Raman scattering (M=Ti,V,Cr, A=Si, X=C,N), Phys Rev B. 71 (2005) 012103. https://doi.org/10.1103/PhysRevB.71.012103.

[175] Z. Feng, P. Ke, A. Wang, Preparation of Ti2AlC MAX Phase Coating by DC Magnetron Sputtering Deposition and Vacuum Heat Treatment, J Mater Sci Technol. 31 (2015) 1193–1197. https://doi.org/10.1016/j.jmst.2015.10.014.

[176] J. Wang, Y. Zhou, Z. Lin, F. Meng, F. Li, Raman active phonon modes and heat capacities of Ti2AlC and Cr2AlC ceramics: first-principles and experimental investigations, Appl Phys Lett. 86 (2005) 101902. https://doi.org/10.1063/1.1873057.

[177] O.D. Leaffer, S. Gupta, M.W. Barsoum, J.E. Spanier, On Raman scattering from selected M2AC compounds, J Mater Res. 22 (2007) 2651–2654. https://doi.org/10.1557/jmr.2007.0376.

[178] G.W. Bentzel, M. Naguib, N.J. Lane, S.C. Vogel, V. Presser, S. Dubois, J. Lu, L. Hultman, M.W. Barsoum, E.N. Caspi, High-Temperature Neutron Diffraction, Raman Spectroscopy, and First-Principles Calculations of Ti3SnC2 and Ti2SnC, Journal of the American Ceramic Society. 99 (2016) 2233–2242. https://doi.org/10.1111/jace.14210.

[179] M. Kadleíková, J. Breza, M. Veselý, Raman spectra of synthetic sapphire, Microelectronics J. 32 (2001) 955–958. https://doi.org/10.1016/S0026-2692(01)00087-8.

[180] P.F. McMillan, N.L. Ross, Heat capacity calculations for Al2O3 corundum and MgSiO3 ilmenite, Phys Chem Miner. 14 (1987) 225–234. https://doi.org/10.1007/BF00307986.

[181] K. Bange, Colouration of tungsten oxide films: A model for optically active coatings, Solar Energy Materials and Solar Cells. 58 (1999) 1–131. https://doi.org/10.1016/S0927-0248(98)00196-2.

[182] A. Coban, E.E. Khawaja, S.M.A. Durrani, Difference between bulk and thin film densities of metal oxide and fluoride films studied by NRA depth profiling techniques, Nucl Instrum Methods Phys Res B. 194 (2002) 171–176. https://doi.org/10.1016/S0168-583X(02)00670-5.

[183] N. V. Tzenov, M.W. Barsoum, Synthesis and Characterization of Ti3AlC2, Journal of the American Ceramic Society. 83 (2000) 825–832. https://doi.org/10.1111/j.1151-2916.2000.tb01281.x.

[184] M.W. Barsoum, M. Ali, T. El-Raghy, Processing and characterization of Ti2AlC, Ti2AlN, and Ti2AlC0.5N0.5, Metall Mater Trans A Phys Metall Mater Sci. 31 (2000) 1857–1865. https://doi.org/10.1007/s11661-006-0243-3.

[185] N.J. Lane, M. Naguib, J. Lu, L. Hultman, M.W. Barsoum, Structure of a new bulk Ti5Al2C3 MAX phase produced by the topotactic transformation of Ti2AlC, J Eur Ceram Soc. 32 (2012) 3485–3491. https://doi.org/10.1016/j.jeurceramsoc.2012.03.035.

[186] M.A. Pietzka, J.C. Schuster, Summary of Constitutional Data on the Aluminum-Carbon-Titanium System, Journal of Phase Equilibria. 15 (1994) 392–400. https://doi.org/https://doi.org/10.1007/BF02647559.

[187] Y.C. Zhou, X.H. Wang, Z.M. Sun, S.Q. Chen, Electronic and structural properties of the layered ternary carbide Ti3AlC2, J Mater Chem. 11 (2001) 2336–2340. https://doi.org/10.1039/b101520f.

[188] X.H. Wang, Y.C. Zhou, Microstructure and properties of Ti3AlC2 prepared by the solid-liquid reaction synthesis and simultaneous in-situ hot pressing process, Acta Mater. 50 (2002) 3143–3151. https://doi.org/10.1016/s1359-6454(02)00117-9.

[189] M.W. Barsoum, M. Radovic, Elastic and Mechanical Properties of the MAX Phases, Annu Rev Mater Res. 41 (2011) 195–227. https://doi.org/10.1146/annurev-matsci-062910-100448.

[190] M.F. Cover, O. Warschkow, M.M.M. Bilek, D.R. McKenzie, A comprehensive survey of M2AX phase elastic properties, Journal of Physics Condensed Matter. 21 (2009). https://doi.org/10.1088/0953-8984/21/30/305403.

[191] T. Liao, J. Wang, Y. Zhou, Chemical bonding and mechanical properties of M2AC (M = Ti, V, Cr, A = Al, Si, P, S) ceramics from first-principles investigations, J Mater Res. 24 (2009) 556–564. https://doi.org/10.1557/jmr.2009.0066.

[192] M.W. Barsoum, M. Radovic, Elastic and Mechanical Properties of the MAX Phases, Annu Rev Mater Res. 41 (2011) 195–227. https://doi.org/10.1146/annurev-matsci-062910-100448.

[193] S.T. Ahams, A. Shaari, R. Ahmed, N.F.A. Pattah, M.C. Idris, B.U. Haq, Ab initio study of the structure, elastic, and electronic properties of Ti3(Al1−nSin)C2 layered ternary compounds, Sci Rep. 11 (2021) 1–8. https://doi.org/10.1038/s41598-021-84466-5.

[194] W.C. Oliver, G.M. Pharr, An improved technique for determining hardness and elastic modulus using load and displacement sensing indentation experiments, Materials Research Society. 7 (1992) 1564–1583.

[195] DIN EN ISO 14577-4:2017-04, Metallic materials - Instrumented indentation test for hardness and materials parameters - Part 4: Test method for metallic and non-metallic coatings (ISO 14577-4:2016); German version EN ISO 14577-4:2016, (2017).

[196] ASTM E2546 - 15, Standard Practice for Instrumented Indentation Testing, ASTM Standards. (2015) 1–24. https://doi.org/10.1520/E2546-15.2.

[197] S.N. Naik, S.M. Walley, The Hall–Petch and inverse Hall–Petch relations and the hardness of nanocrystalline metals, J Mater Sci. 55 (2020) 2661–2681. https://doi.org/10.1007/s10853-019-04160-w.

[198] J.R. Trelewicz, C.A. Schuh, The Hall – Petch breakdown in nanocrystalline metals : A crossover to glass-like deformation, Acta Mater. 55 (2007) 5948–5958. https://doi.org/10.1016/j.actamat.2007.07.020.

[199] G.M. Pharr, E.G. Herbert, Y. Gao, The Indentation Size Effect : A Critical Examination of Experimental Observations and Mechanistic Interpretations, Annu Rev Mater Res. 40 (2010) 271–292. https://doi.org/10.1146/annurev-matsci-070909-104456.

[200] S.M. Han, R. Saha, W.D. Nix, Determining hardness of thin films in elastically mismatched film-on-substrate systems using nanoindentation, Acta Mater. 54 (2006) 1571–1581. https://doi.org/10.1016/j.actamat.2005.11.026.

[201] K. Holmberg, A. Matthews, H. Ronkainen, Coatings tribology - Contact mechanisms and surface design, Tribol Int. 31 (1998) 107–120. https://doi.org/10.1016/S0301-679X(98)00013-9.

[202] G. Plummer, H. Rathod, A. Srivastava, M. Radovic, T. Ouisse, M. Yildizhan, P.O.Å. Persson, K. Lambrinou, M.W. Barsoum, G.J. Tucker, On the origin of kinking in layered crystalline solids, Materials Today. xxx (2021) 1–8. https://doi.org/10.1016/j.mattod.2020.11.014.

[203] M.W. Barsoum, X. Zhao, S. Shanazarov, A. Romanchuk, S. Koumlis, S.J. Pagano, L. Lamberson, G.J. Tucker, Ripplocations: A universal deformation mechanism in layered solids, Phys Rev Mater. 3 (2019) 1–9. https://doi.org/10.1103/PhysRevMaterials.3.013602.

[204] M.W. Barsoum, Ripplocations: A Progress Report, Front Mater. 7 (2020) 1–17. https://doi.org/10.3389/fmats.2020.00146.

[205] G.S. Okram, A. Soni, R. Rawat, Anomalous electrical transport behavior in nanocrystalline nickel, Nanotechnology. 19 (2008). https://doi.org/10.1088/0957-4484/19/18/185711.

[206] H. Zeng, Y. Wu, J. Zhang, C. Kuang, M. Yue, S. Zhou, Grain size-dependent electrical resistivity of bulk nanocrystalline Gd metals, Progress in Natural Science: Materials International. 23 (2013) 18–22. https://doi.org/10.1016/j.pnsc.2013.01.003.

[207] J.M. Camacho, A.I. Oliva, Morphology and electrical resistivity of metallic nanostructures, Microelectronics J. 36 (2005) 555–558. https://doi.org/10.1016/j.mejo.2005.02.068.

[208] M.W. Barsoum, D. Brodkin, T. El-raghy, Layered machinable ceramics for high temperature applications, Scr Mater. 36 (1997) 535–541.

[209] O. Wilhelmsson, J.P. Palmquist, T. Nyberg, U. Jansson, Deposition of Ti2AlC and Ti3AlC2 epitaxial films by magnetron sputtering, Appl Phys Lett. 85 (2004) 1066–1068. https://doi.org/10.1063/1.1780597.

[210] A. V. Pshyk, E. Coy, M. Kempiński, B. Scheibe, S. Jurga, Low-temperature growth of epitaxial Ti2AlC MAX phase thin films by low-rate layer-by-layer PVD, Mater Res Lett. 7 (2019) 244–250. https://doi.org/10.1080/21663831.2019.1594428.

[211] P. Finkel, M.W. Barsoum, J.D. Hettinger, S.E. Lofland, H.I. Yoo, Low-temperature transport properties of nanolaminates Ti3AlC2 and Ti4AlN3, Phys Rev B Condens Matter Mater Phys. 67 (2003) 1–6. https://doi.org/10.1103/PhysRevB.67.235108.

[212] H. Zhai, Z. Huang, M. Ai, Y. Zhou, Z. Zhang, S. Li, Tribophysical properties of polycrystalline bulk Ti3AlC2, Journal of the American Ceramic Society. 88 (2005) 3270–3274. https://doi.org/10.1111/j.1551-2916.2005.00588.x.

[213] Y.A. Wang, J.X. Li, Y. Yan, L.J. Qiao, Effect of surface film on sliding friction and wear of copper-impregnated metallized carbon against a Cu-Cr-Zr alloy, Appl Surf Sci. 258 (2012) 2362–2367. https://doi.org/10.1016/j.apsusc.2011.10.030.

[214] D. Paulmier, M. El Mansori, H. Zaïdi, Study of magnetized or electrical sliding contact of a steel XC48/graphite couple, Wear. 203–204 (1997) 148–154. https://doi.org/10.1016/S0043-1648(96)07361-9.

[215] X. Huang, Y. Feng, J. Ge, L. Li, Z. Li, M. Ding, Arc erosion mechanism of Ag-Ti3SiC2 material, J Alloys Compd. 817 (2020) 152741. https://doi.org/10.1016/j.jallcom.2019.152741.

[216] K. Holmberg, H. Ronkainen, A. Matthews, Tribology of thin coatings, Ceram Int. 26 (2000) 787–795. https://doi.org/10.1016/S0272-8842(00)00015-8.

[217] K. Holmberg, A. Matthews, COATINGS TRI BOLOGY Properties, Tech niq ues and Applications in Surface Engineering, 1994.

[218] D. Dowson, C.M. Taylor, M. Godet, MECHANICS OF COATINGS, 1990.

[219] R. Su, H. Zhang, D.J. O'Connor, L. Shi, X. Meng, H. Zhang, Deposition and characterization of Ti2AlC MAX phase and Ti3AlC thin films by magnetron sputtering, Mater Lett. 179 (2016) 194–197. https://doi.org/10.1016/j.matlet.2016.05.086.

[220] C. Furgeaud, F. Brenet, J. Nicolai, Multi-scale study of Ti3SiC2 thin film growth mechanisms obtained by magnetron sputtering, Materialia (Oxf). 7 (2019). https://doi.org/10.1016/j.mtla.2019.100369.

[221] W. Garkas, C. Leyens, A. Flores Renteria, Synthesis and characterization of Ti2AlC and Ti2AlN MAX phase coatings manufactured in an industrial-size coater, in: Adv Mat Res, 2010: pp. 208–213. https://doi.org/10.4028/www.scientific.net/AMR.89-91.208.

[222] T. Go, Y.J. Sohn, G. Mauer, R. Vaßen, J. Gonzalez-Julian, Cold spray deposition of Cr2AlC MAX phase for coatings and bond-coat layers, J Eur Ceram Soc. (2018). https://doi.org/10.1016/j.jeurceramsoc.2018.11.035.

[223] J.L. Lu, N. Abbas, J.N. Tang, J. Tang, G.M. Zhu, Synthesis and characterization of conductive ceramic MAX-phase coatings for metal bipolar plates in simulated PEMFC environments, Corros Sci. 158 (2019). https://doi.org/10.1016/j.corsci.2019.108106.

[224] I.M. Chirica, A.G. Mirea, Ş. Neaţu, M. Florea, M.W. Barsoum, F. Neaţu, Applications of MAX phases and MXenes as catalysts, J Mater Chem A Mater. 9 (2021) 19589–19612. https://doi.org/10.1039/d1ta04097a.

[225] N.F. Rosli, M.Z.M. Nasir, N. Antonatos, Z. Sofer, A. Dash, J. Gonzalez-Julian, A.C. Fisher, R.D. Webster, M. Pumera, MAX and MAB Phases: Two-Dimensional Layered Carbide and Boride Nanomaterials for Electrochemical Applications, ACS Appl Nano Mater. (2019) 6010–6021. https://doi.org/10.1021/acsanm.9b01526.

# List of publications and conference presentations

## List of publications

### Paper A

**R. Quispe,** C. Torres, L. Eggert, G.A. Ccama, M. Kurniawan, M. Hopfeld, J.L. Zárate, M.K. Camargo, J.A. Acosta, A. Bund, P. Schaaf, R. Grieseler, *"Tribological and Mechanical Performance of $Ti_2AlC$ and $Ti_3AlC_2$ Thin Films"*. Adv. Eng. Mater. (2022) 2200188. https://doi.org/10.1002/adem.202200188.

### Paper B

C. Torres, **R. Quispe**, N.Z. Calderón, L. Eggert, M. Hopfeld, C. Rojas, M.K. Camargo, A. Bund, P. Schaaf, R. Grieseler, *"Development of the phase composition and the properties of $Ti_2AlC$ and $Ti_3AlC_2$ MAX-phase thin films – A multilayer approach towards high phase purity",* Appl. Surf. Sci. 537 (2021) 147864. https://doi.org/10.1016/j.apsusc.2020.147864.

### Paper C

A. Arribasplata-Seguin, **R. Quispe-Dominguez**, W. Tupia-Anticona, J. Acosta-Sullcahuamán, *"Rotational molding parameters of wood-plastic composite materials made of recycled high density polyethylene and wood particles",* Compos. Part B Eng. 217 (2021) 108876. https://doi.org/10.1016/j.compositesb.2021.108876.

### Paper D

**R. Quispe-Dominguez**, S. Naseem, A. Leuteritz, I. Kuehnert, *"Synthesis and characterization of MgAl-DBS LDH/PLA composite by sonication-assisted masterbatch (SAM) melt mixing method"*, RSC Adv. 9 (2019) 658–667. https://doi.org/10.1039/c8ra08780f.

## Conference presentations

1. EUROMAT 2019. European Congress and Exhibition on Advanced Materials and Processes. 1-5 September 2019, Stockholm - Sweden. "Synthesis of MAX phases by co-sputtering and multilayer systems for tribological applications". **R. Quispe**, C. Torres, M. Hopfeld, P. Schaaf and R. Grieseler. Oral presentation.
2. Sinapsis 2021. V Encuentro de Científicos Peruanos en Europa. 21 – 23 October 2021, Turku – Finlandia. "Tribological and mechanical properties of MAX phase thin films for applications as a

protective coating". **R. Quispe**, C. Torres, M. Hopfeld, M. Camargo, P. Schaaf and R. Grieseler. Oral presentation.

3. Latinometalurgia 2021. IX Congreso Internacional LATINOMETALURGIA 2021. "Tribological and mechanical properties of MAX phase thin films for applications as a protective coating on machine components". 15 – 17 December, Cusco – Peru. **R. Quispe**, C. Torres, M. Hopfeld, M. Camargo, P. Schaaf and R. Grieseler. Oral presentation.
4. Workshop – 2019. Multifunctional Materials and Surface Technologies. 25 – 28 March 2019, Lima – Peru. "Study of tribological properties of MAX phases", **R. Quispe**, C. Torres, M. Hopfeld, P. Schaaf and R. Grieseler. Oral presentation.